UNIVERSITY OF CAMBRIDGE
DEPARTMENT OF MATERIALS SCIENCE AND METALLURGY

The Effect of Sintering and CMAS on the Stability of Plasma-Sprayed Zirconia Thermal Barrier Coatings

---

Maya Shinozaki

St John's College
March 2013

A dissertation submitted for the degree of Doctor of Philosophy

This thesis is dedicated to my parents

Preface

This dissertation is submitted for the degree of Doctor of Philosophy at the University of Cambridge, U.K. The research described herein was carried out by myself in the period from October 2009 to March 2013, under the supervision of Professor T.W. Clyne, in the Department of Materials Science and Metallurgy at the University of Cambridge. This dissertation is the result of my own work and includes nothing which is the outcome of work in collaboration except where specifically indicated in the text. No part of this dissertation, or any similar to it, has been, or is currently being submitted for any degree at this, or any other university. It is less than 60,000 words in length.

Maya Shinozaki

March 2013

Abstract

State of the art thermal barrier coatings (TBCs) for gas turbine applications comprise (7 wt.%) yttria partially stabilized zirconia (7YSZ). 7YSZ offers a range of attractive functional properties – low thermal conductivity, high thermal expansion coefficient and high in-plane strain tolerance. However, as turbine entry temperatures are raised, the performance of 7YSZ coatings will be increasingly affected by sintering and environmental contamination, by calcia-magnesia-alumina-silica (CMAS) deposits.

The effect of sintering-induced stiffening on the driving force for spallation of plasma-sprayed (PS) TBCs was investigated. Spallation lifetimes of TBC specimens sprayed onto alumina substrates were measured. A simple fracture mechanics approach was employed in order to deduce a value for the strain energy release rate. The critical strain energy release rate was found to be constant, and if this value had been known beforehand, then the rationale presented here could be used for prediction of coating lifetime.

The effect of vermiculite (VM) and volcanic ash (VA) contamination on the sintering-induced spallation lifetime of PS TBCs was also investigated. The presence of both VM and VA was found to accelerate the rise in their Young's modulus with sintering. Spallation results show that coating lifetime may be significantly reduced, even at relative low addition levels, due to the loss of strain tolerance caused by the penetration of glassy deposits. This result gives a clear insight into the role CMAS plays in destabilizing TBCs.

Finally, the adhesion characteristics of ingested volcanic ash were studied using a small jet engine. The effects of engine speed and particle size were investigated. Deposition on turbine surfaces was assessed using a borescope. Deposition mainly occurred on the nozzle guide vane and blade platform. A numerical model was used to predict particle acceleration and heating in flight. It was observed that larger particles are more likely to adhere because they have greater inertia, and thus are more likely to impact surfaces. The temperature of the larger particles at the end of its flight was predicted to be below its softening point. However, since the component surface temperatures are expected to be hotter, adhesion of such particles is probable, by softening/melting straight after impact.

Acknowledgements

I gratefully acknowledge the provision of funding by the Schools Competition Act Settlement Trust (SCAST), Sulzer Metco Inc., the Royal Aeronautical Society, Cambridge Philosophical and the Worshipful Company of Armourers and Brasiers to support this work.

I would first of all like to thank my supervisor, Prof. Bill Clyne, who has provided me with constant support and guidance throughout my project. His knowledge and commitment has been an inspiration and I would like to thank him for creating such a pleasant working environment.

Many thanks are due to Bennie van de Goor for his excellent technical support and many useful discussions on the Pegasus HP jet engine. Thanks are also due to Dr. Margaret Hartley of the Earth Sciences Department for the provision of the volcanic ash specimen, Prof. Bill O'Neill and Dr. Martin Sparkes, of the Institute for Manufacturing, for their technical assistance with the laser processing of the alumina substrates. Thanks also to Mitch Dorfman and Steve Bomford from Sulzer Metco Inc., for their encouragement and providing the spray powders.

I would also like to say a big thank you to the technical staff at the Department of Materials Science and Metallurgy. Special thanks must go to Kevin Roberts and Les Allen, for their technical (and moral) support, which I could not have done without, as well as for their great company (especially during our frequent trips to Yo Sushi). Thanks are also due to Robert Stearn and Keith Page for their extensive help with technical aspects of the periodic quenching furnace.

I cannot begin to express how grateful I am to the members of the Gordon Laboratory, who made it such a fantastic place to work. A special thank you to Erika, Liza and Sonya for their invaluable friendship, moral support, and for sharing my love for procrastination and conference trips abroad to exotic places. Thanks also to Andy, John, and Ming (for the excellent curry nights), Karen (for being my lovely zumba buddy), Veronica, Su Ki and Noel (for always being so friendly and also for introducing me to Sala Thong restaurant), Chris, James C, Dimitris and James D (for always having the answers) and Alex and Joe (for introducing me to Sporcle).

Last but not least, I would like to thank my loving family, my mother, father and grandmother for their unconditional support. To them, I dedicate this thesis.

Table of Contents

1.0 Introduction

1.1 Overview

State of the art thermal barrier coatings (TBCs) for gas turbine applications comprise yttria partially stabilized zirconia, with a typical composition of ZrO_2 – 7±1 wt.%Y_2O_3 (often referred to as 7YSZ). 7YSZ offers a range of attractive, functional properties – (a) low (for a fully dense material) thermal conductivity ($k \sim 2.3 \pm 0.1$ $Wm^{-1}K^{-1}$), (b) high thermal expansion coefficient ($\alpha \sim 11$ μstrain K^{-1}), (c) high thermochemical stability with the thermally grown oxide (TGO), which is predominantly made of α-Al_2O_3, and, most importantly, (d) high in-plane strain tolerance. The latter originates from its highly porous microstructure, and combined with the material's relatively high fracture toughness, gives the coating superior durability in high temperature and severe thermal cycling conditions.

Since its development, 7YSZ has been rapidly adopted as the preferred TBC material over many other candidates, although arguably its potential is yet to be fully exploited. Despite discoveries of lower thermal conductivity compositions, it still remains the material of choice due to its superior durability. However, it is also evident that the use of 7YSZ is limited for future generation gas turbines, notably in three aspects. Firstly, as turbine entry temperatures are pushed higher, the phase composition of 7YSZ (which in the as-deposited form mainly consists of metastable non-transformable tetragonal phase, t') will increasingly destabilize into Y-rich cubic and Y-lean tetragonal phases, the latter of which is prone to transform into the monoclinic phase upon cooling. The transformation has an associated volumetric expansion of 3 – 5 wt.%, which, should it affect a significant volume of the coating, may be damaging to its mechanical properties. Secondly, as the operating temperatures are raised, 7YSZ coatings will become increasingly affected by the detrimental effects of sintering, such as the increase in through-thickness thermal conductivity and the in-plane stiffness. The former will reduce the coating's thermal insulation capability, whilst the latter will compromise its strain tolerance, which has adverse effects on its durability. Finally, 7YSZ has limited resistance to damage caused by infiltration of molten, environmental deposits (sometimes collectively referred to as calcia-magnesia-alumina-silica compounds, or CMAS), such as sand and volcanic ash. The damage caused is twofold, firstly the infiltration of molten foreign deposits rapidly increases the coating sintering rate, due to a mechanism similar to that of liquid phase sintering. It is shown in the current study that even small additions of CMAS may significantly affect coating durability from accelerated stiffening and in cases of heavy contamination, severe coating embrittlement. Secondly, with extended exposure to high temperatures in the presence of CMAS deposits, accelerated destabilization of 7YSZ takes place, caused by the dissolution of yttria by a silica-rich amorphous phase which rapidly infiltrates and diffuses into the bulk of the coating, tending to segregate at the grain boundaries and free surfaces. The yttria-depleted zirconia phases are thus prone to transform to the monoclinic phase upon cooling, an effect which is similar, but far more aggravated compared to the effects due to sintering alone, and may also embrittle the coating, eventually causing it to fail by extensive microcracking.

The first set of results presented in this thesis concerns the effect of sintering-induced stiffening in promoting spallation of plasma-sprayed YSZ TBCs. Coatings were sprayed onto alumina substrates and were subjected to heat treatments with periodic quenching. By using a simple fracture mechanics approach, the strain energy release rate was obtained, using measured coating stiffness values. The rationale presented here could be used for the prediction of coating lifetime. Experimental results are also presented on the effect of CMAS-type contaminants on the spallation resistance. It is shown that even small amounts of deposits may significantly reduce the coating lifetime. Finally, data is also presented on the deposition behaviour of volcanic ash particulates on internal turbine surfaces of a small jet engine. Observations of deposition were compared with a simple numerical model for particle acceleration and heating, and this was studied for different particle size distributions and engine speeds. This work elucidates the significance of particle velocity and temperature on the deposition efficiency, under real life service conditions.

The first five chapters consists of a literature review on plasma-spraying, residual stresses, strain energy release rate, spallation, degradation caused by CMAS deposits, alternative TBC compositions (including structures that mitigate CMAS attack) and deposition characteristics of ingested particulates carried in high speed flow inside a gas turbine engine.

1.2 Thermal Barrier Coatings (TBCs) for Gas Turbine Applications

Thermal barrier coatings (TBCs) are widely used in gas turbines for propulsion and power generation systems [1-8]. They comprise thermally insulating ceramic material, such as yttria-stabilized zirconia (YSZ), deposited onto the surface of hot engine parts. These parts include the combustor, stationary guide vanes, rotating blades and shrouds in the high pressure section behind the combustor and afterburners in the tail section of jet engines [9]. Typically it creates a temperature drop of ~ 150°C [8] across a coating thickness of 250 – 300 μm, between the hot gas flow at the surface and the load bearing superalloy. Increases in the turbine entry temperature allow overall higher thermal efficiency in power plants and aviation engines. Figure 1-1 shows technological developments over the last 50 years, which have facilitated higher operating temperatures. This is due to three principal materials developments; (a) advances in superalloy design with compositions that are highly resistant to creep, fatigue, oxidation and hot corrosion, (b) better casting technology, allowing production of single crystal blades with intricate cooling air passages and (c) the use of TBCs. It is clear that the implementation of TBCs in conjunction with innovative cooling methods have had a much greater impact on the increase in gas temperature than those enabled by the development of superalloys. Thus during the last 30 years many studies have concentrated on the development of a compliant and robust TBC system.

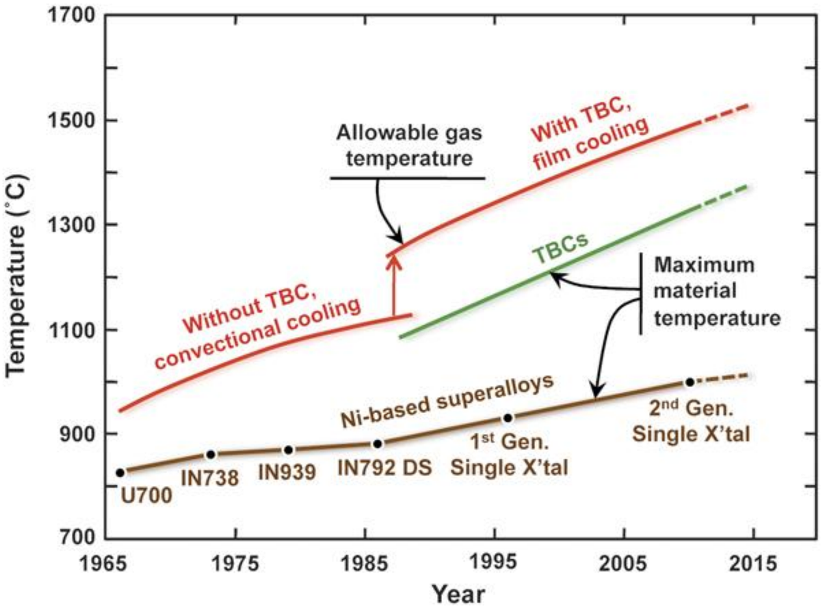

Figure 1-1 Developments in alloy design, multi-passage cooling systems, manufacturing processes and TBCs that have increased the operational turbine entry temperature [9].

Improved performance of TBCs, and hence lower metal temperature, offer the potential to increase component durability (by reducing effects of fatigue, creep rupture and chemical attack), to reduce cooling air and to achieve further efficiency gains. However, such efficiency gains rely on the durability and predictability of TBC performance in increasingly harsh operating conditions. Thus, it is imperative that their basic thermomechanical behaviour in service is well understood.

A typical thermal protection system consists of four layers; the TBC (top coat), the thermally grown oxide (TGO), metallic bond coat (BC) and the superalloy substrate. The TBC provides thermal insulation, whilst the function of the BC and TGO is to improve coating adhesion and to act as a diffusion barrier preventing oxidation of the underlying superalloy. The TGO is a reaction product, the formation of which is facilitated by the fact that the TBC is transparent to oxygen [10, 11]. Each of these layers behaves in a dynamic and interactive way, making it a complex composite system. Table 1-1 summarizes the function, common composition and deposition methods employed for the main constituents. Figure 1-2 shows a schematic illustration of the thermal barrier system on a turbine blade.

Layer	Function	Main Properties	Material	Deposition process
TBC	Thermal insulation, reduces metal temperature	High strain tolerance, low thermal conductivity	YSZ	APS/ EB-PVD
TGO	Reaction product of Al-rich BC, acts as oxidation barrier to substrate	Dense, adherent oxide layer, phase compatible with TBC at high temperature.	Mostly α-Al_2O_3	-
Bond Coat	Improves adhesion of TBC, oxidation protection of substrate	Oxidation resistant	MCrAlY*/ PtNiAl	VPS/ LPPS/ EB-PVD
Superalloy	Takes structural loading	Creep, fatigue, oxidation and hot corrosion resistant	Ni-base superalloy	-

*Table 1-1 Summary of functions, properties, common material and deposition methods of TBC system constituents.*M refers to a metallic element, typically one or two of Co, Ni or Fe.*

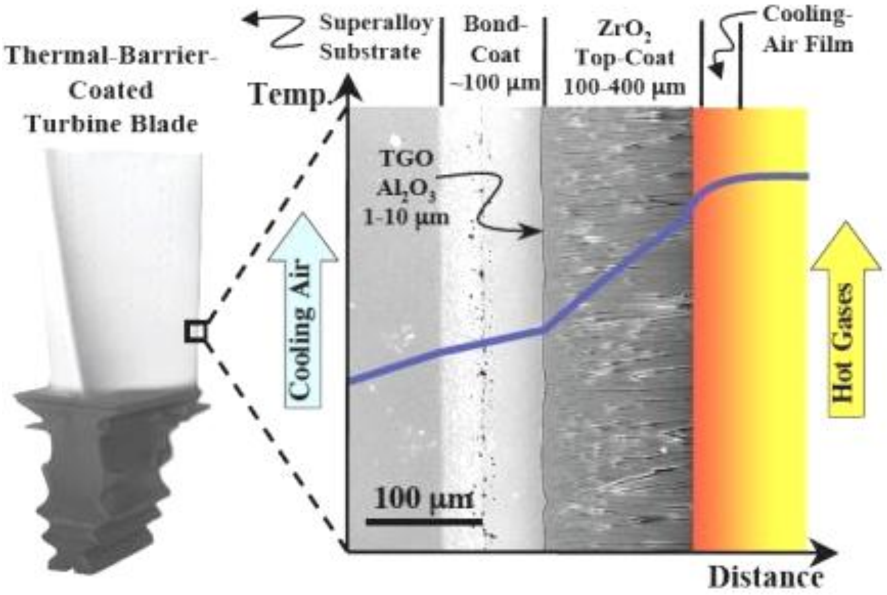

Figure 1-2 Schematic illustration of EB-PVD TBC, TGO, bond coat on a turbine blade [5].

1.2.1 Top Coat

The TBC should ideally be strain-tolerant. It is designed to avoid delamination or “spallation” due to thermal expansion mismatch between itself and the substrate. Today, zirconia ZrO_2 is by far the preferred material, stabilized into its cubic/tetragonal phases by the addition of yttria in solid solution. This material is often referred to as yttria-(partially) stabilized zirconia (YSZ or Y-PSZ). Many studies have been conducted to identify alternative stabilizers (e.g. MgO, CeO_2, Sc_2O_3, In_2O_3, Yb_2O_3 and CaO) and to develop co-stabilized (i.e. with Y_2O_3) coatings [3, 5, 12-15], but 7 – 8 wt.% YSZ has consistently been found to be most suitable for TBC applications. YSZ has several characteristics that make it difficult to displace. YSZ offers intrinsically low thermal conductivity (achieved by the addition of yttria, by introduction of more oxygen vacancies), has relatively high fracture toughness, is thermodynamically stable in contact with alumina and has a thermal expansion coefficient close to that of the metal substrate (see Figure 1-3). The latter helps to minimize the differential thermal contraction stresses during service [10, 16-18]. It is also imperative for it to have a low through-thickness thermal conductivity (~ 1 W m^{-1} K^{-1} for plasma-sprayed YSZ and ~ 1.8 W m^{-1} K^{-1} when deposited by EB-PVD [19, 20]) which is stable in the temperature range in which the gas turbine operates [10]. YSZ may also be easily deposited, either by plasma-spraying or by electron beam deposition techniques without any significant loss of components (as the vapour pressures of ZrO and YO are comparable [3]). On rotating components, particularly for aviation engines, the thickness of the TBC layer is important. It must be sufficiently thick to produce the desired temperature drop, whilst thin enough to avert excessive inertial loads. For aerospace applications, top coat thicknesses range from 100 – 250 µm, whilst for stationary components, such as in shrouds and combustors, the choice is typically 500 µm – 1 mm [21].

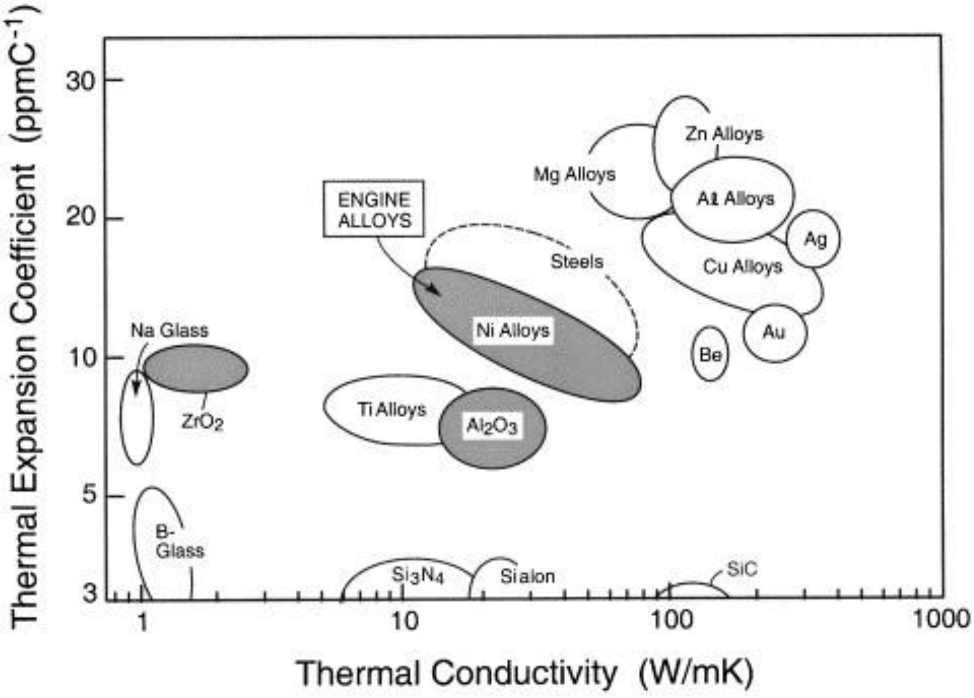

Figure 1-3 Thermal expansion coefficient against bulk thermal conductivity for TBC system constituents [10].

The YSZ, when it is in the form of the t' metastable phase (achieved via various deposition techniques) is experimentally proven to exhibit superior fracture toughness and erosion resistance, compared to many other engineering ceramics [9]. This is attributed to a mechanism called ferroelastic toughening [21-24]. It is postulated that unlike other transformation toughened ZrO_2 based ceramics, the toughness of 7YSZ does not arise from the martensitic transformation (from the tetragonal to the monoclinic phase) but from ferroelastic domain switching from one tetragonal variant to another when stressed. Ferroelastic toughening mechanism can also operate at high temperatures (such as those encountered by gas turbines in service), unlike phase transformation related toughening.

1.2.2 Bond Coat and TGO

The chemistry, surface roughness and microstructure (and hence its process parameters) of the bond coat all influence the TBC durability, mostly by affecting the morphology and thus the fracture energy of the TGO/BC interface. There are two main categories of bond coats. Firstly, there is the NiCoCrAlY overlay system [25], which is commonly deposited through low pressure plasma-spraying (LPPS), with thickness in the range 150 – 250 μm. It results in several phases, the main constituents being β-NiAl, γ-Ni solid solution or γ'-Ni_3Al. The Y (or other reactive elements such as Hf) is added in low concentrations (< 1 wt.%) to act as a sulphur getter, which diffuses to the BC/TGO interface and forms stable sulphides. Sulphur, even when present in very low concentrations, as low as < 1 ppm, is known to segregate at the oxide/metal interface, which compromises TGO adherence, possibly by decreasing chemical bond strength or introducing voids [26-29]. Much of the sulphur embrittlement is suppressed by the Y addition and uniform dispersion of such reactive elements is achieved via both PS and PVD methods for optimal alumina scale adhesion.

The second category of bond coats consists of Pt-modified diffusion aluminide, which is created by electroplating a thin layer of Pt onto the superalloy and then aluminizing it, resulting in a thickness of around 30 – 50 μm. They consist mainly of β-alumina with Pt solid solution. It is widely accepted that the presence of Pt mitigates the embrittling effect of S and hence improves TBC lifetime. While reactive elements such as Y and Hf segregate along grain boundaries and encourage slow upward Al diffusion to induce uniform production of α-Al_2O_3, Pt does not directly affect TGO growth rate, nor the resulting morphology and microstructure. Instead the presence of the Pt slows down the interdiffusion of transition elements from the superalloy, particularly Ti, Re and W, and reduces the activation energy for upward Al and downward Ni diffusion (hence reducing interfacial void formation) [29, 30]. Activation energy calculations conducted by Marino et al. [31] on the interdiffusion mechanisms of Al and Ni agrees with experimental observations that TBC lifetime is significantly improved by the presence of Pt, by maintaining a high level Al concentration at the interface for sustained formation of the alumina scale.

The thermally grown oxide (TGO) is a reaction product between the BC and the combustion gases, and is initially of order ~ 1 µm thickness. The bond coat is rich in Al in order to preferentially produce a protective α- Al_2O_3 scale. Whilst oxygen can readily ingress the TBC [11], α-Al_2O_3 has a low oxygen diffusivity, which improves TBC adherence. Alumina is also known to be highly resistant to high temperature type I hot corrosion [32] and it also effectively heals, should spallation occur. To achieve the protective requirements, the BC must serve as a chemical reservoir for TGO formation, as well as a diffusion barrier or diffusion sink for any deleterious refractory elements from the superalloy substrate that may degrade the bond-coat properties or the bond coat-TGO interfacial fracture properties [33].

1.3 Coating Deposition Techniques

Two methods are currently used to deposit TBCs, namely plasma-spraying (PS) and electron beam-physical vapour deposition (EB-PVD). EB-PVD involves the evaporation of an ingot by heating with a high energy electron beam. The vapour, containing the coating molecules, is then directed towards a pre-heated target, at a deposition rate of typically 4 – 10 µm min^{-1} [6]. EB-PVD creates a columnar grain structure with multi-scale porosity (Figure 1-4(b)), providing excellent in-plane strain tolerance and surface finish of around 1 – 5 µm R_a.

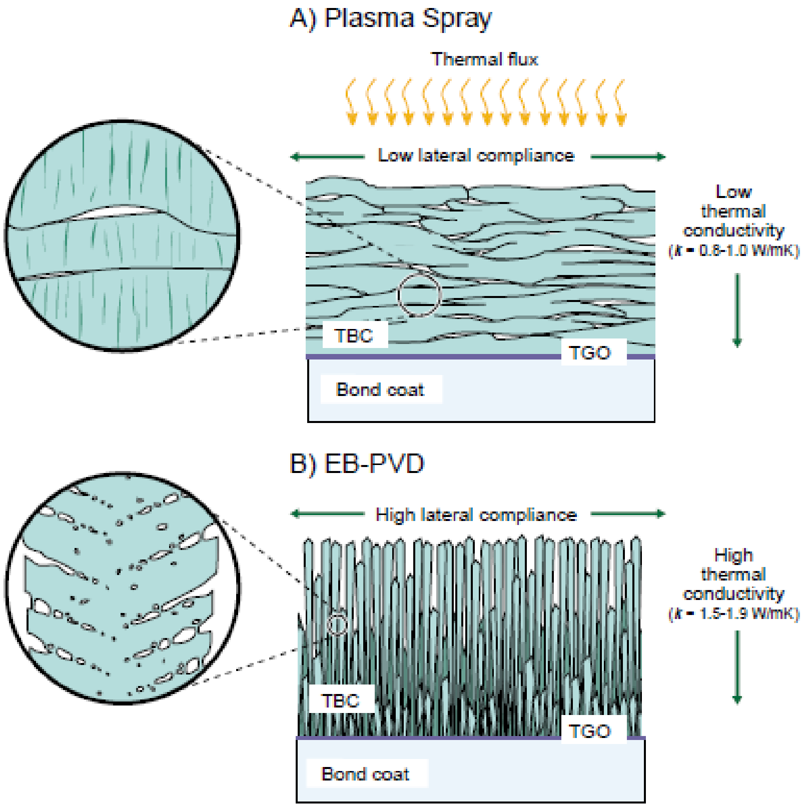

Figure 1-4 Schematic microstructures of (a) plasma spray (PS) and (b) EB- PVD TBCs [34].

The plasma-spraying process is the more cost effective of the two. The process results in a highly anisotropic structure containing a network of inter/intra-splat voids, making it very compliant (Figure 1-4 (a)). In order to control the pore scale and oxide inclusions within the coating, it is also possible to plasma-spray in reduced pressure of inert atmosphere. For both types of coating, after prolonged exposure to high temperatures, sintering reduces fine scale porosities, which results in increased stiffness and thermal conductivity.

1.3.1 Plasma-Sprayed (PS) Coatings

A schematic of a typical plasma spray gun is shown below (Figure 1-5). The basic operation is by creation of a plasma stream, into which the feedstock material is introduced through the powder port. It is then projected towards a substrate in molten form, where it impacts and solidifies, creating overlapping “splats”, thus coating the substrate. The spraying may be conducted in air (APS), low pressure (LPPS) or vacuum (VPS). The resulting microstructure consists of lamellar splats of diameters 100 – 200 μm and thicknesses 2 – 8 μm, formed by rapid solidification, characterised by columnar grains within each splat parallel to the spray direction [35]. Plasma-spraying is a very versatile process, since coatings of many material types may be deposited, including metals, ceramics and composites. Typically, static components, such as combustor cans, vane platforms and also blades in the hot section of stationary gas turbines are coated with PS TBCs.

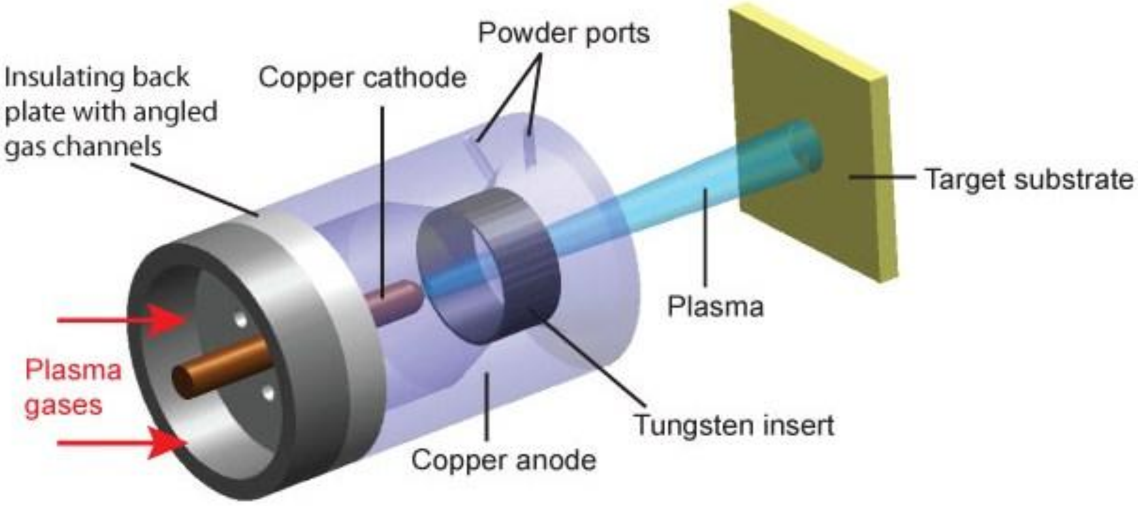

Figure 1-5 Schematic of plasma spray gun

PS coatings consist of a layered structure that is highly anisotropic, with splats orientated parallel to the substrate interface. PS coatings in the as-sprayed state have a low global in-plane stiffness and through-thickness thermal conductivity (typically around 10 – 70 GPa and 1 W m^{-1} K^{-1}) compared to that of bulk YSZ (~ 220 GPa and ~ 2.5 W m^{-1} K^{-1}) owing to its porous and layered microstructure. The low stiffness in the as-sprayed state means it has a high strain tolerance and any residual stresses that develop during service tend to be low. Figure 1-6 shows a typical as-sprayed microstructure. Pores of varying size and shape are seen both between and within individual splats. They are referred to as inter-splat and intra-splat voids respectively.

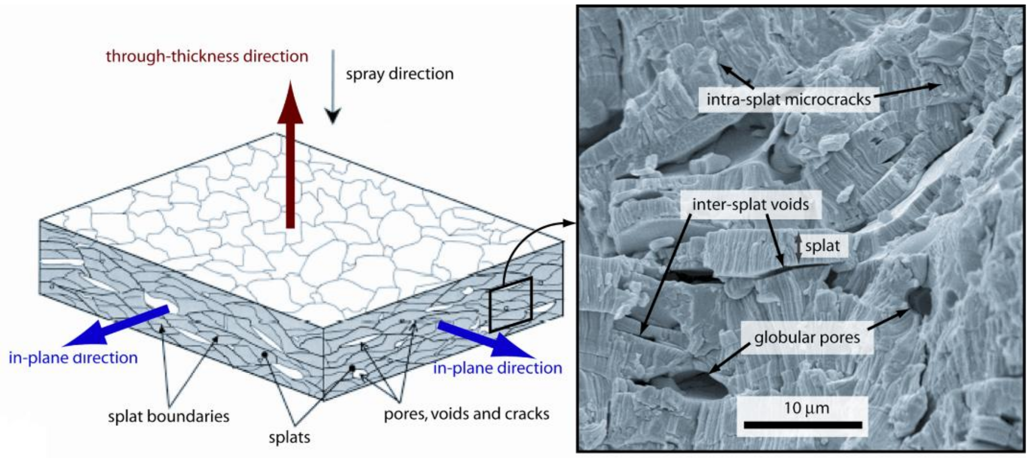

Figure 1-6 Pore architecture in plasma-sprayed coating. Showing spray direction [36] and fractured cross section [37].

Two recent developments in PS technology are notable. The first of these are the dense, vertically cracked (DVC) TBCs, wherein the presence of large through-thickness cracks mimics the segmented and columnar microstructure of EB-PVD coatings. The idea is to improve their strain tolerance. However, its overall denser microstructure (with significantly reduced small scale porosity) means a penalty incurs in the thermal insulation capacity, although its erosion resistance has been reported to improve slightly. Another recent innovation is the solution precursor plasma spray (SPPS). Solvents are fed into the plasma stream, which then undergo evaporation, pyrolysis and crystallisation during its flight. However, such developments are still in their infancy, and careful optimization of spray parameters is often necessary to produce a coating of satisfactory quality. It does offer the advantage of not requiring a powder feedstock and thus expands the scope for exploring complex alternative TBC compositions. Further details on the above techniques may be found in Section 1.3.3.

1.3.2 EB-PVD Coatings

The EB-PVD (electron beam-physical vapour deposition) method emerged in the 1980s. It involves evaporating the coating material within an evacuated chamber. The vapour evaporates according to a $\cos^n$ characteristic in all areas of the chamber. The vapour of the coating material condenses onto a (preheated) substrate surface, forming a coating. If an oxide is being deposited, a controlled amount of oxygen may be fed into the chamber in order to achieve the desired stoichiometry in the coating. In order to ensure good coating adhesion, substrates are heated to ~ $T = 0.5T_\mathrm{m}$ where T_m, is the melting point of the deposited material [20]. In addition, substrate rotation, which causes flux shadowing, is often required in order to create sufficient inter and intra-columnar porosity.

The deposition rate is lower than in plasma-spraying, usually around 4 – 10 µm min^{-1} [6]. Figure 1-7 shows a typical cross sectional microstructure of a 7YSZ EB-PVD TBC, with the underlying TGO. Its microstructure, consisting of poorly bonded columns aligned perpendicular to the substrate surface, confers a high level of in-plane strain tolerance compared to plasma-sprayed coatings. EB-PVD coatings are thus generally observed to have improved spallation lifetime, and therefore are favoured in aerospace applications, particularly in smaller, moving components, which are subject to high temperatures and rapid thermal cycling. Thermal conductivity values, on the other hand, are reported to be significantly higher than their APS counterparts. This is because their large intercolumnar pores are not so effective in impeding heat flow, and they do not have as many pores that are inclined perpendicularly to the heat flux. Typical thermal conductivity values for EB-PVD coatings are 1.5 – 2.0 W m^{-1} K^{-1} [5]. Surface roughness values in the as-deposited state are typically R_a ~ 1 µm, as opposed to R_a ~ 10 – 20 µm for PS coatings. This has obvious aerodynamic advantages and eliminates the need for final polishing stages. In addition, the EB-PVD process deposits with minimal closure of cooling holes (0.25 – 0.5 mm diameter) in aerofoils and therefore requires less subsequent conditioning [1]. The high investment costs and low deposition efficiency of EB-PVD coatings, however, does make it a comparatively expensive process.

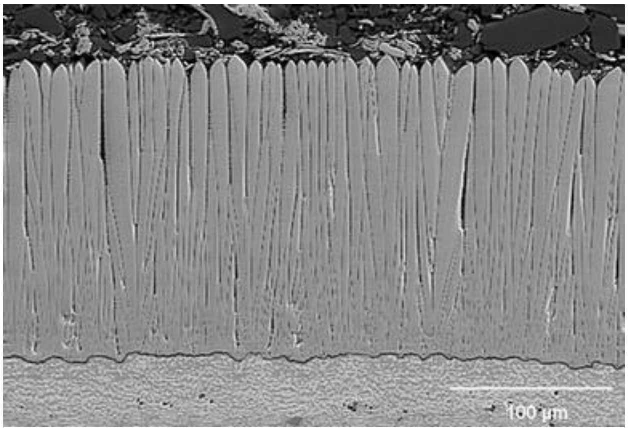

Figure 1-7 Cross sectional image of 7YSZ EB-PVD TBC [38].

Mechanisms responsible for the different types of porosity present in EB-PVD coatings have been elucidated [39]. It has been shown that the shadowing effect plays a critical role in creating the anisotropic textures in the columnar coatings. This is because the microstructure is sensitive to the complex interactions between the local vapour flux and the geometry of the component [14]. Such findings expand the scope for further process optimization in order to achieve desired microstructures.

There have been some innovations to the EB-PVD technology which produces coatings with a modified structure, one such modification is known as directed vapour deposition (DVD) [20, 40]. This method uses a transonic inert gas jet, into which the vapour plume is entrained and deposited onto a substrate, thus significantly improving the deposition efficiency. The interaction between the jet and the substrate results in oblique angle impacts, which causes growth of highly porous, columnar coatings. The motivation behind this technique was to optimize the pore distribution and architectures in order to improve on thermal insulation capabilities, whilst maintaining high in-plane compliance. Hass et al. have also demonstrated that by using DVD and also alternating the incline of the substrates between two fixed angles during deposition, “zig-zag” shaped pores may be created (Figure 1-8). Such structures were reported to have thermal conductivity values as low as 0.8 W m^{-1} K^{-1} [20], which are comparable to PS coatings.

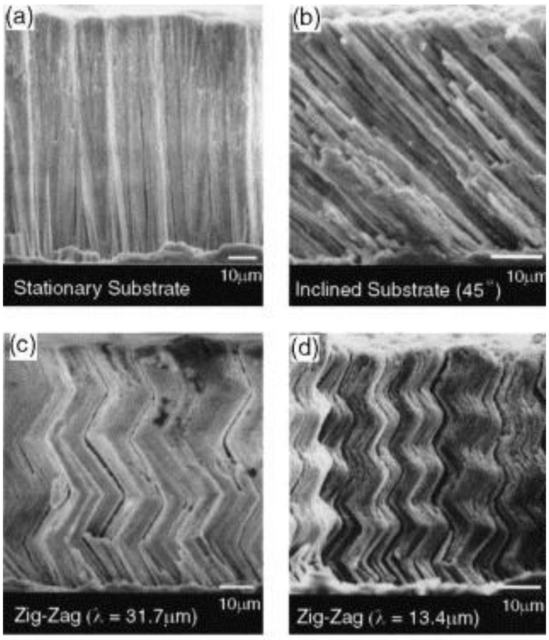

Figure 1-8 Micrographs of EB-DVD coating cross sections. The columns in (a) are aligned perpendicular to the substrate. In (b) the columns are aligned at 45° to the substrate normal. In (c)–(d) coatings with "zig-zag" column morphologies are shown with varying wavelengths [20].

1.3.3 Novel Deposition Techniques

In recent years, a technique called plasma spray-physical vapour deposition (PS-PVD) has been reported to produce strain-tolerant microstructures, with lower thermal conductivity and higher deposition efficiency, which in effect combines the desirable characteristics of both EB-PVD and PS techniques. PS-PVD uses a high energy plasma gun operated at working pressures below 2 mbar [38]. This allows for the possibility to, not only build up a coating from liquid splats, but also by vaporizing the injected material, which is carried by a supersonic plasma plume. The plasma jet forces the evaporated material around complex geometry parts, such as multi-airfoil turbine vanes, allowing for even shadowed areas to be coated, whilst maintaining a columnar microstructure (see Figure 1-9). Coatings produced by PS-PVD, with careful optimization of deposition parameters, have been reported by von Niessen et al. [38] to exceed the spallation resistance of conventional EB-PVD coatings, offer lower conductivity, > 1 W m^{-1} K^{-1} [41] and achieve deposition rates over ~ 10 µm min^{-1}. Their erosion resistance was found to be lower than EB-PVD coatings, but comparable to that of conventional PS TBCs.

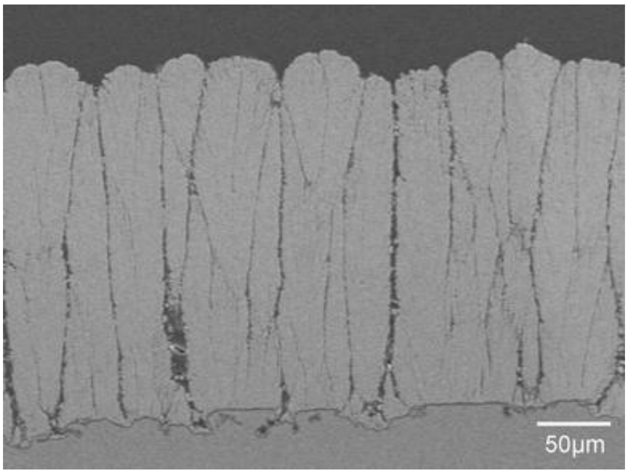

Figure 1-9 Optimized microstructure of PS-PVD coating [38]

Other deposition techniques involve thermally spraying using a liquid carrier. There are two ways in which this is possible, either by injecting (a) precursors in solution (or sol-gel in colloidal solution) or (b) a suspension of submicron particles [42] into the plasma plume. The former technique is often referred to as SPPS (solution precursor plasma spraying) and the latter SPS (suspension plasma spraying). In SPPS, an aqueous chemical precursor feedstock is injected into the plasma jet [43], followed by rapid solvent evaporation, pyrolysis and crystallization, which may occur both in flight and also on the substrate surface [14]. SPPS TBCs contain large vertical cracks in a porous matrix, which consists of submicron scale splats and, in some cases, unmelted particles that have not undergone pyrolysis (Figure 1-10). The large segmentation cracks impart strain tolerance and initial reports of durability tests suggest improved coating lifetimes, albeit only under moderate conditions where the maximum temperature of exposure was ~ 1121°C, compared to PS coatings [44]. Coating regions around the vertical cracks are relaxed, and the beneficial effect of segmentation cracks on coating compliance and thus lifetime has been well documented [45-50]. It may be expected that SPPS will not significantly improve upon EB-PVD coatings in terms of durability. However, SPPS coatings have potentially lower cost [43]. Their thermal conductivity in the as-deposited state, however, is reported to be fairly high for a TBC structure, due to the large proportions of densified regions which have high intersplat areas, measured to be around 1.2 – 1.4 $W\ m^{-1}\ K^{-1}$ [44, 51]. It is also worth noting that, compared to conventional thermal spraying, the use of liquid precursors introduces far more complex physical processes (involving fragmentation and vaporization of liquid in plasma, and subsequent sintering and crystallization [42]), which requires better understanding in order to further optimize the spray parameters.

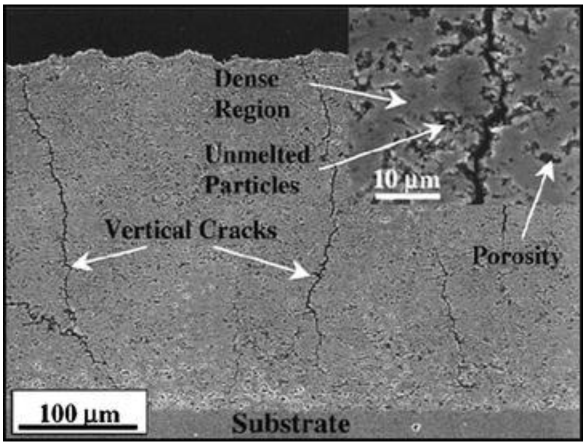

Figure 1-10 Features of SPPS TBCs, including vertical cracks, dense regions of ultra-fine splats, small and uniformly dispersed porosity, and unmelted particles [44]

The SPS process also allows for highly segmented and very porous microstructures to be produced. In SPS, nano-sized powders in suspension are injected into the plasma, whereby the solvent evaporates in flight, allowing for submicron sized molten splats to progressively form on the substrate surface. Since the splats are much finer in scale, SPS coatings contain a higher fraction of submicron pores, which are mostly intersplat porosity, compared to standard PS coatings. SPS coatings contain a lower fraction of intrasplat microcracks, as splats are thinner, and it is postulated that the energy release rate during cooling of each splat is insufficient for crack propagation [52] within the splats. This means that overall tensile stress across the coating thickness, which is essential for the formation of segmentation cracks, may be easily built up during spraying. Due to their highly porous microstructure, their thermal conductivity values have been reported to be as low as 0.5 – 1 W m^{-1} K^{-1} [53]. In addition, the large fraction of fine scale porosity and the presence of overspray (regions of the coating containing unmelted particles) mean that it has a higher specific surface area compared to their conventional counterparts. Despite the obvious gain in compliance due to high porosity and high density of segmentation cracks, improvement in its cyclic lifetime is not so obvious. Guignard et al. [53] conducted cycle tests at 1400°C, which show that the lifetime of SPS TBCs is about 50% lower than the standard APS TBCs. This is attributed to the low toughness of overspray areas and cracks may propagate from one such area to another. It is interesting to note that the segmentation cracks are reported not to heal, even when exposed to high (1400°C) temperatures, and thus the crack density remained fairly constant throughout cyclic heat treatment. This is why it is important to control the original spray parameters, in order to achieve an optimum crack density. In addition, experimental results from Guignard et al. show a significant drawback to SPS coatings, which is that their areas of submicron/nano scale porosity (with large specific surface area) are prone to rapid sintering when exposed to isothermal heat treatment at

1400°C, leading to rapid stiffening. This explains why it was observed to perform poorly compared to APS coatings in thermal cycling tests, hence negating the advantages of the presence of the segmentation cracks. This drawback is likely to similarly affect SPPS coatings, although at the moment there is a lack of data on cyclic lifetime tests conducted at high temperatures > 1200°C.

There is, however, a major industrial advantage to using liquid carriers, which is that it does not require a powder feedstock. For all conventional thermal spraying methods, a flowable feedstock powder is necessary, which must become molten in a matter of a few milliseconds, without vaporizing completely, which often limits the particle size range to around 10 – 70 microns. Hence, both SPS and SPPS are versatile methods that allow spraying of new multiple compositions with submicron-sized particles at relatively low cost.

2.0 Residual Stress and Mechanical Properties of Plasma-Sprayed Thermal Barrier Coatings

PS TBCs have a pore structure, conferring good strain tolerance and thermal insulation capacity. The strain tolerance of TBCs, being one of the key parameters affecting their durability, is dependent on their mechanical characteristics, and particularly on their residual stress state and stiffness. Due to their pore distribution and structure, the mechanical behaviour is non-linear and anisotropic. This chapter explores the origins of residual stresses and strain energy release rate of TBCs, as well as factors which affect their stiffness.

2.1 Residual Stress in PS TBCs

It is widely recognised that residual stresses in plasma-sprayed coatings significantly influence the durability of TBCs and many different mechanisms have been discussed [10, 54-58]. Considerable efforts have been made to understand and predict the development and interaction of stresses during production and service. They may shorten service lives and can result in spallation failure. Residual stresses in sprayed coatings arise from three main sources; *quenching* (of the deposits during plasma spraying), *phase transformation* (due to destabilization of zirconia) and *secondary cooling,* which occurs when the coating/substrate system with an expansivity mismatch is thermally cycled in service. Firstly, the three sources of residual stresses are discussed below.

2.1.1 Quenching Stress

Under plasma-spraying conditions, molten powder particles strike the substrate at velocities exceeding 100 m s^{-1} [59, 60]. Quenching stresses arise from the contraction of molten splats as they cool and rapidly solidify to the underlying substrate temperature. It only takes less than around a millisecond for a thin splat to solidify and cool on the underlying material. Thus each splat impact may be treated as a discrete event. Assuming that the splat behaves elastically, with perfect interfacial bonding, the maximum theoretical value of the quenching stress, σ_{q}, is given by the expression:

$$\sigma_{\mathrm{q}} \sim \frac{E_{\mathrm{YSZ}}\alpha_{\mathrm{d}}(T_{\mathrm{d}}-T_{\mathrm{s}})}{1-\nu_{\mathrm{d}}} \sim \frac{E_{\mathrm{YSZ}}\alpha_{\mathrm{d}}\Delta T}{1-\nu_{\mathrm{d}}} \qquad \text{Equation 2-1}$$

Substituting typical values; E_{YSZ} ~ 220 GPa (Young's modulus of fully dense YSZ), α_{d} ~ 11×10^{-6} K^{-1} (CTE of YSZ), ΔT ~ 1000 K (difference in temperature between a partially-molten splat, T_{d}, and substrate, T_{s}), ν_{d} ~ 0.2 (Poisson's ratio of YSZ) gives σ_{q} ~ 3 GPa, which is much greater than the tensile strength of most ceramic materials. As expected, measured values in comparison are significantly lower (typically < ~ 150 MPa for metallic powders and < ~ 50 MPa for ceramic powders [59]) due to stress relaxation from extensive microcracking and interfacial sliding. Therefore, there is a close connection between the build up of quenching stress and the density of intrasplat cracks. One of the first successful measurements of the quenching stress of plasma-sprayed splats was conducted by Kuroda and Clyne [61] using in situ curvature monitoring during spraying, which generally showed positive dependence on substrate temperature, due to better wetting and therefore interfacial bonding of splats. For some splat materials, such as Ni and Al, a decrease in quenching stress was observed with increasing substrate temperature, and this may be attributed to stress relaxation from creep. It has also been shown that such measured values of quenching stress (for a variety of powders) were independent of substrate material [62]. This is because the substrate is massive and much colder than the splats, so the quenching stress is an indication of the degree of stress relaxation occurring within each splat. Overall, however, due to extensive microcracking, the quenching stress often plays a relatively minor role in the residual stress state of ceramic plasma-sprayed coatings. For ceramic coatings, the CTE mismatch with a metallic substrate tends to be rather high, and thus the thermal stresses generated during service (see section 2.1.3) are expected to be much more significant.

2.1.2 Phase Stabilization of Zirconia and Solid State Transformations

Pure zirconia is a polymorph that exists in three crystallographic phases at atmospheric pressure; the low-temperature *monoclinic* (m) phase, intermediate *tetragonal* (t) phase and a high-temperature *cubic* (F) fluorite phase (see phase diagram for yttria-zirconia system in Figure 2-1 [21]). Stabilization of the tetragonal phase is achieved through the addition of oxides, such as yttria (Y_2O_3), calcia (CaO), magnesia (MgO) and ceria (Ce_2O) [63-65]. Suitable stabilizer dopants must have an appropriate cation radius (similar to that of zirconium). Doping stabilizes the higher temperature cubic and tetragonal phases, depending on the dopant concentration. Dopant concentrations of 6 – 13 wt.% stabilize the tetragonal phase (thus referred to as “partial” stabilization), whereas further increases lead to full stabilization of the cubic phase. These lower valence oxides disfavour the m-phase and stabilize the more symmetric structures of cubic and tetragonal by generation of oxygen vacancies [66]. The main objective of the stabilization is to avoid the disruptive volume change accompanying the martensitic, diffusionless transformation of t → m of 3 – 5% [63, 66-69] upon cooling. When such internal volume changes occur, one would expect an associated increase in the residual stress, which may cause microcracking and impair the mechanical properties of the coating. However, it should be noted, that under most operational conditions, yttria stabilization can minimize this phase transformation effect, and thus the impact it has on the overall residual stress state of the TBC is expected to be fairly low. However, after extended exposure to high temperatures, the yttria diffuses out of the stabilized tetragonal phase, making the small volumes concerned prone to phase transformation. This effect is further discussed in section 3.7.

It is known that, the higher the dopant content, the lower the bulk thermal conductivity, due to the creation of additional oxygen vacancies [3, 70, 71]. However, the stabilized cubic phase have been experimentally proven to exhibit much reduced thermal shock [67, 72] and erosion resistance [22, 73, 74], thus typically for TBC applications, 7 – 8 wt.% (~ 4.5 mol.%) yttria doping is used, which still suppresses the t → m transformation taking place within projected operational temperatures (up to ~ 1200°C).

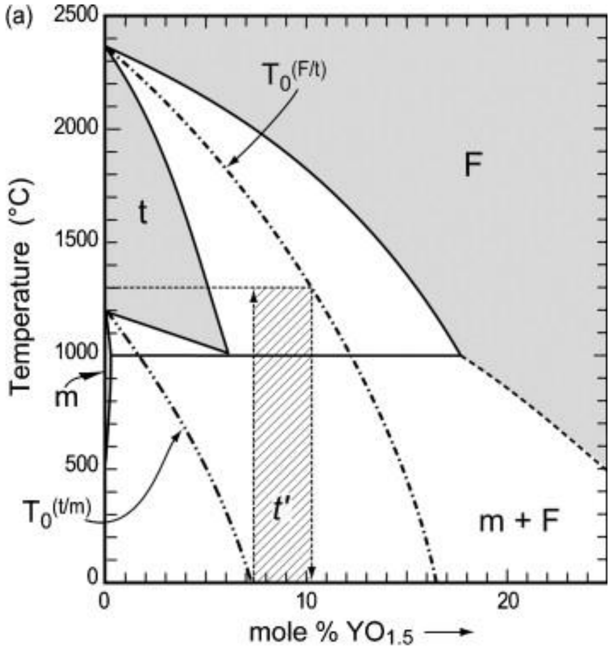

Figure 2-1 (a) ZrO_2–$YO_{1.5}$ phase diagram showing the domain where in non-transformable tetragonal (t') solid solutions are thermodynamically feasible (hatched area) [21]

In addition to the yttria concentration, the deposition process also affects the resulting crystallographic phases for YSZ TBCs. When 7YSZ powder is plasma-sprayed, a metastable tetragonal phase (t') is induced. This is due to a displacive, diffusionless shear transformation from the molten cubic state [75], and is a consequence of very rapid cooling, typically ~ 10^7 – 10^8 K s^{-1}. This phenomenon was first studied comprehensively by Scott et al. [76]. The t' phase is stable till around 1400°C [77] i.e. it will not transform to monoclinic directly upon cooling. Its resistance to transformation is due to its smaller tetragonality and is often referred to as the *"non-transformable"* tetragonal phase.

The yttria concentrations which allow the non-transformable t' phase to form is said to be between 7.5 – 16 wt.% Y_2O_3 [4] (see Figure 2-1). $T_0^{(t/m)}$ and $T_0^{(c/t)}$ marks the temperatures above which it is thermodynamically forbidden (or there is very little driving force) for phase transformations of t → m and c → t to take place respectively. Thus the best-performing t' phase would be achieved by the compositions shown by the hashed area in the binary phase diagram in Figure 2-1.

As mentioned briefly before, this non-transformable tetragonal phase (t') exhibits superior fracture toughness (therefore has superior thermal cyclic durability) compared to its cubic counterpart and this has been attributed to ferroelastic toughening [21-23]. The main reason why this is regarded as the most likely governing toughening mechanism is that it can operate at temperatures exceeding 900°C [78] and its effect is proportional to crystal tetragonality. Mercer et al. [22] have shown that there is evidence of ferroelastic domain formation and switching in dense t' 7YSZ material, in the process regions surrounding a crack. When a crack advances through such materials, irreversible domain switching takes place (where one set of variants within a domain may change orientation) and toughening occurs due to the associated stress/strain hysteresis. However, there is very little evidence to date which confirms the presence of such domains in either EB-PVD or PS coatings of 7YSZ (although some experimental evidence for PS 7YSZ was reported recently by Donohue et al. [24]), so the true reason for its superior toughness and cyclic durability remains to be uncovered.

2.1.3 Differential Thermal Contraction Stress

In general, there is a difference in the coefficients of thermal expansion (CTE) between the substrate and the sprayed material. The plasma-spraying process may heat up the substrate and coating to fairly high temperatures, as high as ~ 600°C in some cases. During subsequent cooling of the specimen (which may be at the end of the coating deposition process or indeed when the component is in service), the mismatch in the expansion properties will generate residual stresses. In practice, very large stresses are readily generated, which may be often sufficient to cause spallation, distortion or the generation of defects such as cracks [79].

The thermal stress, assumed to be equal biaxial, tends to be confined predominantly to the TBC (taken to be transversely isotropic and to exhibit linear elastic behaviour), since the substrate is appreciably thicker and stiffer. In other words, the thermal misfit strain between substrate and coating is accommodated almost entirely within the coating. After cooling from T_2 to T_1, the (in-plane) stress created in the coating is therefore given by [80, 81]:

$$\Delta\sigma = \frac{E_{\mathrm{TBC}}\int_{T_1}^{T_2}\left(\alpha_{\mathrm{sub}}(T)-\alpha_{\mathrm{TBC}}(T)\right)\mathrm{d}T}{1-\nu} = \frac{E_{\mathrm{TBC}}\left(\Delta\alpha\Delta T\right)}{\left(1-\nu\right)} \qquad \text{Equation 2-2}$$

where E_{d} is the global in-plane stiffness of the coating, α_{sub} and α_{TBC} are the thermal expansivities of substrate and TBC and ν is the Poisson ratio of the TBC, taken in the present work to have a value of ~ 0.2. At high temperature, the system is assumed to be in a *stress-free state*. This implies that inelastic effects, such as creep, relax the residual stresses in the system. It must be noted, however, that the assumptions made above may not always be valid, particularly for specimens with thin substrates and/or are small in planar dimensions. In the former case the substrate properties would start to significantly affect the stress state, whilst in the latter case, edge effects may need to be considered.

Such applied thermal loads (inducing in-plane stresses within the TBC) may lead to the initiation of through-thickness (segmentation) and interfacial cracks, as shown by experiments and analytical modelling conducted by Kokini et al. [82, 83]. It can be seen from Equation 2-2 that the driving force for both segmentation and interfacial cracks to propagate will increase either when the stiffness of the TBC, the expansivity mismatch or the temperature drop are increased.

2.2 Measurement of Residual Stress

Several methods for determination of residual stresses in PS TBCs have been established. Each technique has certain advantages and disadvantages. Measurements are often presented together with analytical or numerical prediction techniques.

X-ray diffraction residual stress analysis (XRSA) has traditionally relied on the reflection based $\sin^2\psi$ technique, and is the most widespread technique [55, 58, 84-87]. In this method the lattice d-spacing is determined as a function of ψ, the tilt angle, defined relative to the surface normal of the sample. Lattice strains are obtained from shifts in d-spacing with respect to an unstrained specimen. This technique is limited by the low penetration depth of the X-rays in zirconia, typically no more than ~ 50 μm depending on porosity level. This is particularly problematic for PS TBCs, whose as-sprayed surface roughness may be up to R_{a} ~ 10 μm, and therefore measurements must be made after careful surface polishing. Inevitably, stresses measured in this region are subject to relaxation associated with the free surface, and stresses imposed as a result of polishing may also need to be taken into account. Analogous neutron diffraction methods [16] have also been used to determine residual stress, with the advantage of having a significantly larger penetration depth (up to a few cm), the ability to identify stress levels in individual phase compositions and the applicability to specimens of various sizes and shapes [58]. However it is an expensive and complex method, also limited by its spatial resolution, which is typically ~ 1 mm.

Micro-Raman spectroscopy may also be used to study the structural and stress changes in the coatings by measurement of Raman scattering that depends on electron–phonon interactions, which are very sensitive to local environments (micrometre range). Therefore it is possible to map out a stress distribution, although the measured area is limited to near the surface [88]. Due to its sensitivity it is a suitable technique to identify and study small changes in the stress states of the coatings. The Raman shift also has a strong dependence on the local TBC structure, which may be affected by the irregularity of pore shape/distribution and local crystalline structure. Therefore careful consideration is necessary when calibrating the measurement for the unstrained stress state. The use of Raman spectroscopy has proven fruitful in several studies [88-90] with some convincing results.

The most promising method for evaluating the average (weighted over the entire coating volume) residual stress involves measuring the curvature of the substrate/deposit couple. The curvature method allows determination of stresses in thick layers of graded or inhomogeneous composition, and is non-destructive. However, unlike for example the neutron diffraction technique, the curvature method can be used on only simple specimen geometries [58]. Due to its simplicity, this technique is suited to in-situ measurement of residual stress development during spraying [91]. There is, however, the issue that the measurement of a single value does not lead to a unique solution for the residual stress state, although in some cases analyses may be applied under simplifying assumptions [79]. It is therefore most informative when used in combination with a numerical model, allowing the prediction of stress distributions.

Several researchers have used numerical models to predict stresses generated by the spraying process [77, 90, 92-94]. Good understanding of the mechanisms of stress generation is essential. In addition, accurate information on the thermal history and the (temperature-dependent) thermal and elastic properties of the coating and substrate is required. Tsui and Clyne [84, 93, 95-97] have outlined an elastic analytical model for the prediction of residual stress. The model analyses coating deposition and stress development as a progressive process, with the coating being treated as a multi-layered composite applied in steps, where stress equilibration is achieved between each step. The final modelling step calculates the stresses resulting from the coating-substrate thermal expansivity mismatch. This CTE mismatch stress is added to the previously calculated deposition stress. The comparison between measured and modelled curvature (and temperature) histories provided a comprehensive method for investigating stress generation mechanisms [54, 61]. It was later shown that final stress predictions of this model was in fairly good agreement with a more complex numerical model developed by Gill and Clyne [79, 91], which allowed curvature history to be predicted from thermo-mechanical material properties (including the quenching stress). The Tsui-Clyne model was also recently implemented by Totemeier and Wright [97], showing good agreement with in-depth measurements by x-ray diffraction.

2.3 Stress Relief by Cracking in TBCs

The formation of a crack in a stressed coating results in the redistribution of various stress components and local relaxation of the stress driving the crack [49, 98]. A variety of different cracking phenomena may occur, such as cracking of the coating itself [99, 100], delamination failure driven by tensile or compressive loads [82, 85, 101-103] or the cracking of the substrate. The consequence of crack formation is very much dependent on the material properties and geometry of the coating system. In the case of TBCs, both through-thickness cracks and interfacial cracks are observed to form, which may eventually lead to coating spallation. However, the mechanism of the evolution of through-thickness cracks is still virtually unknown. Whilst small areas of spalls may be tolerated, degradation becomes a concern after an appreciable area fraction of coating has been removed, exposing the bare metal to dangerously hot gases.

2.3.1 Through-Thickness Cracking

An in-plane tensile stress in a brittle coating, which is bonded to a relatively tough substrate, can be relieved by the formation of through-thickness (or sometimes referred to as “segmentation”) cracks [46, 50, 82, 98, 104]. These cracks may be initiated from surface flaws, edge flaws or from flaws at the interface. Once initiated, such cracks may then propagate normal to the interface and/or may channel across the coating in the in-plane directions (see section 3.6 for further details on the initiation of segmentation cracks). Crack propagation leads to the strain energy in the coating (which is governed by the coating thickness) being relaxed at the cost of the energy required to create new fracture surfaces. For an ideally brittle material, the energy required to create new surfaces is its fracture toughness. At the simplest level of approximation, the fracture toughness may be equated to twice the surface energy, 2γ, because two new surfaces are formed by a crack. It is often the case, however, that dissipative processes occur as the crack advances, thus the fracture toughness is > 2γ. Segmentation cracks are driven by in-plane tensile stresses, thus these cracks propagate almost exclusively in mode I (see section 2.4.1 for the definition of mode mixity).

Typically, the fracture toughness of fully dense 7YSZ is reported to be in the range $40 < G_c < 150$ J m^{-2}, all of which were measured by indentation techniques [22, 105-107]. Many repeats are required in order to ascertain an average crack length, and moreover, the crack path is often complex and its mixity is uncertain. Thurn et al. [108] have reported values for mode I through-thickness cracking of PS 7YSZ, using a miniaturized three point bending test. They reported values of ~ 150 J m^{-2}, with a general tendency for it to increase to 300 J m^{-2} with annealing at 1400°C. In general, measured values for the mode I fracture toughness of through-thickness cracking of PS 7YSZ is currently lacking in literature.

If the coating/substrate interface has a relatively low toughness, the formation of segmentation cracks may lead to coating delamination [50, 100, 101, 109]. On the other hand, if the interface is sufficiently tough, this may allow the stress (which drove the crack) to partially relax, without causing the coating to break down [43, 49, 110]. This may result in the creation of an array of through-thickness cracks in the coating, which are individually still attached to the substrate [111].

Segmentation cracks will also effectively increase the coating compliance (as first shown comprehensively by Berry et al. [112]), and hence may significantly improve coating durability. The in-plane residual stresses must go to zero at the crack faces, and thus the strain energy available for driving interfacial cracks are much reduced in the coating regions near the cracks, which may have a positive effect on its lifetime. This has certainly been observed to be case for DVC (dense vertically cracked) TBCs whereby segmentation cracking is deliberately introduced [45, 50, 103, 113-115]. Solution Precursor Plasma-Sprayed (SPPS) TBCs also possess vertical cracks, which contribute to their superior thermal cyclic durability [43]. Although in terms of their functionality, improved strain tolerance of DVCs and SPPS coatings are offset by their higher thermal conductivity associated with higher coating density. It is also important to bear in mind that the crack density must be carefully optimized so as to avoid compromising the mechanical integrity, as too many cracks will cause the coating to be friable. It is also worth mentioning that wide vertical cracks are also likely to make them susceptible to attack by ingression of molten environmental deposits.

2.3.2 Through-Thickness Crack Spacing

The characteristics of a crack network formed are dependent on the stress distribution, which is related to its generation mechanism. One of the first analytical models for multiple surface cracking of coatings postulates that the local stress is partially relaxed in the region of a distance, r, from the crack, and the stress varies as $1/r$ [116, 117]. Although an analytical expression for r is difficult to obtain rigorously, it is thought to be approximately of the order of magnitude of the coating thickness [49]. In most analyses, the stress distribution is fixed arbitrarily, with the constraint that the normal stress is zero at the crack and will gradually increase to the far field value [118, 119].

Stress relaxation (that happens as a consequence of a through-thickness crack forming) may prevent subsequent cracks from developing, unless they are sufficiently far away so that the strain energy may be built up to a critical level. A concept of minimum crack spacing thus arises, which is related to the coating thickness, residual strain, coating modulus and the fracture toughness of the coating. Thouless [120] obtained an expression for the thermodynamic minimum crack spacing by equating the strain energy changes between a cracked and uncracked coating to the energy associated with the array of cracks. The analysis was conducted assuming identical elastic properties of the coating and substrate, under uniaxial elastic mismatch stress, with the presence of a suitable density of initial flaws and that an array of parallel cracks (all assumed to have reached the interface) propagates across the coating simultaneously (rather than cracks propagating sequentially). The strain energy (per unit area of interface between coating and substrate) associated with the array of cracks, U_{c}, was given by the expression:

$$U_{\mathrm{c}} = \frac{G_{\mathrm{c}} h}{s} \qquad \text{Equation 2-3}$$

where G_{c} is the mode I (see section 2.4.1 for definition of mode mixity) coating fracture toughness, h is the coating thickness and s is the crack spacing. The following expression for the minimum crack spacing was determined (which implies that an array of cracks more closely spaced than this limiting value will not propagate):

$$s_{\min} = 8h\left(1-\sqrt{1-\frac{G_{\mathrm{c}}}{2E\varepsilon^{2}h}}\right) \qquad \text{Equation 2-4}$$

where ε is the uniaxial tensile strain component that is orthogonal to the array of cracks and E is the coating Young's modulus in plane stress conditions.

Thouless et al. [121] later presented an analysis on the sequential development of a crack array, where the energy associated with uniform arrays of increasing density was considered. It was recognised that the previously obtained minimum crack spacing (as shown in Equation 2-4) was in fact unobtainable in practice. In order to analyse a sequential development of cracks, it was assumed that the equilibrium crack density is obtained when the change in elastic energy between a coating with crack spacing s and one with a crack spacing $s\text{-}\delta s$ is insufficient to provide the energy required for the additional cracks. This concept yields the following expression for the equilibrium crack spacing:

$$s_{\mathrm{equib}} \approx 5.6h\sqrt{\frac{G_{\mathrm{c}}}{E\varepsilon^{2}h}} \qquad \text{Equation 2-5}$$

An important difference to note between the two expressions is the predicted relationship between the coating thickness and crack spacing (assuming all else equal). Use of Equation 2-4 suggests that crack spacing decreases as coating thickness increases. Conversely, Equation 2-5 predicts the minimum crack spacing to be proportional to the square root of the coating thickness. The latter expression is in fact in agreement with experiments conducted by Thouless et al. [121]. However, experimental evidence in this area is certainly lacking. Papers by Beuth [99] and Hutchinson and Suo [122] have also explored the mechanics of a cracked coating, incorporating the effects of an elastic mismatch between the coating and substrate. However, the concepts of crack density (and minimum spacing) were not examined in detail.

Finally, it is important to note that cracks, unlike other strain energy relieving mechanisms such as the formation of dislocations, are not mobile. Equation 2-5 can only be considered as an approximation since cracks cannot adjust their spacing to maintain uniform arrays. The assumption of simultaneous propagation of all cracks is also unlikely to be accurate. For example, if a perturbation occurred such that some cracks advanced ahead of the array, the lagging cracks may be shielded to such an extent that the energy release rate associated with them drops below the value required for fracture. A less dense array would then result. In some cases, crack distributions are simply dictated by the stochastic nature of the distribution of initial flaws [123], rather than by the energetics described here. However, provided a suitable density of initial flaws is present (and one may assume that such flaws are ample on the surface of both PS and EB-PVD TBCs) then the general trend in crack formation may be described by energetic considerations.

2.4 Driving Force for TBC Delamination

Brittle coatings subject to residual stress have a tendency to delaminate from their substrates. The susceptibility to delamination depends on the magnitude of the residual stress, the coating thickness, the interfacial fracture energy and the flaw distribution at or near the interface [124]. Many studies have focused on the relationship between residual stress distributions and the corresponding strain energy release rate [125] when the coating becomes debonded. A simple expression for the interfacial strain energy release rate for debonding of such a stressed coating (assumed elastic and equal biaxial) may be derived from the elastic stored strain energy in the coating [21, 54, 81, 100, 117, 122, 126, 127]:

$$G_{\mathrm{i}} = \frac{E_{\mathrm{TBC}} h \varepsilon^2}{2(1-\nu)} \qquad \text{Equation 2-6}$$

Where h is the coating thickness, ε is the in-plane strain in the coating and E_{TBC} is the coating in-plane stiffness. This expression is based on the assumption that only the stress parallel to the direction of crack propagation is relaxed by the debonding, since the other in-plane stress is still constrained as the interfacial crack passes the region concerned.

Debonding is energetically favourable when the interfacial strain energy release rate becomes greater than or equal to the critical strain energy release rate, G_{ic} (or the interfacial fracture toughness) [128-133]:

$$G_{\mathrm{i}} \geq G_{\mathrm{ic}} \qquad \text{Equation 2-7}$$

The interfacial strain energy release rate, G_{i}, in Equation 2-6 may be regarded as the driving force for spallation of a coating. Provided that the stress in the coating is known at the point when debonding occurs, and there are plenty of flaws available to initiate interfacial cracking, G_{ic} can be taken as equal to G_{i} at that point. Note that G_{i} is linearly proportional to the coating thickness and stiffness (from Equation 2-6), implying that the thicker and stiffer the coating, the more likely it is to debond. In other words, provided the stresses are the same, the thickness and strain tolerance of the coating controls the driving force for the creation of new fracture surfaces [80]. This concept explains experimental observations of why thicker top coats debond more readily than thin ones [17, 130, 134], and indeed that debonding is less likely when the top coat is less stiff [17, 110, 135-137] (for a given misfit strain). Thus, provided that the residual stress state and the interfacial toughness may be predicted with confidence, by ensuring that the strain energy release rates remain below that of the interfacial fracture energy, spallation may be avoided. This might constitute an attractive rationale for coating lifetime prediction.

It must be noted, however, that this approach does not take into account any barriers to initiation of the interfacial crack. It simply considers the energetics of the advance of a fully developed crack. In addition, it has long been recognized that the in-plane stress responsible for driving an interfacial crack from a specimen edge (or a segmentation crack) must be relaxed in the regions near the lateral free surface, and thus the initial strain energy release rate will be lower [54]. Several studies have focused on stress distributions in the coating regions near the free surface [100, 122, 126, 138] and its effect on initiation and subsequent propagation. Evans et al. [102] and Akisanya et al. [139] have presented finite element modelling (FEM) data on residually stressed films, showing how the strain energy release rate varies with edge crack length. An analytical model has also been reported [126] which predicts the strain energy release rate as a function of the crack length, with a strong dependence on the relative mechanical properties of the coating and substrate.

$$\frac{G(a)}{G_0} = \left(\frac{a}{hB}\right)^2 - \left(\frac{a}{hB}\right) \ln\left(\frac{a^2}{h^2 B^2}\right) \qquad \text{Equation 2-8}$$

where a is the edge crack length, G_0 is the steady state strain energy release rate expected for a long crack, h is the coating thickness and B is an empirical factor estimated to be an empirical function of the Dundurs parameter, α:

$$B = 10^{(\alpha+1)} \qquad \text{Equation 2-9}$$

and the Dundurs parameter is given by:

$$\alpha = \frac{E_c - E_s}{E_c + E_s} \qquad \text{Equation 2-10}$$

where E_c and E_s is the Young's modulus for the coating and substrate respectively.

From this, it is clear that the stress-relaxed depth in the coating increases as α is raised, reflecting the increased compliance of the substrate, and hence the reduced constraint imposed on the coating. This expression highlights the fact that initiation for spallation may be substantially reduced by edge effects.

It may also be inaccurate to assume that all the elastic strain energy is released upon delamination by bending/extension/contraction of the debonded coating, although experimental evidence suggests that stresses after debonding are rather small [140]. Another question to ask is whether stresses arising from processing, such as quenching stress etc., contribute to the strain energy release rate. Such stresses are in fact, likely to be relaxed at high temperatures so that they quickly become irrelevant. The stresses arising from differential thermal contraction upon cooling thus dominates.

2.4.1 Measurement of TBC Interfacial Strain Energy Release Rate

Although the energy-based argument introduced in the previous section is a simple and promising criterion for estimating the value of the interfacial fracture toughness (G_{ic}) and thus assessing the likelihood of delamination, there are further complications, which must be discussed. One such issue is the effect of mode mixity.

Analysis of the stress field at a crack tip, in characterising interfacial debonding of a thermally sprayed material, is a complex matter. Most situations do not represent conditions of pure mode I crack opening. Structural components in gas turbines are often subject to a mixture of mode II shear loading and mode I opening. Therefore crack growth is often mixed mode, depending on the loading geometry and elastic properties of the coating and the substrate. Mode mixity is usually expressed in terms of the phase angle, ψ (or sometimes referred to as mixity angle):

$$\psi = \tan^{-1}\left(\frac{K_{\mathrm{I}}}{K_{\mathrm{II}}}\right) \qquad \text{Equation 2-11}$$

where K_{I} and K_{II} represent crack tip stress intensity factors for mode I and II. Phase angles of 0° and 90° represent pure opening and pure shear modes respectively.

Studies have shown that the critical strain energy release rate (interfacial fracture energy) usually increases with phase angle and interfacial roughness [54, 125, 141]. This may be due to changes in the source of fracture energy. In pure mode I, the fracture energy is due to breaking of chemical bonding whilst crack shielding and plasticity dissipation at asperities (especially if concerning a metallic interface) becomes significant as ψ increases. The mixity would therefore depend on the associated debonding mechanism.

Various test methods have been devised for determining the fracture toughness of TBC interfaces by inducing debonding with applied stress [80, 108, 109, 142-148]. Four point bending methods, single-edge notched specimens, double cantilever beam tests and indentation techniques are just a few of the range of measurement techniques employed in order to assess the adhesion of thermally sprayed coating systems. For all of these methods, the experimental proposition is to establish the equilibrium condition where the elastic energy provided by an external force is balanced by the propagation of a stable crack. The widespread simple tensile adhesion test (or a “pull-off” test) is not a suitable test for determining the fracture toughness of TBCs - it is at best a semi-quantitative method useful for only comparative purposes. The main issue with this test is that the failure depends on the distribution of flaws present at the specimen edge and also any slight misalignment in the loading system, which results in a wide scatter of values obtained [148].

Values of G_{ic} obtained for as-sprayed TBCs in the literature are in general agreement around 50 – 100 J m^{-2} (with a general tendency for it to decrease with heat treatment [108]), although uncertainty remains over its dependence on ψ. The interfacial fracture toughness value should always be quoted with its associated phase angle, although often the mixity is difficult to ascertain accurately. However, it may be estimated for some simple cases. For example, a coating/substrate system whereby the residual stress states are relaxed by the substrate and deposit bending away from each other, gives rise to mode I loading at the crack tip. Whilst those relaxed by the two constituents changing length (for example due to differential thermal expansion mismatch), generates predominantly mode II loading. A contact shielding model, first suggested by Evans and Hutchinson [149] was recently applied by Arai et al. [150] and is in fairly good agreement with experimental data, although existing test methods are still limited in the measurable range of phase angles, limited by the fracture strength of TBCs. It would be useful to evaluate the interfacial fracture toughness under mixed mode, which is closer to service conditions. This is an area requiring further experimental study.

Lastly, it is important to note that the focus of much work on spallation in the literature has been on interfacial embrittlement, as a result of the growth of the thermally grown oxide (TGO) [10, 132, 133, 151]. Several researchers have also solely focused on the strain energy built up in the TGO [133, 152], and hence regarding that as the driving force for delamination, rather than in the top coat. Such an approach cannot account for experimental observations that thicker top coats debond more readily than thinner ones [17, 130, 134], or indeed that debonding is more likely when the top coat is stiffer [17, 110, 135, 136]. Furthermore, since the TGO is very thin (< ~ 10 µm), prediction that it can store strain energies sufficient to drive interfacial cracking requires the assumption that unrealistically high stress levels (in the GPa range) can be sustained within them. Of course, as the TGO grows, this may degrade the fracture energy of the interface over time, and, in addition, the interface also progressively roughens, and calculations show that out-of-plane (perpendicular to the interface) tensile stresses build up at the asperity tips of the oxide layer. Reports of measurement or the prediction of the change in the interfacial fracture toughness due to the growth of the TGO are sparse [21, 132], and this too is an area which requires further experimental study.

2.4.2 TBC Spallation Lifing Test Methods

Burner rig tests [52, 114, 153, 154], furnace cycle tests and laser shock tests [72, 83, 155, 156] are some of the most common methods of assessing the lifetime of TBCs. These methods are very effective in simulating severe thermal gradients and thermal cycling conditions that TBCs may encounter in service, and therefore are useful for comparative purposes. It is often however, difficult to identify specific failure mechanisms. Ultimately, as discussed in previous sections, the coating lifetime is defined by the fracture energy of the coating in the planes parallel to the interface.

2.5 Macroscopic Stiffness of PS TBCs

Accurate determination of the macroscopic stiffness of the TBC is crucial, in order to predict the residual stress levels and thus the value of the strain energy release rate, which in turn affects their spallation lifetime and thermal fatigue behaviour under cyclic loading. The stress-strain behaviour of TBCs is non-linear and strain-dependent. This is due to the shape, orientation and distribution of pores and cracks within the TBC structure [108, 113, 114, 157-161]. Although the intersplat and intrasplat microcracks may only represent a small proportion of the overall porosity, the elastic openings and partial closings of such cracks under small stresses contribute to its elastic anisotropy. The intersplat microcracks may enable a relative motion and bending of the splats, whereas the intrasplat microcracks reduce the stiffness of the splats themselves [114]. The irreversible behaviour can be explained due to microcrack propagation, mechanical interlocking, loosening or splat sliding [162]. However at very low strains, TBCs tend to exhibit near-elastic behaviour [161]. The anisotropy and hysteretic behaviour is often highlighted at higher strains. The hysteresis is less marked for specimens that have been heat treated [110, 114, 163, 164], mainly due to the removal of small scale porosity caused by sintering, which makes splat sliding more difficult. These are significant complicating factors, since different methods of measuring the stiffness generate different strains and strain distributions, which partly explain the wide scatter in global stiffness values for as-sprayed TBCs reported in literature.

For example, in bend tests [109, 114, 161, 163], approximately half of the specimen volume is under compression and the other half under tension. This means an average value of the stiffness may be measured, weighted equally between its response in tension and compression. Wakui et al. [165] found that the stiffness of an as-deposited PS TBC, measured by four point bend test, decreased from 38 GPa to 12 GPa as the applied strain was increased from -0.75% to 0.11%. Others have also found that the greater the density of microcracks, the greater the difference between the Young’s modulus measured in tension and in compression [148] (although this difference only becomes apparent at relatively high strains, > ~ 0.7%, representing the point when microcracks close up in compression). Ultrasonic methods [135, 166] have also been successfully employed to determine TBC stiffness. This method uses the relationship between ultrasonic wave propagation velocities in a material and its elastic constants. Both beam bending and ultrasonic methods may be regarded as macroscopic stiffness measurements ($\bar{E}_{\mathrm{tbc}}$ in Figure 2-2), which are most widely used. Typical values obtained using ultrasonic or flexural methods range from 10 – 30 GPa.

When indentation techniques [167, 168] are employed, the elastic response of the material is measured predominantly in compression. The indentation measurements represent local Young's modulus values (denoted by E_0 in Figure 2-2), which approach the values of the bulk material, since the region undergoing deformation should be free from larger flaws. This is why indentation techniques often measure higher values (~ 70 – 100 GPa) compared to flexural/bending tests. In general, strong load dependence is also observed. The value of the Young's modulus decreases with increasing indentation load. This is a result of the increasing deformation volume progressively including more pores or cracks responsible for the low values obtained with the flexural techniques. Indentation data are also sensitive to surface roughness.

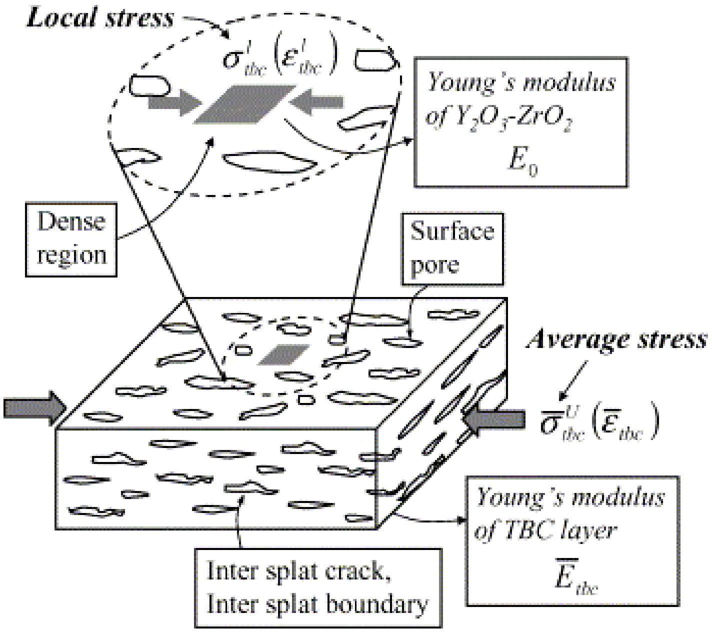

Figure 2-2 Showing the difference between local and average Young's modulus values for PS TBCs [88].

3.0 Sintering-Induced Degradation of PS TBCs

3.1 Sintering of PS TBCs

It is well known that when TBCs are exposed to temperatures above around 1100°C for extended periods of time, sintering takes place [39, 169]. Sintering is a thermally activated process driven by the reduction in surface energy, and it causes morphological changes in the porosity, reduces small scale porosity and increases intersplat contact areas [170]. Although the overall porosity is changed only slightly by these processes [13], at temperatures above 1100°C, drastic changes are observed in the pore size, shape and distribution. Since both the reduction in coating stiffness and thermal conductivity in TBCs are primarily reliant on microstructural optimization, excellent sintering resistance is crucial in order to ensure long term durability and functionality.

3.2 Sintering-Induced Changes in TBC Stiffness

As a consequence of sintering, increased global in-plane stiffness has been widely reported [13, 114, 163, 168, 171-176]. This is caused by microcrack healing, intersplat locking (increase in intersplat contact areas) and also by the stiffening of individual splats. The change in microstructure due to sintering is shown by the micrographs in Figure 3-1.The rate of increase in stiffness is very sensitive to temperature. The experimentally observed rise in stiffness may be divided into two regimes - the initial rapid increase within the first 5 h, followed by a progressive rise. Figure 3-2 shows measured change in stiffness for TBCs with different impurity levels, heat treated at 1400°C. The two regimes are only distinguishable at temperatures typically over ~ 1200°C [163].

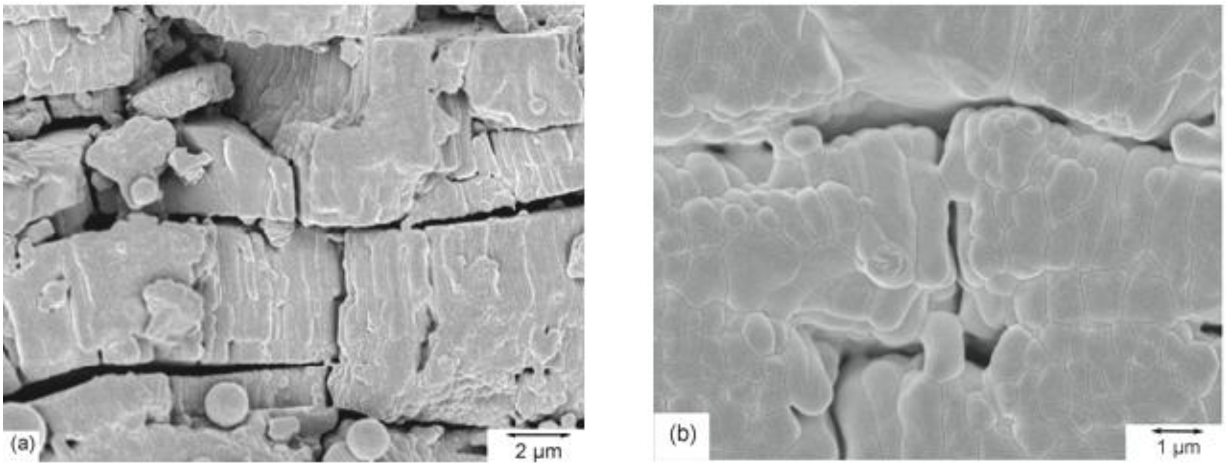

Figure 3-1 SEM fracture surfaces, taken from Paul et al. [177] showing splat structures in PS YSZ coatings (a) as-sprayed and (b) after 10 h at 1400°C.

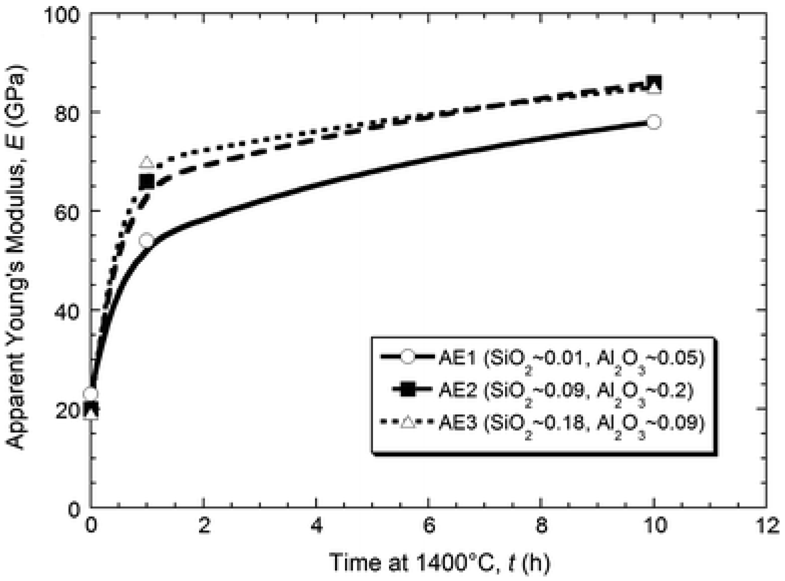

Figure 3-2 Measured in-plane stiffness (by four point bending) of free-standing YSZ coatings, with different impurity levels, as a function of annealing time at 1400°C [177].

Stiffening of the top coat from sintering has deleterious effects on coating spallation resistance by increasing the in-plane stress and strain energy release rates (as previously discussed in Chapter 2.0) induced by differential thermal contraction on cooling. Although the mechanism of sintering-induced stiffening has been made fairly clear, modelling and hence predicting the stiffening behaviour has so far not been possible. There is no simple correlation between volumetric shrinkage and stiffness increase during sintering. This is shown experimentally by Ahrens et al. [114] whose dilatometry data show that the shrinkage due to sintering is substantially larger for coatings with higher overall porosity than for the segmented coatings, whereas it is difficult to distinguish any significant difference in their stiffening behaviour. Stiffness evolution is therefore very much dependent on the pore architecture and orientation rather than the overall porosity. Healing of microcracks and the increase in intersplat contact areas are predominantly caused by surface diffusion, which do not contribute to any densification. It should be noted that, while both grain boundary and surface diffusion will tend to affect changes in pore architecture and associated reductions in surface area, only grain boundary diffusion causes densification, and hence changes in the macroscopic dimensions of the specimen [178, 179].

Cipitria et al. [178, 179] presented a sintering model for prediction of changes in the microstructure and dimensions of both free-standing and constrained PS TBCs, which is based on the variational principle. It incorporates the main microstructural features of PS TBCs and simulates the effects of surface diffusion, grain boundary diffusion, grain growth and the resulting increase in intersplat area. The model is validated by comparison with experimental data for shrinkage, surface area reduction and porosity reduction. Predictions indicate that, while surface diffusion does not directly contribute to coating densification, it can indirectly affect shrinkage rates. If the surface diffusivity is increased, this might consume the driving force for diffusion, therefore retards the rate of grain boundary diffusion. In addition, model predictions indicate that more rapid surface diffusion can accelerate the rate of increase of the intersplat contact area, while simultaneously retarding the rate of densification and shrinkage. This highlights the importance of monitoring both densifying and non-densifying mechanisms (and accurately measuring their respective diffusivities) in order to better understand the effect of sintering on the microstructure and its mechanical properties.

It is worth mentioning that imposed tensile stresses in the coating will retard sintering and the associated stiffening by forcing microcracks to remain open [163]. Tsipas et al. have incorporated the effect of a high thermal gradient along the through-thickness direction and its effect on the residual stress state of TBCs [180], using a model previously developed by Clyne and co-workers [181]. It was shown that, by imposing a thermal gradient, the stress level in the coating tends towards more compressive values, particularly at the free surface, where it is hotter. Thus the free surface is likely to experience accelerated rates of sintering and stiffening.

3.3 Sintering-Induced Changes in TBC Thermal Conductivity

In addition to increased stiffness, increased through-thickness thermal conductivity is observed due to sintering, related to the growth of intersplat contact area, which therefore compromises the thermal insulation capacity of the TBC [2, 20, 39, 168, 182]. Heat transfer within the TBC takes place mainly via conduction, although the contribution from radiation can become significant at temperatures above about 1500 K [178, 183]. Several techniques for measuring conductivity of TBCs are well established. These are laser flash [184, 185], Hot-Disk® [186] and the steady state bi-substrate [187] techniques. In the former two techniques, only the thermal diffusivity is measured and the specific heat must be independently obtained in order to evaluate the thermal conductivity. Considerable care is required in determining a reliable value for the thermal diffusivity using the laser flash method, since factors such as laser power, detector linearity, opacity and thermal history of the specimen must be taken into account [188, 189]. In addition, the precise conductivity of air (at operational temperatures) in the intersplat pores is predicted to have a significant effect on the overall conductivity (as TBCs are known to have high gas permeability [11]), which depends on the gas pressure [190]. TBCs on components within the gas turbine engine, where the gas pressure is typically about 40 atm [37, 182, 183], may thus exhibit appreciably higher conductivities in service than those obtained experimentally, which are almost invariably measured at ambient pressure and temperature.

Finite element modelling has been employed to study the effects of shape, orientation and volumetric percentage of porosity on the thermal conductivity of TBCs [191]. It was found that cracks orientated parallel to the coating surface (i.e. inter-splat gaps) contribute far more in reducing the thermal conductivity, since they lie perpendicular to the direction of the heat flux. Cylindrical pores and vertical cracks on the other hand, are expected to contribute less to impeding the heat flow. Analytical and numerical models for simulation of heat flow in TBCs for prediction of thermal conductivity from microstructural parameters, have been suggested by Tsipas and Golosnoy et al. [178, 183]. The model includes heat flow via phonon conduction through the solid, molecular collision conduction through gas in pores and radiative transmission through both components. The effective thermal conductivity was predicted to be most sensitive to bridge contact area (and not to overall porosity). Figure 3-3 shows schematic representation of the two flux regimes used in this model.

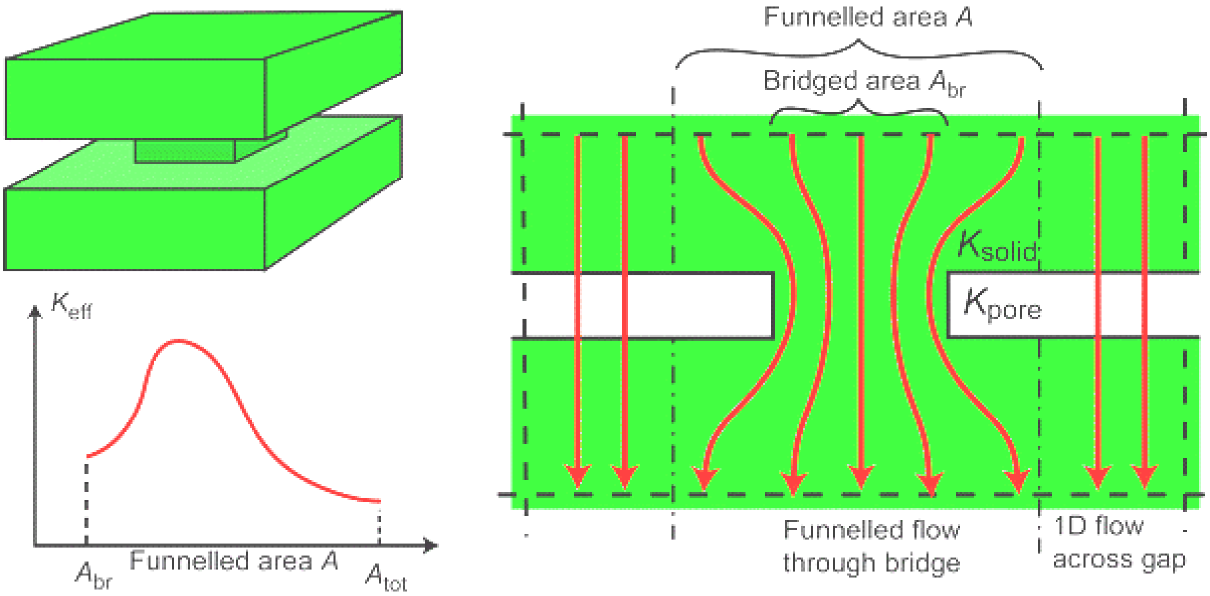

Figure 3-3 Schematic representation of the two flux regime model showing heat flow through solid splats connected by bridges [178, 183].

Further work has combined the sintering model of Cipitria et al. [178, 179], which is based on the same geometrical model, with the two flux regime model in order to predict changes in thermal conductivity with heat treatment. Resulting comparison between model prediction and measurements (made at room temperature) plotted against time of exposure at 1400°C is shown in Figure 3-4. Pore size distribution (whether mono-disperse pore size of 125 nm or bimodal of 50 nm and 200 nm) is shown to have a significant effect on the kinetics of sintering. Increases in fine scale porosity accelerate the initial growth of contact bridges. Overall, it is evident that experimental conductivity data show some scatter. Values are very sensitive to initial pore architecture and hence are dependent upon fabrication parameters. Whilst it is possible to identify trends, comparison of absolute values is difficult, particularly across different measurement techniques.

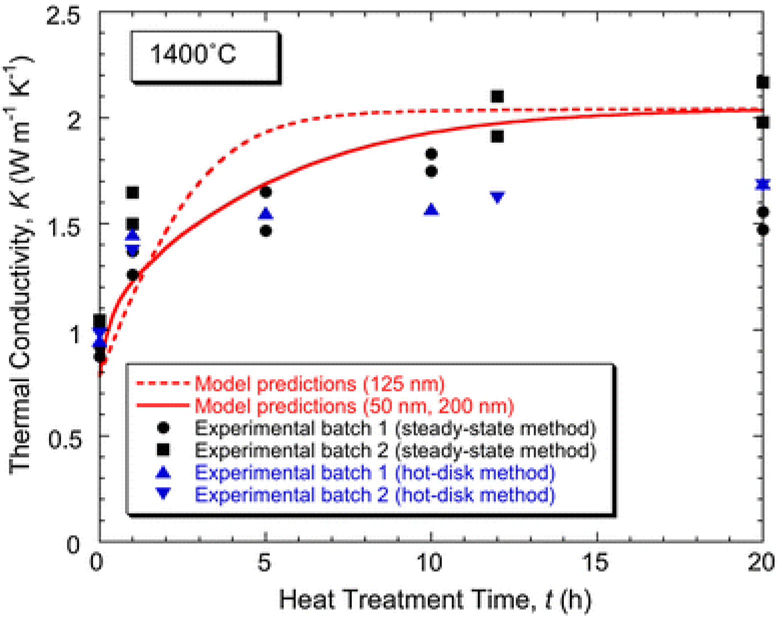

Figure 3-4 Comparison between predicted and experimental change in thermal conductivity of PS YSZ due to heat treatment at 1400°C [178, 183].

3.4 Effect of Impurities on TBC Sintering

There is growing concern over the effect of impurities on the sintering rate, notably silica and alumina, which are commonly present in spray powders. Studies suggest that silica may accelerate the rate of coating densification via a mechanism similar to liquid phase sintering [17, 192], which involves the creation of vitreous phases with low viscosities, which enhance mass transport, mainly at the grain boundaries [193]. The glassy phase is able to more effectively redistribute species by capillary forces, which in general is much faster than by solid state diffusion (surface, grain boundary or lattice) alone (see section 4.2 for further details). Impurities also enhance the rates of surface and grain boundary diffusion [177]. The postulate is consistent with observations made by Eaton et al. [194], Chen et al. [195] and Stemmer et al. [196], the latter having reported amorphous silica-rich phases at triple grain junctions (with silica addition of ~ 0.1 wt.%). Even if concentrations of such vitreous phases at segregation points (usually at grain boundaries or intersplat boundaries) are too low to locally induce viscous flow, the diffusion rates in such phases will be high and hence it is still expected to increase the rate of solid-state sintering [172]. Even at moderately low temperatures, the increase in the contents of alumina and silica, from < 0.1 to 0.26 wt.% and from < 0.01 to 0.69 wt.% respectively, data presented by Rejda et al. [162] show that the coating creep and deformation rate is significantly accelerated by changing the surface conditions of the microcracks involved in the compaction and sliding processes. Work by Xie and Paul et al. [172, 177] on free-standing PS YSZ coatings reported that reducing the contents of alumina and silica, from ~ 0.1 – 0.2 wt.% down to ~ 0.01 – 0.05 wt.%, significantly reduced sintering rates (which may be monitored by changes in thermal conductivity, as shown in Figure 3-5).

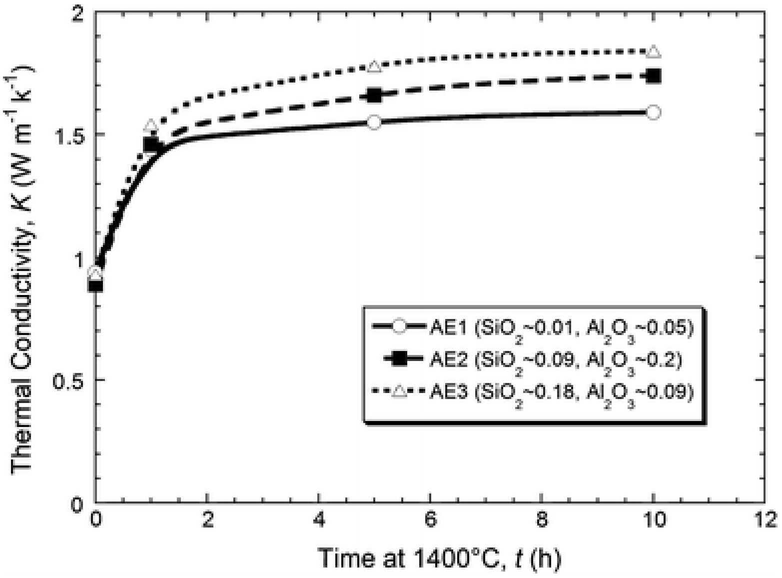

Figure 3-5 Changes in thermal conductivity due to isothermal heating at T = 1400°C for varying coating impurity levels [172].

3.5 Sintering of PS TBCs Constrained by a Substrate

Most sintering-related measurements have been conducted on free-standing coatings. Under service conditions, TBCs are attached to a rigid substrate, subject to high thermal gradient and rapid heating and cooling cycles. Tensile stresses in the TBC caused by the constraint imposed by the substrate may retard the coating sintering rate by opening up microcracks [163, 197, 198]. However, work by Cipitria et al. [179] has shown that the constraint by a substrate does not in fact alter coating sintering (and hence the stiffening) behaviour very much at temperatures exceeding ~ 1200°C since creep relaxation readily takes place. Moreover, non-densifying (surface diffusion) sintering mechanisms are unaffected by attachment to a substrate, and these mechanisms tend to play a dominant role in the overall microstructural changes (and hence the changes in mechanical properties) taking place. However, rapid thermal cycling may generate local stresses that cause microcracking of sintering necks, which may retard the progression of the sintering related microstructural changes [114].

3.6 Effect of Thermal Cycling on Sintering

Thermal cycling may cause an initial flaw to grow to a critical size from fatigue cracking. Zhu et al. [156] have quantified a crack propagation rate for a particular regime of thermal cycling (10 – 20 mins) with a thermal gradient (using a laser thermal fatigue test, with maximum surface temperature achieved being around 1300°C). The initial (interfacial) crack propagation rate was estimated to be 5 – 8 microns/cycle. However, for longer testing times, it is unclear whether the observed interfacial degradation is due to propagation of sub-critical interfacial cracks or due to the growth of a TGO. Sintering of the top coat also cannot be discounted for longer heat treatment times. Overall, it is unlikely that thermal cycling alone (at least at moderate temperatures) can cause substantial degradation of the interfacial fracture properties.

Kokini et al. [82, 199] have suggested a mechanism by which segmentation cracks may be initiated in TBCs under service conditions. The initiation is related to the stress relaxation, which occurs at the top surface of coatings at high temperatures, followed by subsequent cooling in a thermal gradient. The study examines an analytical model of a TBC on a metallic substrate (which is internally cooled so that a large thermal gradient is created) and then the TBC surface is subsequently cooled (simulating engine shut down). Initially, when the TBC surface is heated, the TBC is under residual compression due to the thermal gradient. This stress then relaxes at the surface, by creep processes, as steady-state conditions are attained. Upon cooling, modelling results showed that the coating surface rapidly goes into tension. These results are later confirmed by experimental studies, which use a high power laser in order to subject the specimen to a high heat flux [45, 199, 200], and upon cooling, some initiation and propagation of segmentation cracks were observed. Further propagation of cracks is likely to be driven by subsequent thermal cycling and top coat sintering. Sintering will take place the fastest at the coating surface in the presence of a thermal gradient [180] because it is the hottest part.

3.7 Phase Destabilization of Yttria-Stabilized Zirconia (YSZ)

The phase stability of the YSZ after prolonged heat treatment is an important issue. One limitation arises from the partitioning of supersaturated metastable tetragonal (t') phase into the equilibrium phases (by diffusion of Y atoms into low-yttria tetragonal and high-yttria cubic phases), and the potential for undesirable transformation of the depleted tetragonal phase into the monoclinic phase upon cooling [201]. The associated volume expansion, due to this martensitic transformation, of around 3 – 5 %, may result in extensive microcracking and coating degradation [72]. Ilvasky et al. [68] showed that after 1000 h at 1200°C, the monoclinic phase content of a PS 7YSZ coating increased to 10 wt.% and after 400 h at 1400°C, the monoclinic phase content was measured to be around 35 wt.%. Such destabilization behaviour is also dependent upon the cooling rate [202, 203]. Moon et al. [202] have shown that faster cooling rates reduce the likelihood of the monoclinic transformation. In the presence of a thermal gradient, destabilization is more likely to occur near the free surface since it is hotter [180].

It is also known that thermochemical reactions with CMAS and other impurities can dramatically increase the rate of YSZ destabilization [21, 204-208]. Effects due to CMAS-accelerated sintering are often far more serious compared to the effects of solid state sintering alone, and therefore, should large volumes of the coating undergo transformation into the monoclinic phase (from high levels of CMAS contamination), it is possible that the coating durability may be significantly reduced (for further details see Chapter 4.0).

4.0 Adhesion and Degradation by Calcia-Magnesia-Alumina-Silica (CMAS) Deposits

During operation, the surface of the TBC may become contaminated with environmental deposits that are ingested into the gas turbine engine. Contaminant particulates, such as sand, volcanic ash or fly ash, commonly comprise calcia-magnesia-alumina-silica compounds, which are termed collectively as "CMAS". In the first part of this chapter, the adhesion characteristics of particulates onto turbine internal surfaces are discussed. In the following section, the degradation effects caused by the ingression of molten CMAS into TBCs are discussed. The ingression of CMAS accelerates sintering, and has been observed to adversely affect the thermomechanical stability of the TBC (in both PS and PVD coatings) [208-212]. CMAS infiltration is also known to degrade the insulating properties of the TBC [213, 214]. These effects are likely to be of greater concern as engine operating temperatures are pushed higher. Finally, some research into novel TBC compositions that mitigate CMAS attack is reviewed.

4.1 Deposition Behaviour of Ingested Particulates Inside a Gas Turbine Engine

Ingested particulates, such as sand, fly ash and volcanic ash, often referred to generically as calcia-magnesia-alumina-silica (CMAS), can cause significant problems in both types of turbine (for power generation and for propulsion). Such particles may melt, or at least soften, in flight, making it more likely that they will adhere to surfaces within the turbine on impact. Increased turbine entry temperatures clearly raise the danger of this happening. There is thus considerable interest in identifying and quantifying the factors affecting the likelihood of particles adhering to surfaces within the turbine (rather than simply passing through the engine) since it is clear that such adhesion can rapidly lead to severe component degradation. In the combustion chamber, where the flame temperature may be as high as 1650°C, silica-based slag deposits have been observed to plug combustor liner cooling holes, thus creating hot spots that can lead to premature failure [215]. Deposits can also form on blade surfaces and along nozzle guide vanes, causing local overheating [216]. Deposition can also accelerate the corrosion of turbine components as they may come in direct molten contact with corrosive elements [217]. The melting (or softening) point of CMAS varies with its composition, and so if the particulate temperature, at the point of impact is below the softening point, erosion may be the prevailing damage mechanism. Both deposition and erosion are also known to increase component surface roughness, which may cause increases in heat transfer (up to 50%) and skin friction (up to 300%) [218].

Effects of CMAS-related degradation of TBCs are discussed in later sections 4.2 and 4.3 in some detail.

Three main factors affect the likelihood of particulate deposition. These are the gas temperature, particle temperature and the turbine surface temperature, at the point of impact. The gas temperature determines the particle temperature, which in turn determines the physical state of the particles; solid, liquid or partially molten - and in the latter case the melt fraction becomes significant. The state of the particle influences whether they rebound from the surface (causing erosive damage) or instead are likely to deposit.

Several mechanisms for the particle delivery to turbine surfaces have been identified. These include inertial impaction, turbulent diffusion/eddy impaction, Brownian diffusion and thermophoresis [217, 219-223]. Inertial impaction applies to larger particles, which have sufficient mass to deviate from the turning gas streamlines and subsequently impact onto engine surfaces. Turbulent diffusion and eddy impaction are where smaller particles (but still with sufficient mass to be delivered by inertial effects) are entrained in the turbulent eddies within surface boundary layers and impact the surface. For much smaller particles, transportation is possible by impacts with thermally agitated gas molecules in the surface boundary layers, and the random impacts produce Brownian diffusion delivery to the surfaces. Thermophoresis takes place when the surface is cooled and the energy of the random impacts from thermally agitated molecules in the thermal boundary away from the surface is higher. This produces a net average impact force from gas molecules in the direction towards the surface.

It is widely accepted that the trajectory of a particle carried through the gas turbine is primarily dependent on the particle Stokes number, $\mathrm{Stk_p}$. This is derived from taking the ratio of the particle time scale to the flow time scale. The particle time scale is a measure of particle inertia and denotes the time scale with which any slip velocity between the particle and the fluid is equilibrated:

$$\mathrm{Stk_p} \approx \frac{\rho_\mathrm{p} D_\mathrm{p}{}^2 U_\mathrm{p}}{18 \mu_\mathrm{f} L_\mathrm{c}} \qquad \textit{Equation 4-1}$$

where U_p is the particle velocity, D_p is the particle diameter, ρ_p is the particle density, L_c is the characteristic length of the flow (e.g. duct diameter) and μ_f is the gas dynamic viscosity. A large Stokes number indicates that the particle’s inertial response to the surrounding flow is slow, whereas if the Stokes number is much less than unity, it is expected that the particle will closely follow the streamlines of the carrier gas. For example, the Stokes number, as obtained using Equation 4-1, and taking the free stream velocity inside a typical gas turbine to be approaching sonic speeds ~ 300 m s^{-1}, particle density (e.g. of silica sand) to be ~ 2650 kg m^{-3}, gas viscosity to be 4.4×10^{-5} kg s^{-1} m^{-1} and obstacle dimension to be 10 mm, has a value of about 1,000 (representing a strong tendency to deviate from the gas streamlines) for a particle diameter of 100 µm, but a value of about 0.1 (representing a strong tendency to follow streamlines) for a particle diameter of 1 µm.

Hamed et al. [219] presented a particle delivery model, in order to assess the relative rates of delivery for each of the dominant turbine deposition mechanisms. The model showed that Brownian diffusion was the dominant deposition mechanism for particles less than ~ 0.1 µm, and deposition was gradually enhanced by turbulent diffusion and eddy impaction as particle size increased. With further particle size increase (> ~ 10 µm), inertial impaction was found to dominate. The study also showed that deposition efficiency generally decreased as particle size decreased.

Other studies have concentrated on the effect of component surface temperature on deposition efficiency. Walsh et al. [223] studied the deposition behaviour of bituminous coal ash on a heat exchanger tube. The surface temperature of the metal coupon was found to be highly significant. Initially they found that only molten particles would stick to the clean surfaces, solidifying soon after impact. However, as the metal temperature increased beyond 1000°C, it was found that the particles melted on impact or melted shortly after impact. The combination of increased metal temperature from the deposits already adhered to the surface, and the increased roughness of the surface caused subsequent particles to have a higher probability of adhesion.

A few studies have examined particle deposition characteristics using an accelerated deposition test facility (aimed to simulate conditions inside a gas turbine). Jensen et al. [224] used a Turbine Accelerated Deposition Facility (TADF), which was designed in order to simulate deposition, in an accelerated manner. They simulated 10,000 h of turbine operation in just 4 h by increasing the particulate concentration. Deposition was simulated by injecting particulate into a natural gas combustor. The methodology was validated by inspecting the coupons subjected to accelerated deposition, by microscopy and x-ray analyses, which showed similarities with actual deposits found on off-service turbine components. Bons et al. [217] studied deposition characteristics of fly ash (see section 4.3 for details), using a similar test facility matching the gas temperature and velocity of modern first-stage high pressure turbine vanes. Ash particles were accelerated to a combustor exit flow of around 180 m s^{-1} before impinging on coupons coated in TBCs, with surface temperature of around 1150°C. The effect of gas stream temperature was also studied by placing coupons at different streamwise locations after the combustor exit. It was noted that the upstream specimens operating at gas temperatures ~ 1100°C experienced one to two orders of magnitude higher deposition rates compared to the downstream specimens operating at gas temperatures ~ 980°C. Chemical variations in fly ash samples caused deposit thickness and structure to vary widely. In all cases, corrosive elements (e.g., Na, K, V, Cl, S) were found to penetrate the TBC layer during the accelerated deposition test. There may be scope for reducing the degradation caused by deposition of fly ash by controlling fuel purity.

Crosby et al. [225] used the TADF to study independent effects of particle size, gas temperature and surface temperature on the deposition of coal ash. The deposition rate increased by more than a factor of two as the mean particle diameter was increased from 3 μm to 16 μm (all other factors being equal). Particle deposition rate was found to decrease with decreasing gas temperature, and the threshold gas temperature (below which no deposition was observed) was found to be around 960°C. This temperature, however, is likely to depend heavily on the physical and chemical properties of the ash. Deposit surface roughness was found to increase with increasing surface temperature, which is consistent with the trend that rougher and hotter surfaces are more efficient at capturing impinging particulates. This work also points towards the importance of blade cooling in order to minimize damage to the TBC from CMAS adhesion.

Ai et al. [226] conducted a study using the TADF to investigate deposition behaviour near film cooling holes on a high pressure turbine vane. Film-cooled coupons were placed in the path of a particle-laden exhaust flow and the surface temperature and coverage were monitored over time. Results showed that increased deposit height resulted from increased surface temperature, which in turn increased the deposition rate (in a non-linear manner). They also concluded that increased film cooling blowing ratio resulted in a decrease in surface temperature, which reduced deposition, particularly in the coolant wakes. Ai et al. [216] also compared these experimental findings with 3D numerical simulations. The deposition model predicted that initially, smaller particles have a greater tendency to stick. However, after the initial deposition had taken place, the rise in surface temperature allows larger particles to also deposit. Adhesion of larger particles will then tend to dominate and thus contribute most to the delivery rate. Predictions of capture efficiencies, concerning different coolant blowing ratios, were also found to be in good agreement with the experiment.

Rozati et al. [227] investigated the effect of particle size and coolant blowing ratios on the deposition and erosion behaviour of combustion fly ash, using a large eddy simulation model. The model predicted that smaller particles (~ 1 μm), with particle Stokes number of 0.03, tended to follow the streamlines around the turbine leading edge, and therefore not reach the blade surface. Larger particles (~ 10 μm), with a substantially larger particle Stokes number of 3, were predicted to impinge on the blade surface, with blowing ratio having minimal effect. Intermediate particle sizes were found to show some receptivity to the level of surface coolant flow, and overall there was a trend of decreasing percentage of particles being deposited with increased coolant blowing ratio. Erosion, on the other hand, was found to be highest around the cooling holes and was mostly attributed to particles with average diameters of 5 μm – 7 μm. This was because a threshold ash softening temperature was assumed to determine the state of particles on impact (which decides whether particles erode or deposit), and such intermediate particle sizes were found to have enough inertia to impact, whilst not being hot enough to deposit.

4.2 TBC Degradation by Molten CMAS Ingression and Liquid Phase Sintering

It is known that, following CMAS adhesion, the ingression of molten CMAS can damage the chemical and mechanical stability of TBCs, and these effects have been extensively studied in recent years [131, 208-212, 228-234]. Degradation arises when molten compounds (with low melting points, typically no more than ~ 1220°C [209, 228, 235-237]) adhere to the coating surface, and subsequently penetrate into the coating during extended exposure to high temperatures.

At sufficiently high temperature and concentration levels, CMAS liquid firstly creates a CMAS-rich outer layer. It then infiltrates pores and cracks by viscous flow (driven by capillarity) and may also diffuse along grain boundaries. CMAS oxides do not, in general, readily dissolve in the zirconia lattice, but tend to form vitreous phases which wet the crystalline grains at the boundaries [193], where they accelerate (diffusional) sintering, and also encourage intersplat sliding and creep deformation [162, 238, 239]. Such flow of CMAS glass is only possible at high temperatures, when its viscosity is low (although this will also be composition dependent). Glassy flow is driven toward the sintering necks [239], which may lead to shrinkage (by a mechanism similar to liquid phase sintering).

There are essentially four different stages in the general densification process of liquid-assisted sintering, as outlined in Figure 4-1 [240]. Firstly the reactive liquid forms in Stage 0. Stage I involves the rearrangement of the liquid and solid driven by capillary forces. This process results in a substantial loss in porosity. If sufficient levels of liquid are present, full densification is possible (Stage III). On the other hand, at intermediate liquid concentration levels, solution-reprecipitation takes place (Stage II), where mass transport through the liquid primarily drives densification. The solid dissolves at the contact points and diffuses out through the liquid film, mainly via the grain boundaries. This causes the particle centres to move closer together, leading to densification. The final stage of liquid phase sintering may be subsequently followed by processes such as grain growth and phase transformation etc. A key factor which affects the rate of liquid phase sintering is the solubility of the solid in the liquid. In order to achieve a highly dense material, high solid solubility in the liquid and low liquid solubility in the solid is ideal [240, 241]. It is clear from studying the effects of liquid phase sintering that CMAS-assisted sintering of TBCs, at temperatures above its softening point, will cause detrimental loss in its compliance, which makes it prone to failure by spallation.

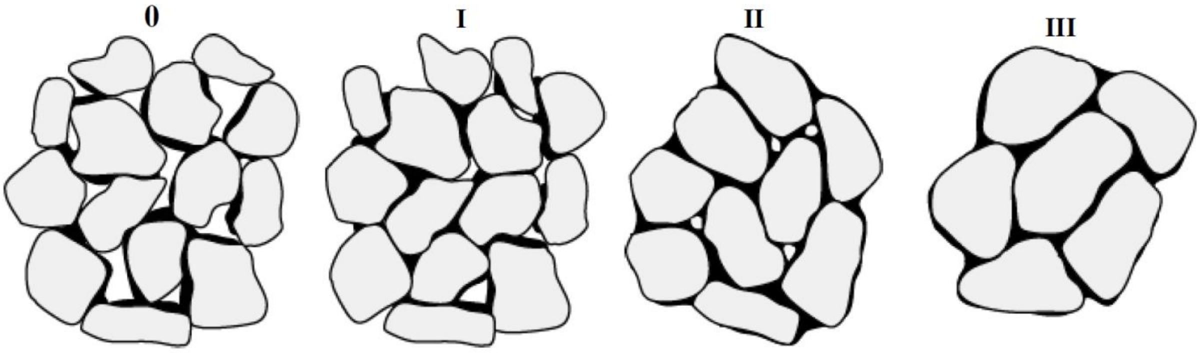

Figure 4-1 Schematic diagram of the stages of liquid phase sintering, 0: melting; I: rearrangement; II: solution- reprecipitation; III: pore closure (full densification) [240]

The thermochemical aspects of CMAS degradation in TBCs was first investigated in depth by Krämer et al. [208]. His model CMAS composition was 33.2 CaO–6.5 MgO–11.9 Al_2O_3–48.5 SiO_2 (wt.%). The study shows that, as soon as CMAS melting takes place, rapid dissolution and reprecipitation of the 7YSZ occurs. The CMAS melt dissolves the metastable tetragonal (t') phase, causing the CMAS glass adjacent to the zirconia grains to become locally enriched in Zr^{4+} and Y^{3+}. Similar observations were made by Aygun et al. [207] on APS YSZ coatings. Bacos et al. [242] used a CAS melt, with composition 23.5 CaO–15 Al_2O_3–61.5 SiO_2 (wt.%), on 7YSZ EB-PVD coatings. As well as the usual dissolution and reprecipitation effects, 4 h of heat treatment at 1200°C resulted in the formation of new crystalline phases, which were identified as $Ca_2ZrSi_4O_{12}$ and $CaAl_2Si_2O_8$ (anorthite). It was observed by Drexler et al. [243] that it only takes a small amount of Zr^{4+} to saturate the CMAS glass, whereas the solubility of the Y^{3+} is much higher. If, for example, the concentration of Y^{3+} were high enough, the accumulation of it in the glassy melt would cause crystalline phases to be formed, resulting in the arrest of any further CMAS infiltration [234]. However, the stabilizer concentration in 7YSZ is not enough to induce crystallization. Instead, as a result of Y^{3+} being leached out from the metastable tetragonal phase, at high temperature, the equilibrium tetragonal phase forms, and upon cooling zirconia grains are precipitated out in the stable monoclinic phase, with a characteristic spherodized grain structure [208, 232, 243]. Figure 4-2 shows cross-sectional SEM images taken by Drexler et al. [244], demonstrating that complete infiltration of CMAS glass across the entire thickness of the coating (~ 200 μm) takes place after 24 h at 1200°C. In most of these studies, the residual CMAS was largely amorphous upon cooling. The cooling may also induce large differential thermal expansion misfit strains between the solid CMAS/heavily CMAS-infiltrated YSZ layer (~ 8×10^{-6} K^{-1} [211]) and the relatively undamaged underlying YSZ layer (~ 11×10^{-6} K^{-1} [10]). This may lead to large residual stresses being induced, which may be sufficient to drive cohesive spallation failure [208, 209, 228, 232, 234]. In general, the mechanisms involved in CMAS penetration (both thermochemical and thermomechanical processes) into the 7YSZ TBCs are complex, and so simple models relating to porous-medium viscous flow and wetting cannot be used to describe or predict such effects.

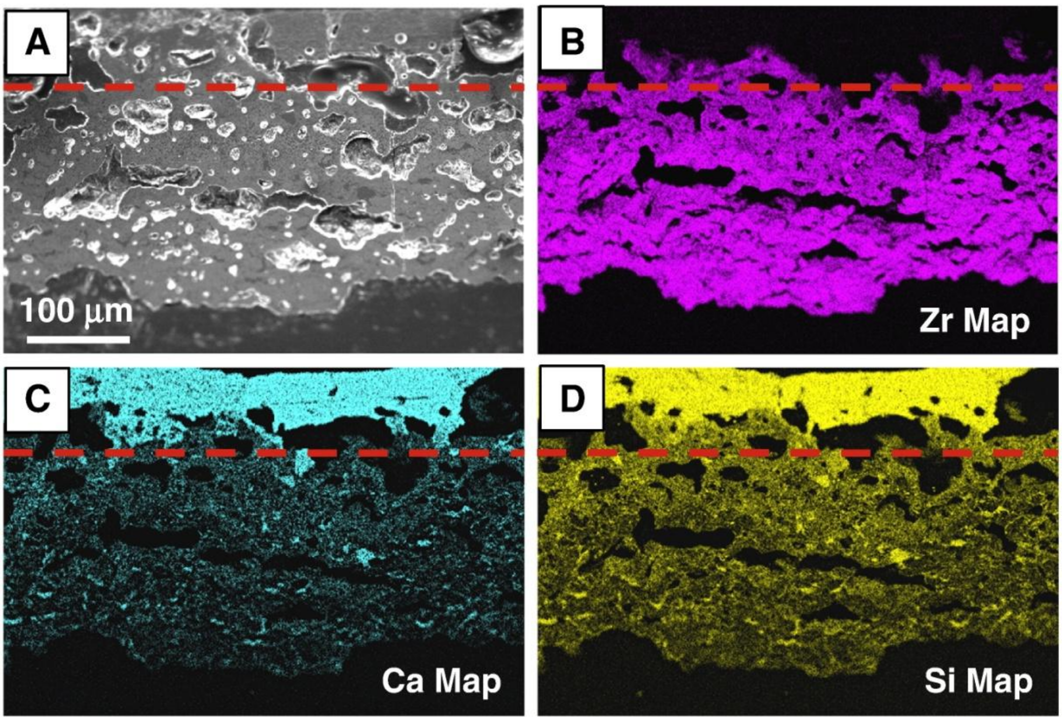

Figure 4-2 (A) Shows cross-sectional SEM micrograph of APS 7YSZ TBC with CMAS on top that has been heat-treated at 1200°C for 24 h, showing the complete penetration of the TBC (penetration depth of ~ 200 microns). The dashed red line indicates the original top surface of the TBC. Images (B), (C), and (D) are corresponding Zr, Ca and Si EDX elemental maps [244].

Several researchers [206, 210, 228, 237], have inspected removed aerofoil and stationary components where extensive CMAS penetration into the TBC was observed (particularly in the hottest parts) and delamination had taken place as a result of accelerated sintering and increased thermal stresses experienced during turbine operation. Observations of field specimens are roughly consistent with simulated exposures in the laboratory, although it is hard to draw mechanistic conclusions due to many unknown variables, such as thermal history and CMAS exposure levels. In addition to delamination failure, Vidal-Setif et al. [206] also reported the formation of vertical cracks (enlarged inter-columnar gaps), presumably formed due to sintering of the TBC columns which resulted in mud-cracking upon cooling. They also reported the formation of new crystalline phases, which were identified as $Ca_2Zr_5Ti_2O_{16}$ (calzirtite) or $Ca_2Zr_2Ti_4O_{14}$ (zirconolite). Whether these reaction products play a significant role in affecting the penetration behaviour of CMAS remains unclear.

4.3 TBC Degradation by Volcanic Ash and Fly Ash

Aviation engines may encounter, not only low levels of particulate debris in the atmosphere, but volcanic ash that may linger at aircraft cruise altitude (30,000 – 50,000 ft). Volcanic ash typically consists of sharp mineral particulates of varying particle sizes (measuring anything from ~ 100 μm down to a few nanometres), with compositions broadly consisting of SiO_2, Al_2O_3, CaO, Fe_2O_3, MgO, with traces of Na_2O, K_2O, P_2O_5, TiO_2 and MnO, largely depending on the nature of the surrounding geology [245-247]. Whilst improved monitoring and tracking of volcanic ash clouds and guidelines for no-fly zones (when ash concentration is above 4 mg m^{-3} [248]) are leading to improved avoidance strategies, it is recognized that low level exposure to volcanic ash in the atmosphere is probably inevitable. Just like CMAS, molten volcanic ash could form glassy deposits on combustor walls, turbine inlets and on the TBC surface. Deposits may block cooling passages and induce spallation of TBCs through creation of a densified layer. Ash may also contaminate the engine fuel. Fan, compressor blades, wing leading edge and tail rudder will suffer from severe erosion. Exterior pitot tubes may also become blocked, with catastrophic implications for navigation control [246]. Furthermore, plumes produced from explosive eruptions travel at high speeds, reaching cruise altitude within minutes.

The explosive eruption of the Eyjafjallajokull volcano in Southern Iceland in April 2010 caused serious disruption to European air traffic for weeks. A typical elemental composition (bulk) of an explosive volcanic ash is shown in Table 4-1. This is of course, only a very approximate composition. However, it is immediately obvious that natural volcanic ash exhibits much greater chemical complexity than synthetic “laboratory grade” CMAS, which is often used in research. It was found that the Eyjafjallajokull ash had an approximate melting point (T_m) of around 1160°C, although presumably this would be from taking the average of a range of melting points due to a number of distinct crystalline phases present. The main crystalline phases were identified as plagioclase solid solution, with traces of feldspar $KAlSi_3O_8$ and quartz (SiO_2) with pyroxene and other minor phases [247, 249, 250]. It must be emphasized that, in general, volcanic ashes are rapidly quenched (due to an explosive reaction with moisture at the vent surface) and therefore predominantly consists of a glassy phase, with only a minor proportion made of crystalline components. The glass transition (T_g) of a specimen of volcanic ash would therefore vary over a wide range, depending on composition. Therefore broadly speaking, a particular CMAS specimen (of which volcanic ash may be considered as a variant) may be characterised by (a) the crystalline phases present (which affects T_m), (b) the T_g of the glassy part and finally (c) the relative proportion of the glass to the crystalline phases.

Composition (wt.%)	Explosive Ash (bulk)
O	bal.
Si	27.1
Al	7.8
Fe	7.6
Mg	1.4
Na	3.7
Ca	3.9
C	1.1
K	1.5
Ti	1.1
P, Cl, F	traces

Table 4-1 Typical elemental (bulk) composition of an explosive volcanic ash specimen [247].

The large fraction of amorphous phase present in volcanic ash is one of the main reasons why ash contamination is thought to inflict greater damage on TBCs, at a given temperature, compared to “laboratory grade” CMAS. Whilst synthetic CMAS (with mainly crystalline phases) typically has a melting point of around 1100°C – 1200°C [208, 236], volcanic ash, with generally much higher Si content combined with oxide mixtures of Fe, Na, K and Ti etc., tends to exhibit a much lower range of T_g [229, 249, 250]. Thus volcanic ash is expected to soften at lower temperatures, and therefore is likely to more aggressively infiltrate the TBC at a given operating temperature.

An XRD profile and a DSC plot, taken from an artificial volcanic ash specimen (AVA), which was modelled on approximate oxide proportions published of the Eyjafjallajokull volcanic ash [249], are shown in Figure 4-3 and Figure 4-4. It is clear from the XRD profile that the AVA consists of a large amorphous phase, with a small fraction of crystalline phases which have been identified. Even peaks which have been indentified are broad and weak, indicating poor crystallinity, which is representative of real volcanic ashes. The DSC plot elucidates two thermal effects. The T_g may be identified at around 930°C, whilst a second endothermic peak is observed at around 1300°C. This is the melting peak, which is broad and the plot suggests that melting onset actually starts at temperatures just below 1200°C. This is not surprising, since there are a number of crystalline phases present.

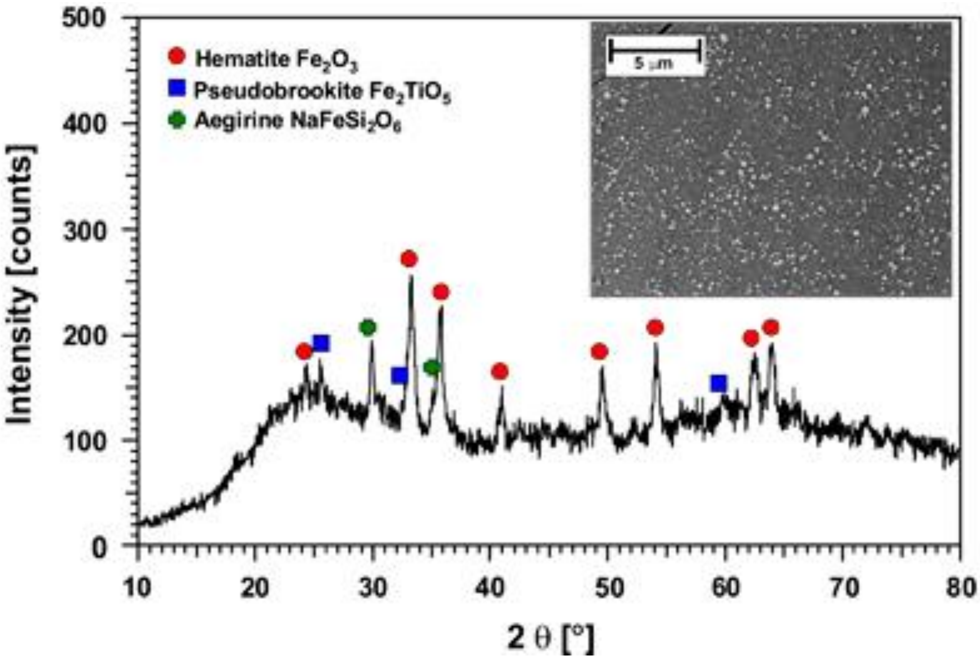

Figure 4-3 X-ray diffraction profile of as-processed artificial volcanic ash. Crystalline constituents include hematite Fe_2O_3, pseudobrookite Fe_2TiO_5, and aegirine-type clinopyroxene $NaFeSi_2O_6$. The inset SEM image shows a polished cross section of AVA after annealing at 800°C, which shows that nano-sized precipitates, presumably hematite Fe_2O_3, are embedded in a dark contrasted matrix representing the dominating amorphous part of AVA [249].

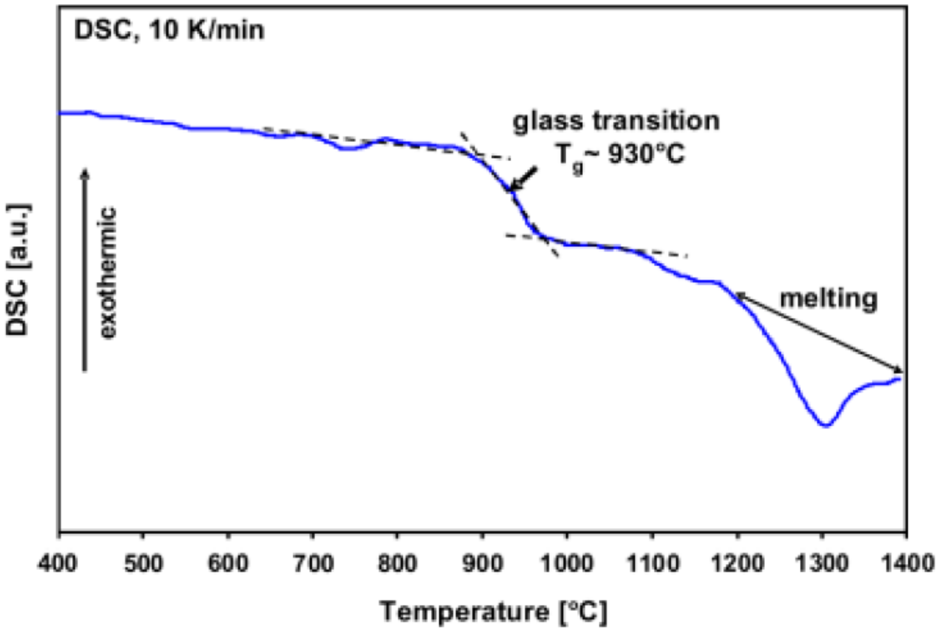

Figure 4-4 Differential scanning calorimetry (DSC) of artificial volcanic ash in the 400 – 1400°C temperature range (heating). There is a glass transition at approximately 930°C and the melting onset at around 1180°C [249].

Another source of CMAS-type deposits worth mentioning is syngas fly ash. Natural gas-fired turbine engines are one of the most efficient methods of generating electricity [230]. An integrated gasification combined cycle (IGCC) creates synthetic H_2-rich gas fuel (syngas), using energy generated by coal. Syngas is then used to generate electricity. The additional heat generated from syngas-fired turbines is often used to run additional steam turbine generators, which therefore makes the overall thermal efficiency as high as 60% [230]. However, the downside of this process is the production of fly ash, which results during the combustion of coal. Fly ash is primarily made of silicates, and have been reported to adhere to or erode the surface of the TBCs and cause damage, just like other CMAS-type deposits [217, 225, 227, 251].

Mechnich et al. [249] studied the thermochemical interaction between artificial (synthesized) volcanic ash (AVA), based on the composition of the Eyjafjallajokull ash (its XRD profile and DSC plot are shown in Figure 4-3 and Figure 4-4) and EB-PVD 7YSZ. It was shown that, as soon as the ash is exposed to a temperature above its T_g, it softens and exhibits viscous flow. When heat treated for 1 h at 1200°C, complete wetting and penetration of the glassy AVA was observed. Since the AVA, like CMAS, acts as a solvent for Y_2O_3, the yttria content in the YSZ was observed to decrease, although no monoclinic phases were detected, probably due to the short heat treatment time. Instead, however, the formation of a new crystalline phase, $ZrSiO_4$ was detected. The crystallization of $ZrSiO_4$ is significant, since the reaction in the binary ZrO_2-SiO_2 system at 1200°C is expected to be extremely sluggish

[252]. It seems that in this case, the presence of the Y_2O_3 had increased their reactivity. The formation of $ZrSiO_4$ has not been reported in similar CMAS studies, although this may be because the AVA environment, unlike the laboratory grade CMAS, provides a sufficient saturation of SiO_2. The $ZrSiO_4$ was observed to have nucleated at the interface between the Y_2O_3 enriched amorphous phase and the residual ZrO_2. Interestingly, EDS analyses gave no evidence for the uptake of MgO and CaO by the YSZ, which are also common stabilizing agents. It is likely that under these conditions, the dominating driving force for diffusion is the concentration gradient of Y_2O_3, whereas MgO and CaO are presumably located in thermodynamically stable environments. With longer heating times, the thermomechanical stability of the coating would no doubt, have been compromised due to increase in in-plane stiffness. This study shows that the wetting and infiltration behaviour of AVA differs from the standard CMAS ingression behaviour reported in literature [208, 236]. It was found that the onset temperature for interaction is much lower in the case of AVA, and this is because AVA exhibits considerable softening above its glass transition, rather than a well defined melting point. Hence infiltration was observed to occur by gradual viscous flow. It is, however, important to note that ashes from different volcanic provinces would exhibit vastly different chemical and physical properties, and thus any study conducted on the chemical interaction between it and 7YSZ is case-specific. It is therefore difficult to come to a general conclusion on the impact of volcanic ash on TBC performance, and further experimental work is required.

Gledhill et al. [230] investigated the thermochemical reactions between a sample of lignite fly ash and APS 7YSZ. Whilst the details of the mechanisms would inevitably depend on the microstructure of the TBCs, in general, the degradation caused by fly ash was found to be very similar to the effects caused by CMAS and volcanic ash - see schematic in Figure 4-8. Whilst there was definitely some evidence of the dissolution of Y_2O_3 by the molten fly ash, no formation of the monoclinic phase, or any new crystalline phases, were observed. It was also found that the residual fly ash was largely amorphous on cooling and very little change in its composition was detected as it progressively infiltrated the TBC.

In general, it is clear that the long term effects of CMAS-type contaminants on the thermomechanical performance of TBCs (which are in reality experiencing thermal gradients and ill-defined temperature histories), is yet to be determined. Understanding these effects are crucial to the development of next generation TBCs, which should be able to resist CMAS attack. Several developments in this area are notable in the last decade, and a few of these are explored in the following section.

4.4 Novel TBC Materials that Mitigate CMAS Attack

Some approaches for mitigating CMAS attack on 7YSZ TBCs have been reported in literature [207, 230, 233, 243]. The most promising strategy so far suggested is to modify the TBC composition (and/or structure) so that it will induce crystallization of the CMAS and arrest its penetration. Aygun et al. [207] reported on the performance of a TBC composition such that up to 20 mol.% of Al_2O_3 and 5 mol.% of TiO_2 were incorporated as a solid solution into 7YSZ. The deposition of this particular composition was carried out by SPPS (solution-precursor plasma-spray). When the TBC comes into contact with CMAS glass, the Al- and Ti-bearing solutes become incorporated within it. The rapid accumulation of Al in the CMAS glass shifts the glass composition from the pseudo-wollastonite ($CaSiO_3$), which is difficult to crystallize, to the anorthite ($CaAl_2Si_2O_8$), which crystallizes easily. The presence of the Ti helps the crystallization process by promoting nucleation. This leads to the arrest of the infiltrating CMAS front. The mechanism is summarized in the schematic illustration shown in Figure 4-7. After 24 h exposure at 1121°C, the CMAS was found to penetrate into the YSZ+Al+Ti coating by around 70 μm (into a 250 μm thick coating). This can be seen from the cross sectional SEM micrograph of the resulting microstructure and its corresponding EDS mappings of Zr, Si and Ca, shown in Figure 4-5. A line scan of the compositional profile of Si and Al along line X-Y in Figure 4-5 is shown in Figure 4-6. The Al and Si signals are strong near point X, due to the high concentrations present in the CMAS glass. Whilst the average signal of Si remains steady with distance from point X, the Al signal increases until there is a spike observed at point Z. This spike in the Al content corresponds to the front where the CMAS infiltration is arrested. On the other hand, CMAS was found to have completely infiltrated conventional TBCs of 7YSZ composition under the same exposure conditions.

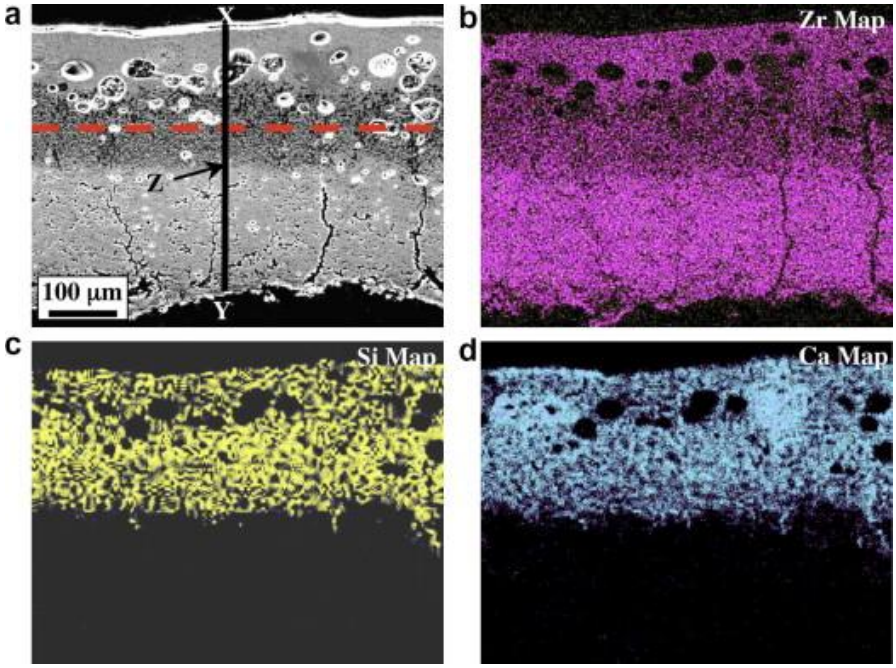

Figure 4-5 (a) Cross-sectional SEM micrograph of SPPS (YSZ+Al+Ti) TBC that has interacted with CMAS glass (for 24 h at 1121°C), and corresponding elemental maps: (b) Zr, (c) Si and (d) Ca. The horizontal dashed line in (a) corresponds to the top of the original TBC. The vertical line in (a) denotes the approximate path of the EDS line scan shown in Figure 4-6.The "Z" denotes the leading edge where the CMAS-glass front appears to have arrested [207].

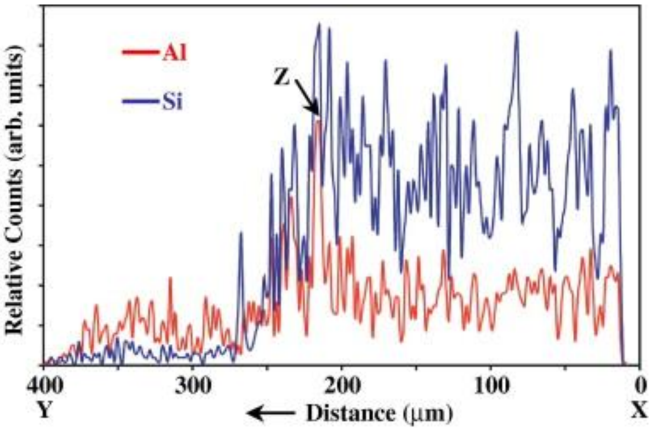

Figure 4-6 EDS line scan from X to Y (see Figure 4-5) showing relative counts for Al and Si in SPPS (YSZ+Al+Ti) TBC that has interacted with CMAS glass (for 24 h at 1121°C). The spike in the Al counts is denoted by Z, which corresponds to the location Z in Figure 4-5 [207]

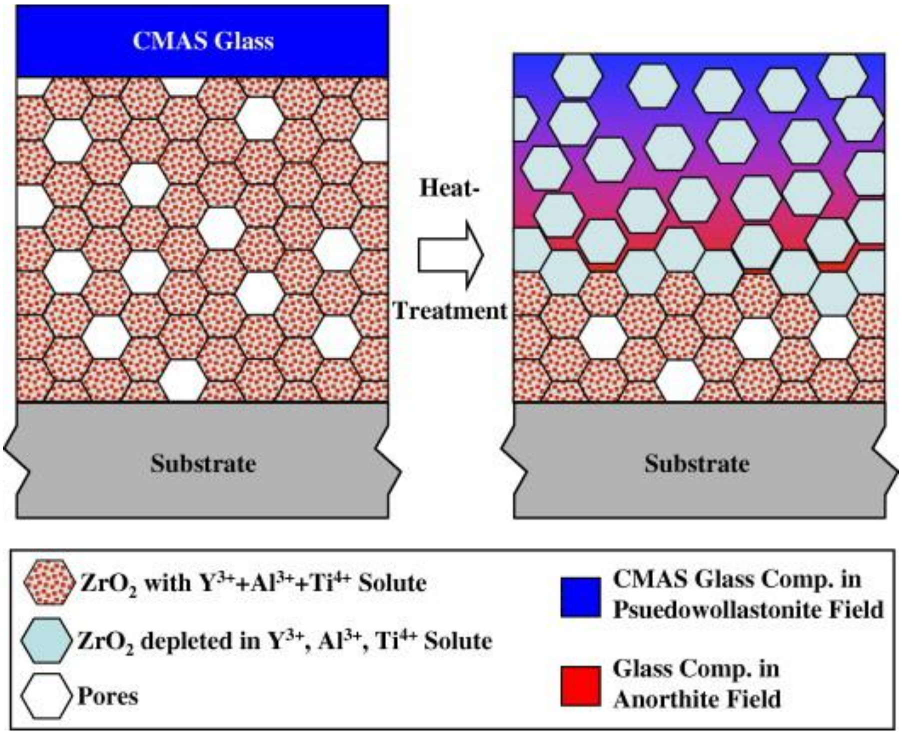

Figure 4-7 Schematic illustration (not to scale) of the proposed mechanism of CMAS-attack mitigation in SPPS (YSZ+Al+Ti) TBCs [207]

More recently, Kramer et al. [253] showed that a layer of gadolinium zirconate ($Gd_2Zr_2O_7$) is effective in arresting the infiltration of CMAS. The high temperature reaction between the CMAS glass and the gadolinium zirconate produces a dense crystalline layer, which consists of an apatite phase, $Gd_8Ca_2(SiO_4)_6O_2$ and cubic ZrO_2 with Gd and Ca in solid solution. The possibilities of implementing gadolinium zirconate as a TBC have since then been explored by several other researchers [230, 243, 254]. Gledhill et al. [230] showed that gadolinium zirconate is indeed resistant to attack by molten lignite fly ash, and the proposed mitigation mechanism is illustrated in Figure 4-8.

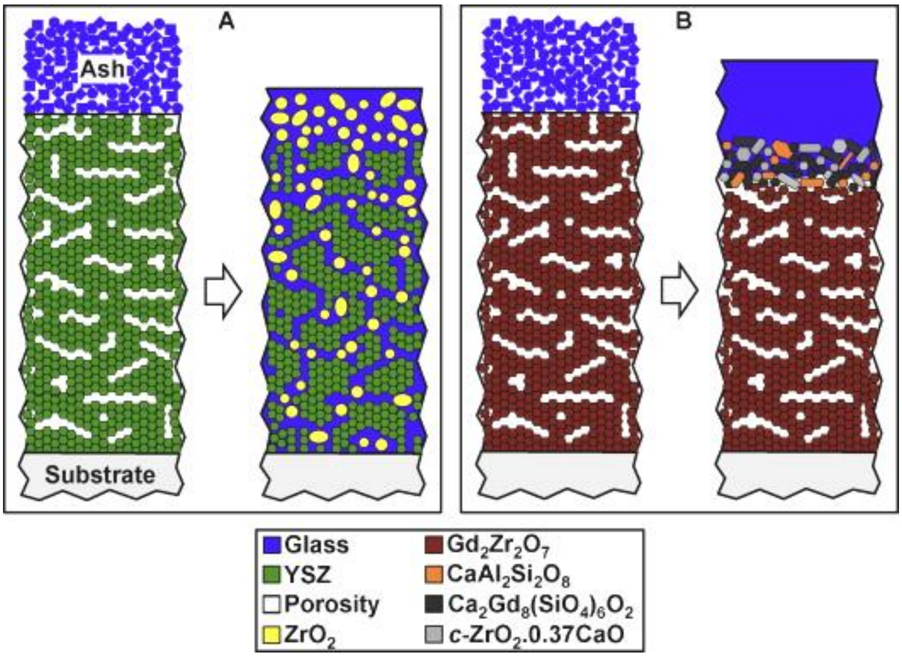

Figure 4-8 Schematic diagrams of APS TBCs cross-sections with lignite fly ash deposits, before and after 24 h heat treatment at 1200°C, depicting the possible interactions: (A) 7YSZ and (B) $Gd_2Zr_2O_7$ *[230].*

Zirconates with pychlore structures, like gadolinium zirconate, are attractive because they offer lower intrinsic thermal conductivity. They do however, have slightly higher thermal expansion coefficients (and lower fracture toughness) relative to the 7YSZ of around 9 – $10 \times 10^{-6}\ K^{-1}$, which explains why by itself as a top coat, it exhibits a much lower spallation lifetime compared to conventional 7YSZ. In addition, gadolinium zirconate is not chemically compatible with the TGO. In order to tackle these issues, graded TBC structures with a 7YSZ interlayer have been tested and shown to have a slightly longer lifetime than having a single layer YSZ top coat [254]. It must be noted, however, that due to the expansion mismatch, large segmentation cracks often form during thermal cycling, which negates the advantage of having a lower intrinsic thermal conductivity and CMAS resistant composition, since both hot gases and contaminants are likely enter such deep crevasses. Unfortunately, there are no obvious solutions to toughening zirconates and this challenge remains to be addressed.

5.0 Experimental Procedures

This chapter describes the experimental methods employed in this work, divided into three parts. The first part describes the methodology for prediction of sintering-induced TBC spallation lifetime. The second part describes procedures on how the first study was extended to investigate the effect of different levels of CMAS deposits on the TBC spallation behaviour. In the final section, details are found on how the Pegasus HP gas turbine engine was used in order to study the effects of particle size and temperature on the deposition characteristics of ingested volcanic ash on internal turbine surfaces.

5.1 Methodology for the Prediction of Sintering-Induced Spallation Lifetime of PS TBCs

5.1.1 Choice of TBC Substrate

In order to study the spallation behaviour of TBCs, with particular focus on sintering, specimens were prepared by depositing onto alumina substrates. The rationale for the use of this unconventional substrate is as follows. The use of dense polycrystalline alumina ensured that there was little or no degradation of neither the substrate nor the interface during isothermal heat treatments, even at temperatures as high as 1500°C. It should be noted that the misfit strain ($\Delta\alpha\Delta T$) in this system has the opposite sign to that in a more conventional (zirconia/superalloy) coating/substrate combination, since alumina has a lower thermal expansivity than zirconia. The stress induced in the coating is therefore tensile upon cooling (from a stress-free upper temperature), whereas it is compressive if it were on a superalloy substrate. However, since only the square of this strain appears in Equation 2-6, the driving force for interfacial debonding (the interfacial strain energy release rate) is unaffected by its sign. As it can be seen from the literature data [10, 255, 256] in Table 5-1, the misfit strain induced, for a given temperature drop, is of similar magnitude for zirconia/superalloy and zirconia/alumina coating/substrate systems.

Material	Thermal expansivity α (K^{-1})	Misfit strain from ΔT of 1000 K $\Delta\alpha\Delta T$ (millistrain)
Alumina	~ 7 – 8 × 10^{-6}	~ 3.5
YSZ	~ 11 × 10^{-6}	
Superalloy	~ 14 – 16 × 10^{-6}	~ - 4

Table 5-1 Approximate values [10, 255, 256] for the expansivities of alumina, YSZ and a typical Ni-based superalloy, and corresponding misfit strains for YSZ coatings on alumina and superalloy substrates, arising from a temperature drop of 1000 K

5.1.2 Alumina Substrate Laser Treatment

In order to ensure good adhesion of the plasma sprayed YSZ coating, the surface of the alumina substrate was roughened using a scanning laser beam. An SPI® 200W water-cooled fibre laser was used. The processing parameters are summarized in Table 5-2. The resultant topography of the alumina substrate is illustrated in Figure 5-1, which presents surface height maps (obtained using a WYKO RST Plus Optical Interferometer) before and after the laser treatment. Figure 5-2 shows an SEM image showing the relation between topographic features created on the alumina substrate surface and the laser tracks. The surface roughness (R_a), measured using a Veeco Dektak 6M Stylus Profiler over a length of 5 mm, was observed to increase from ~ 1.0 μm for the as-received substrates to ~ 9.5 μm after the laser treatment.

Power (W)	Frequency (kHz)	Feed rate (mm s^{-1})	Pulse length (μs)	Number of scans	Track spacing (μm)
30	75	550	1200	5	100

Table 5-2 Laser processing parameters for surface treatment of alumina substrates

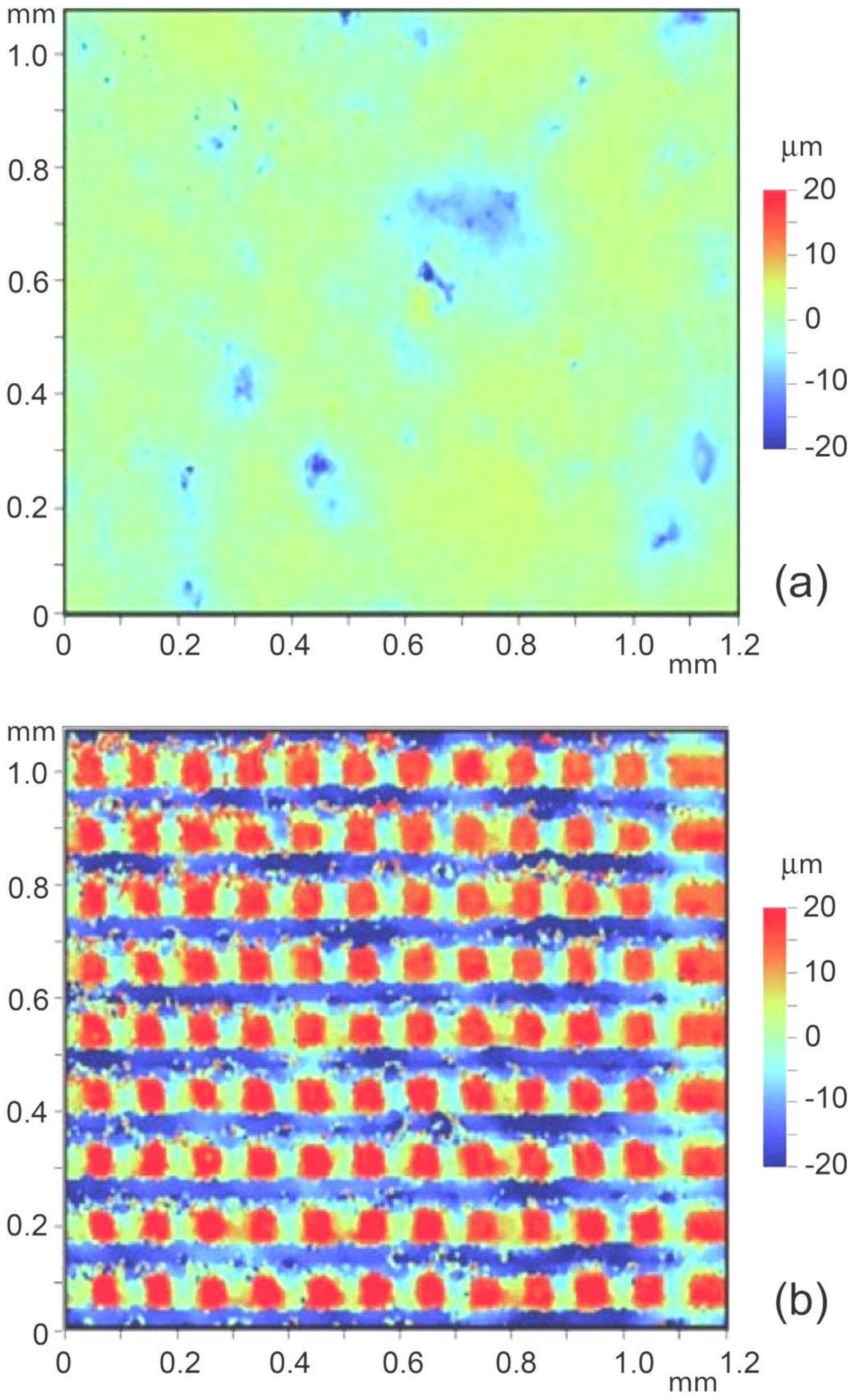

Figure 5-1 Illustration of the topography of alumina substrates, in the form of optical interferometric surface height maps (a) before and (b) after laser treatment.

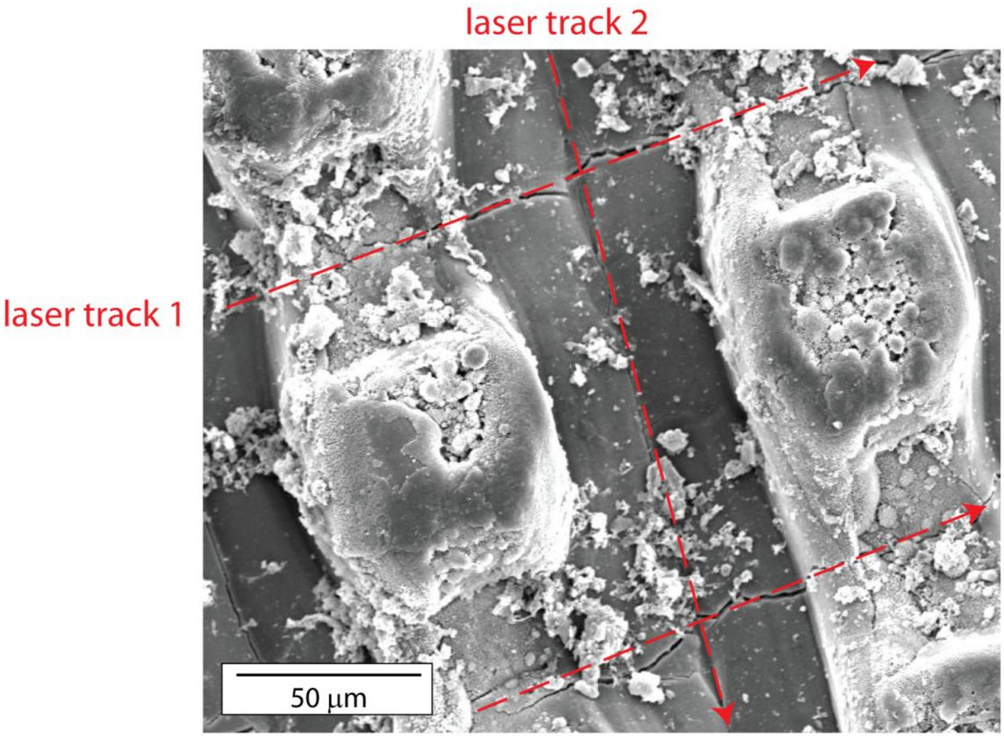

Figure 5-2 SEM image showing the relation between topographic features created on the alumina substrate surface and laser tracks.

5.1.3 Plasma-Spraying

The YSZ coatings were produced by plasma spraying of a Metco 204NS powder, with the composition given in Table 5-3, using a LPPS system with an F4-VB gun, at the University of Cambridge. The optimized spray parameters are summarized in Table 5-4. It is in fact most common for PS YSZ coatings to be produced in ambient air - i.e. using APS - but it was found to be necessary to use LPPS in order to ensure that the interfacial adhesion between the alumina substrate and the YSZ coating was adequate. The alumina substrates were 5 mm thick, with in-plane dimensions of approximately 50 mm by 50 mm. The temperature of the reverse side of the substrates was monitored during spraying, using a thermocouple spot welded onto a metallic plate, which was cemented onto the back of the substrate. This temperature typically reached a maximum of about 600°C by the end of the preheat passes. After spraying, specimens were cut using a diamond wheel, with a slow feed rate, giving specimens with dimensions of ~ 13 × 10 × 5 mm. A photograph of a TBC specimen prepared for spallation testing is shown in Figure 5-3.

Composition (wt.%)								
ZrO_2	Y_2O_3	HfO_2	Al_2O_3	SiO_2	TiO_2	CaO	MgO	Fe_2O_3
bal.	7.6	1.5	<0.01	0.07	0.09	<0.01	<0.01	<0.01

Table 5-3 Chemical composition of Metco 204NS starting powder

Chamber pressure (mbar of Ar)	200
Plasma gun	F4 Plasma Technik VPS
Nozzle diameter (mm)	8
Plasma gas flow rates (l min^{-1})	Ar 50, H_2 7
Carrier gas flow rates (l min^{-1})	Ar 3.5
Arc current (A)	760
Voltage (V)	50
Power (kW)	38
Preheat stand-off distance (mm)	400 (4 passes) 270 (2 passes)
Spraying stand-off distance (mm)	270

Table 5-4 Plasma spraying parameters for TBC specimens on alumina substrates

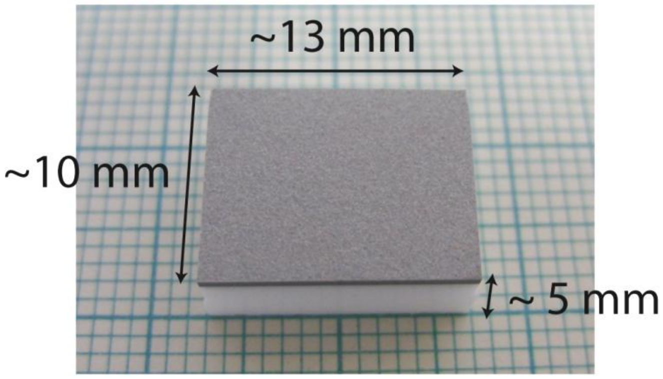

Figure 5-3 TBC specimen sprayed onto alumina substrate, cut into appropriate dimensions for spallation testing

5.1.4 Heat Treatment with Periodic Quenching for Spallation Monitoring

A computer-controlled furnace with a periodic quenching capability (see schematic in Figure 5-4) was used to investigate coating spallation. The set-up comprises a tube furnace (Elite Thermal Systems, model TSH16), with a recrystallized alumina tube of diameter 50 mm. A motorized mechanism periodically pushes the sample boat in and out of the furnace. Each boat typically contained about 6 samples. When withdrawn, the samples were quenched with nitrogen gas jets. An R-type thermocouple was located inside the sample boat, to monitor their temperature. A typical specimen thermal history is shown in Figure 5-5, where it can be seen that the furnace temperature in this case was set at 1500°C and quenching (to approximately 100°C) took place at hourly intervals, induced by 5 minutes of exposure to the nitrogen jets. The system incorporates a motion sensitive webcam focussed on the sample boat, the output of which is recorded during quenching. Inspection of recorded images and videos allowed the time of spallation to be established for individual specimens, without the need for frequent personal inspection. In this way, it is possible to efficiently obtain data relating to substantial numbers of specimens, exhibiting fairly long spallation lifetimes.

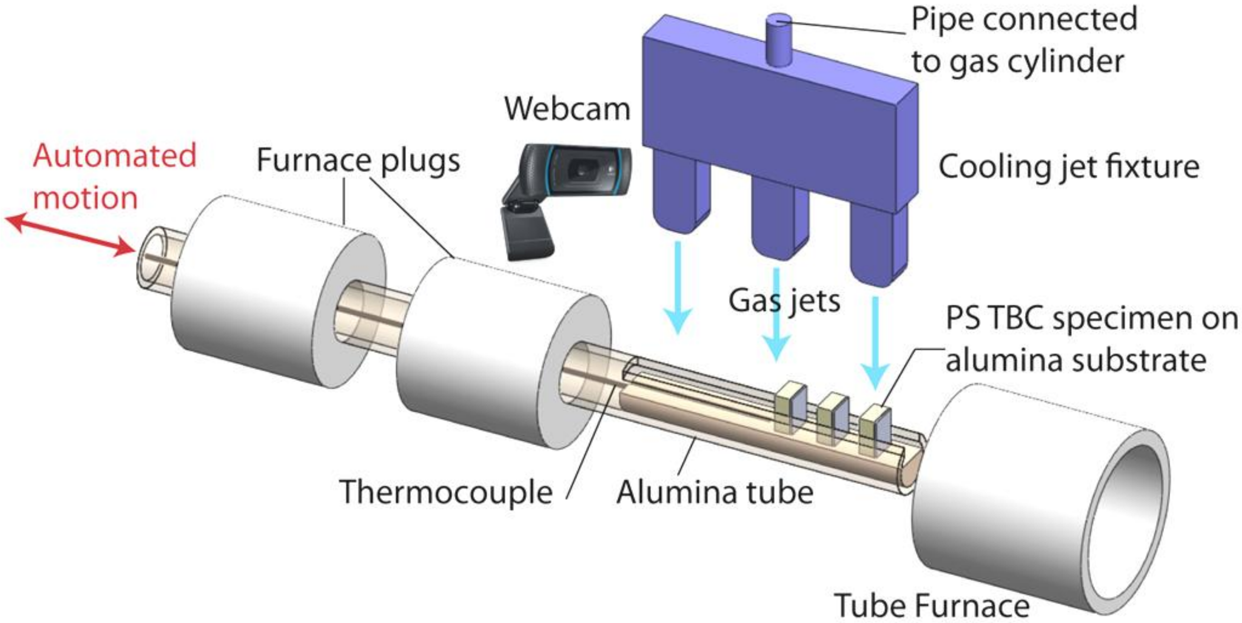

Figure 5-4 Schematic illustration of periodic quenching and spallation monitoring set up.

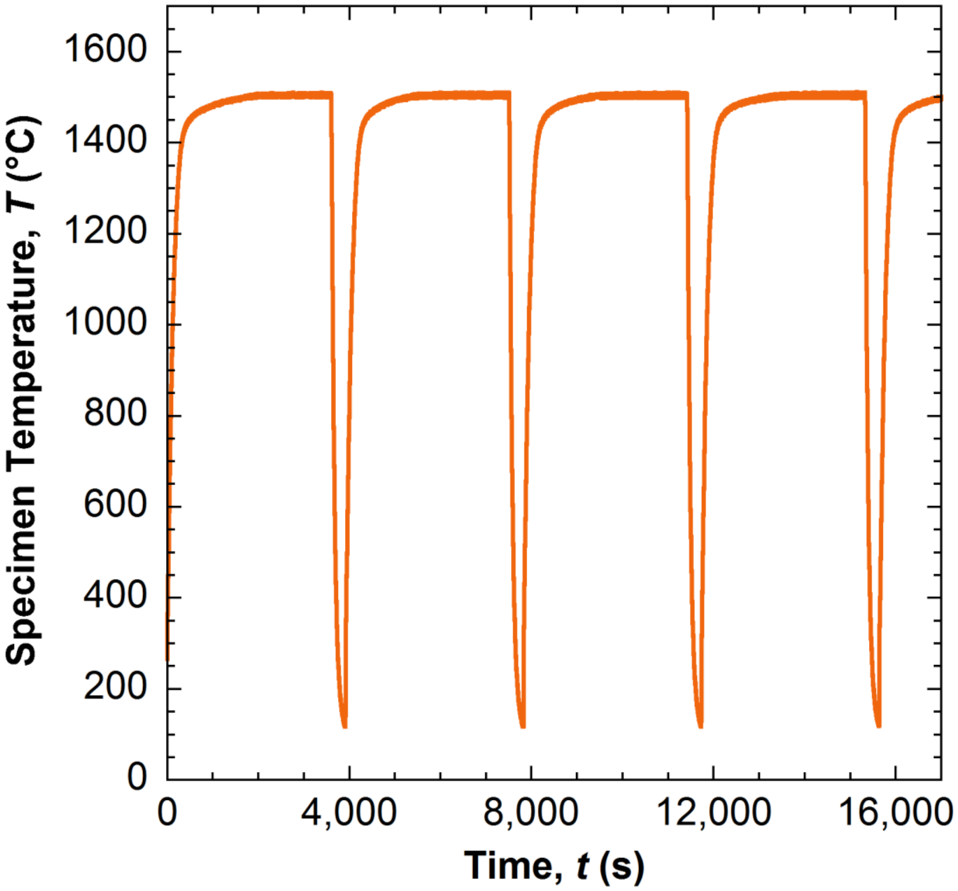

Figure 5-5 Measured thermal history of thermocouple placed inside the sample holder of the periodic quenching set up. Furnace temperature was set at 1500°C with hourly 5 mins quenching.

5.1.5 Preparation and Heat Treatment of Free-Standing Coatings

Free-standing YSZ TBC specimens were obtained by spraying (using the parameters shown in Table 5-4) onto grit-blasted mild steel substrates. Detachment from the substrates was achieved by immersion in 36% HCl, which caused partial dissolution of the steel. These specimens were used to determine the coating expansivity and its stiffness, as a function of heat treatment time and temperature. Heat treatments were conducted in the periodic quenching furnace, as described in section 5.1.4. Two specimen arrangements were employed, the YSZ samples being placed on (2 mm thick) alumina plates either with or without a second (2 mm thick) alumina plate placed on top of them. This was done in view of observations that, particularly at extended exposure to very high temperatures (~ 1500°C), there was a tendency in the absence of the second alumina plate for the coatings to distort by developing some curvature. Such distortion, especially if curvature were to develop in the transverse direction across the width of the specimen, meant that stiffness measurements obtained by bending tests (described in section 5.1.7) were significantly over-estimated.

5.1.6 Coating and Substrate Expansivity Measurement

Expansivity data for the YSZ coatings (and also for the dense alumina substrates) were obtained using a Netzsch 402C dilatometer. The set up comprises an alumina sample holder with an alumina push rod, which applies a constant load to the specimen (of 0.3 N). A linear variable displacement transducer (LVDT) measures the displacement of the push rod. Samples were heated and cooled between 20°C and 1200°C at 10°C min^{-1}. A calibration run was conducted in order to correct for dimensional change of the alumina push rod. Tests were performed on free standing coatings in the in-plane direction, and specimens approximately 10 mm in length were used.

5.1.7 Coating Stiffness Measurement

In-plane Young's modulus values of free-standing coatings were obtained via four point bending, using a scanning laser extensometer (Lasermike model 501-195, with a resolution of around 3 μm) to monitor specimen deflections. Specimen dimensions were approximately 12 × 40 × 0.4 mm. All measurements were made at room temperature. Loads were applied via a counter-balanced platen, using small pre-weighed masses. The four point bending technique was deemed most suitable in the order to determine the global stiffness values of fragile, detached coatings as it involves the application of a uniform bending moment over a larger area of the coating. It may be noted that values obtained in bending are weighted equally by tensile and compressive responses. In fact, these are expected [165] to be similar for strains up to about 0.7%, after which the compressive value is likely to be significantly higher as a consequence of the closure of through-thickness microcracks. The strains induced during stiffness measurement in this work ranged up to about 0.1%. The following equation, derived from elastic beam theory, was used to calculate the coating stiffness:

$$E = \frac{Fa}{48I\delta}(3L^2 - 4a^2) \qquad \text{Equation 5-1}$$

Where F is load, a is the distance between the outer and inner supports, L is the distance between the outer supports, δ is the central deflection and I (=bh^3/12) is the second moment of area, where b is the coating width and h is the thickness.

5.1.8 Microstructural Examination

Coating microstructures were examined using a JEOL-5800 SEM, with a typical accelerating voltage of 10 – 15 kV. Samples were sputter coated with gold (using an Emitech 330 facility), to prevent charging.

5.2 Methodology for Investigating the Effect of CMAS on TBC Spallation Lifetime

5.2.1 Chemical Composition of VM/VA Powder

Vermiculite (VM) is a hydrous silicate mineral and is widely mined for commercial uses such as for insulation panels or fertilizers. The vermiculite (VM) powder was supplied by Goodfellows and the volcanic ash (VA) powder was supplied by Dr. Margaret Hartley of the Earth Sciences Department in Cambridge University. VA powder was extracted from the ground near the Laki volcanic vent in Southern Iceland. In both cases, the powder was ground/ball milled and then sieved to give a selected size range. The chemical compositions of the two powders, obtained by EDX, are shown in Table 5-5. They have broadly similar compositions, although the VM is richer in Mg, Si and K with virtually no Ca content, while the VA contains appreciably higher levels of Fe.

Element	Weight (%)	
	Vermiculite	Volcanic Ash
O	Bal.	Bal.
Na	2.5	1.0
Mg	11.6	2.0
Al	4.0	6.7
Si	28.8	24.0
K	4.8	0.1
Ca	-	6.1
Ti	0.6	2.4
Fe	4.0	21.3

Table 5-5 Chemical composition (wt.%) of as-received VM and VA powders, data obtained by EDX.

5.2.2 Particle Size Distribution

Particle size distributions were obtained using a Malvern P580 Mastersizer E, which involves adding the powders to an aqueous medium and keeping them in suspension using a stirrer. Plots are shown for both powders in Figure 5-6. Average particle sizes are about 50 µm and 100 µm respectively for VA and VM. Of course these size distributions are dependent on the sieving and grinding operations, and on mechanical characteristics of the powder particles, more than on their original sizes. Nevertheless, particle size distributions are relevant, for example, in determining whether ingested particles adhere to internal turbine surfaces following impact (further details of which are discussed in section 5.3 and Chapter 8.0).

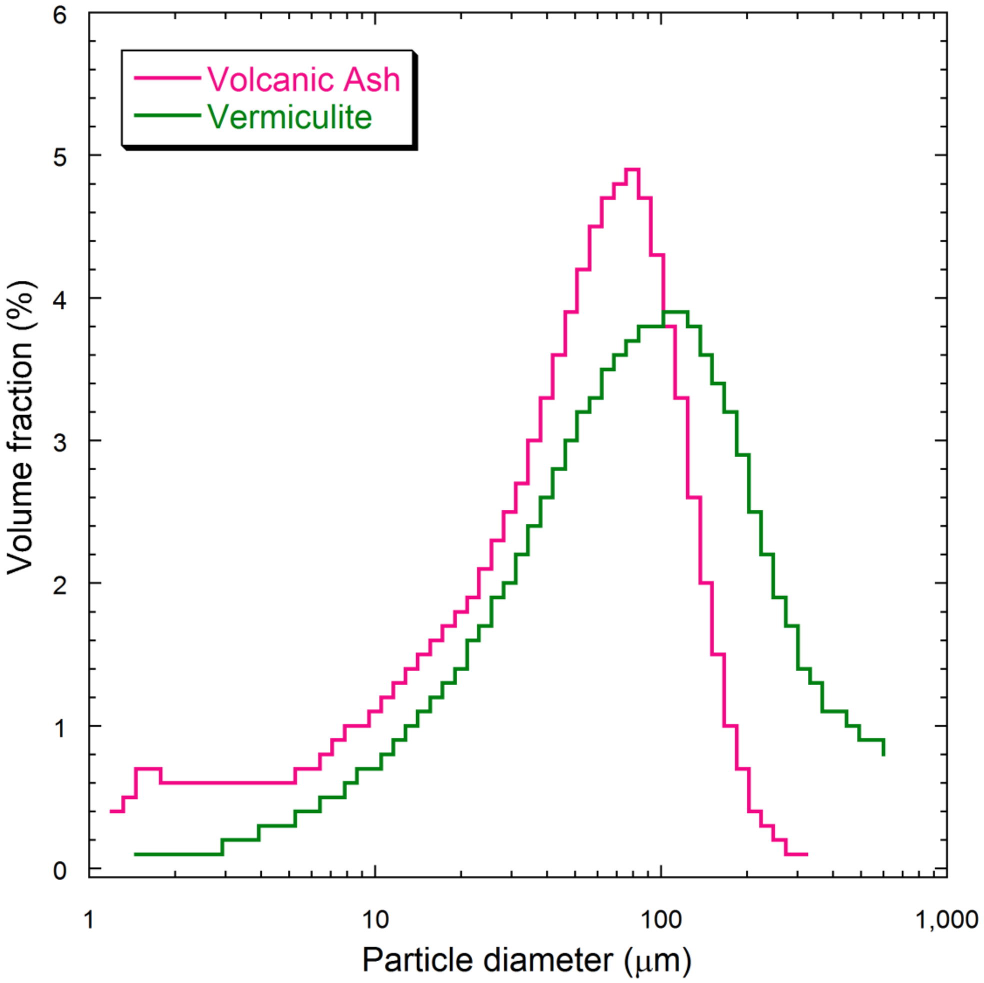

Figure 5-6 Particle size distributions for VM and VA powders after ball milling and sieving. Bin sizes as indicated.

5.2.3 Particle Morphology

SEM images showing particle morphology of ground/milled and sieved VM and VA powders are shown in Figure 5-7. Both VM and VA particulates exhibit angular and irregular morphologies, which are a result of the mechanical grinding operations.

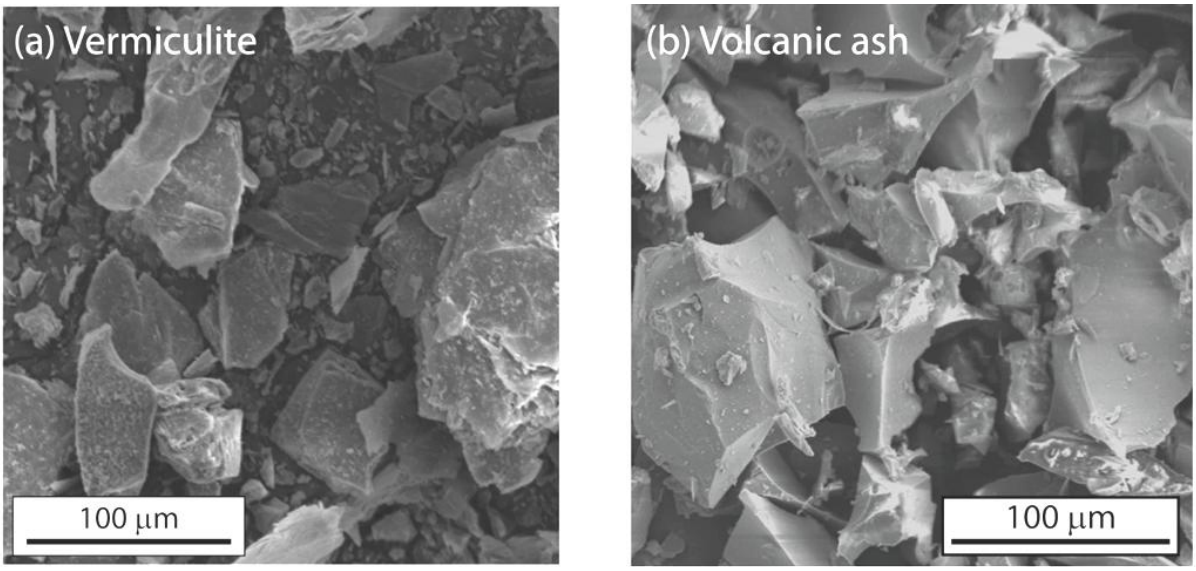

Figure 5-7 SEM showing particle morphologies of (a) VM and (b) VA powders after grinding/ ball milling and sieving.

5.2.4 Differential Scanning Calorimetry

Glass transition and melting temperatures were obtained using a Netszch 404 DSC, with a ramp rate of 10°C min^{-1}, up to 1500°C. The DSC plots for both types of powder are shown in Figure 5-8, where it can be seen that these temperatures are ~ 1040°C and 1360°C for the VM and ~ 500 – 700°C and 1130°C for the VA respectively. Although, it is hard to identify the exact position of the glass transition temperature, particularly in the case for the VA.

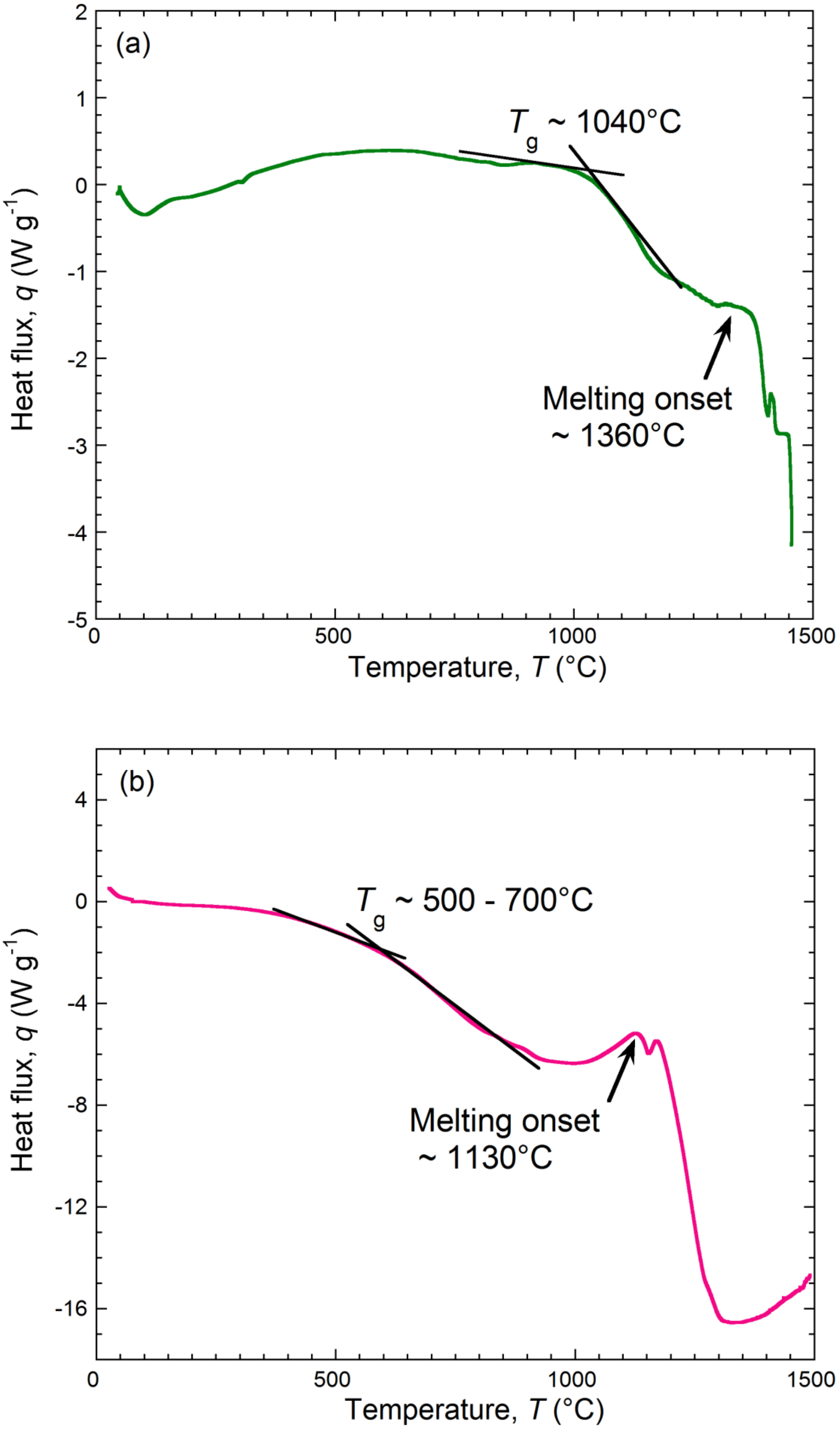

Figure 5-8 Differential scanning calorimetry plots, obtained using a heating rate of 10°C min^{-1}, for powders of (a) VM and (b) VA.

5.2.5 X-ray Diffraction

The phases present in both types of powders, and in coatings exposed to CMAS, were investigated via X-ray diffraction measurements made using a Philips PW1710 diffractometer, with CuK_α radiation (λ = 0.154 nm), 40 kV accelerating voltage and a 40 mA filament current. A step size of 0.02° was used with a 4 second dwell per step. The XRD profiles are shown in Figure 5-9, where it can be seen that the VM samples contain only the expected vermiculite phase, where it can be seen that four possible crystalline phases have been identified for the VA, mostly at relatively low levels. These correspond to albite (sodium aluminium silicate), enstatite (magnesium silicate), sanidine (potassium sodium aluminium silicate) and magnetite (iron oxide). Albite is a plagioclase feldspar mineral, common in granitic rocks. Enstatite is commonly found in igneous and metamorphic rocks. Sanidine is a potassium feldspar, usually found in volcanic rocks. Finally, magnetite is one of the most common naturally occurring iron oxides. Due to many of the strong peaks overlapping, it is difficult to say which crystalline phases are definitely present, although, these four were found to be the most likely candidates. In both cases, the prominent broad peak at around 20 – 30° (2θ) is a clear indication that a substantial proportion of amorphous phase exists. The amorphous and crystalline phase proportions were calculated after peak deconvolution and profile fitting performed using Phillips PROFIT software. The software can fit Lorenzian, Gaussian, pseudo-Voigt and Pearson-Seven profiles, all of which can be symmetrical or asymmetric. This procedure allows the determination of peak positions, peak areas and widths. The amorphous proportions of the VM and VA samples were determined to be roughly 40 – 50% and 80 – 90% respectively.

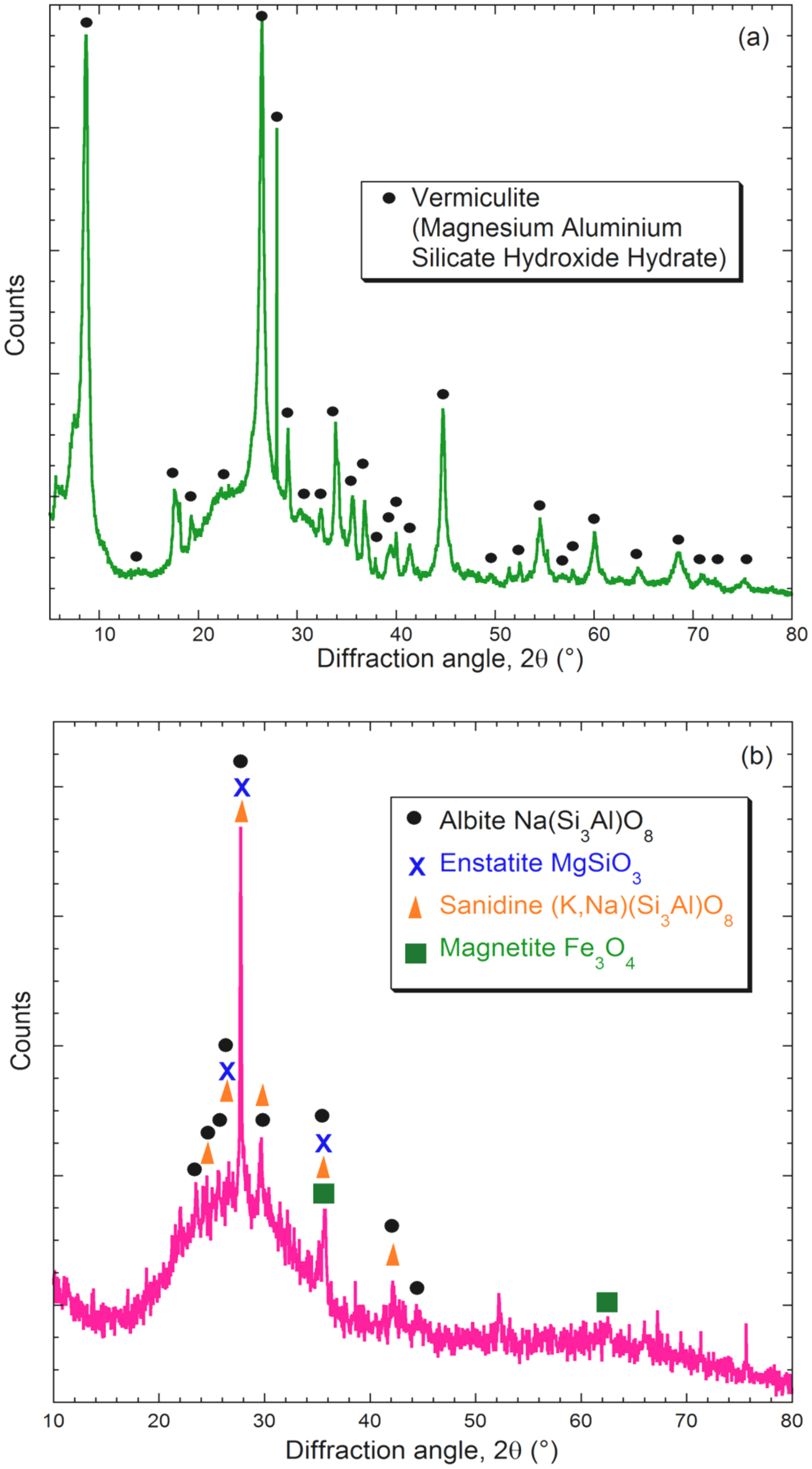

Figure 5-9 X-ray diffraction profiles from powders of (a) VM and (b) VA.

5.2.6 Application of VM/VA Powder and Microstructural Examination

VM and VA powders were applied onto the surface of free-standing YSZ coatings and also on specimens attached to alumina substrates, using the following steps (see schematic in Figure 5-10). The amount of VM/VA powder added was measured as percentage weight, with respect to the coating mass (measured after the short initial heat treatment):

- Spray adhesive applied onto the surface of PS YSZ coatings
- VM/VA powder sprinkled on top
- Specimens were placed in a furnace held at either 1000°C (for VA) or 1200°C (for VM) for 10 minutes and were subsequently taken out and left to air cool. This step ensured that no powder was lost during subsequent handling of the specimen.

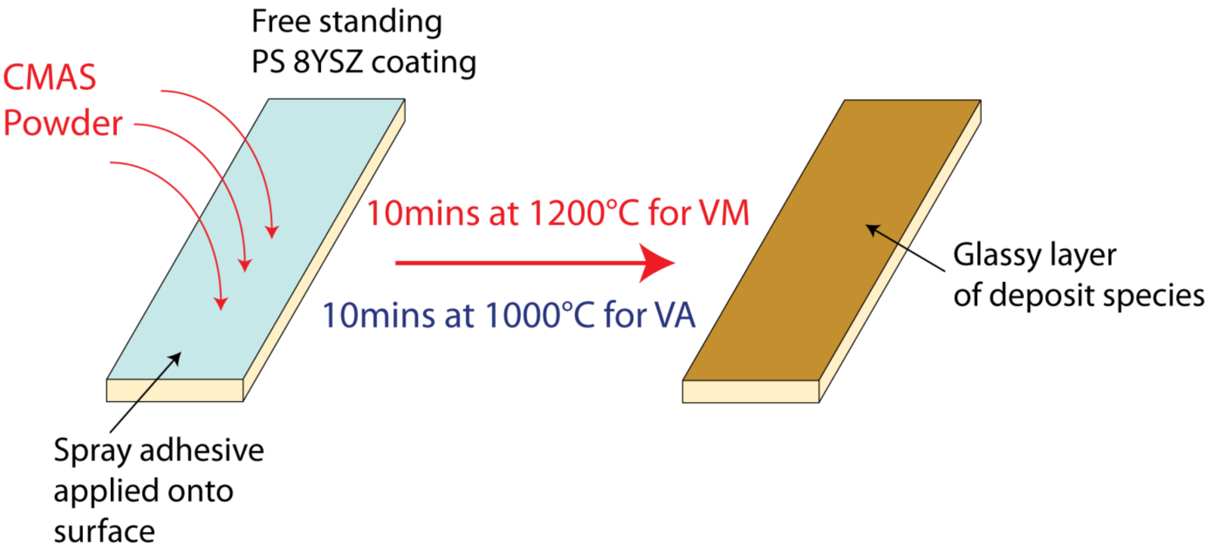

Figure 5-10 Schematic showing procedure for application of VM and VA powder onto TBC specimens

Experiments were carried out where such CMAS-incorporated free-standing coatings were subjected to various heat treatments, and small section of them were periodically cut off, polished, mounted and examined. SEM micrographs were taken of these sections, together with EDX mappings of elemental distribution, with around 30 minutes accumulation time. Particular attention was drawn to the distribution of Si, which is present at substantial levels in both VM and VA species, whilst it is virtually absent from the YSZ.

Figure 5-11 shows a BSE image of the transverse section of a free standing PS TBC, after 10 minutes of heat treatment at 1200°C with 1.8 wt.% of VM addition. Figure 5-12 shows a BSE image of the transverse section of a free standing PS TBC, after 10 minutes of heat treatment at 1000°C with 2.0 wt.% of VA addition. Corresponding EDX elemental maps are also shown. These images suggest that the initial treatment causes sufficient decrease in the viscosity of the CMAS, and therefore it readily spreads over the coating surface, is rapidly followed by its penetration into the (porosity within the) near-surface region of the coating.

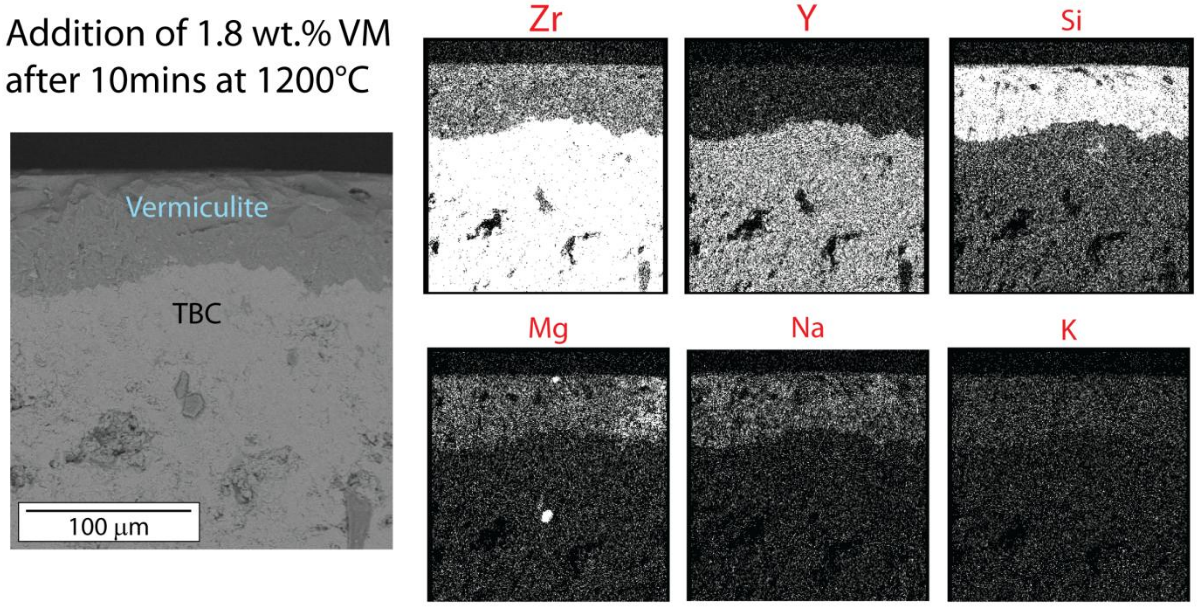

Figure 5-11 Showing BSE image of the transverse section of glassy VM layer on the surface of a free standing PS TBC, after 10 minutes of heat treatment at 1200°C, and corresponding EDX elemental maps

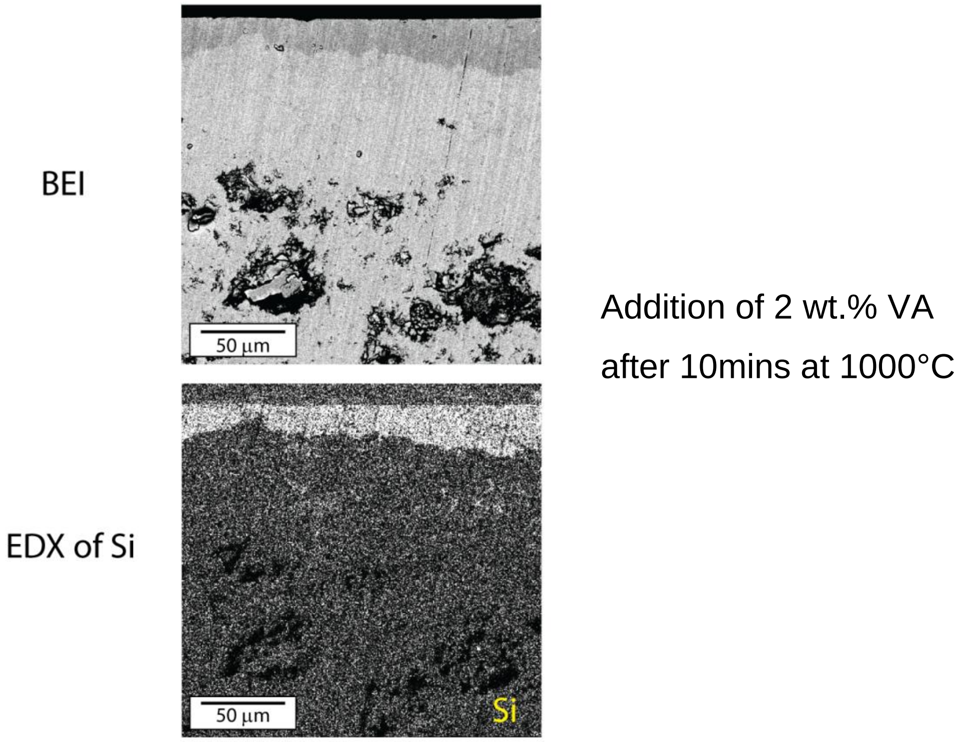

Figure 5-12 Showing BSE image of the transverse section of glassy VA layer on the surface of a free standing PS TBC, after 10 minutes of heat treatment at 1000°C, and corresponding EDX Si map.

5.2.7 Stiffness Measurement of Coatings with CMAS

Free-standing YSZ specimens were used to determine their stiffness as a function of heat treatment time, temperature and CMAS addition level. Heat treatments were conducted using a Lenton 1700 UAF 17/4 Furnace. Samples with CMAS incorporated on one side (in a similar fashion to as described in section 5.2.6) were placed on a clean, flat dense alumina surface and placed inside the furnace once the set temperature had been reached. After heat treatment, they were taken out and left to cool in air. The in-plane Young's modulus values were obtained via four point bending, as outlined in section 5.1.7. However, in order to account for the inevitable inhomogeneity in the microstructure (as CMAS was applied only on one side), stiffness measurements were made by taking an average of the Young's modulus value measured with the specimen orientated with the CMAS layer on top and on the bottom.

5.2.8 Coating In-Plane Shrinkage with Sintering

In-plane shrinkage of the YSZ coatings (with and without CMAS incorporation) was monitored using a Netzsch 402C dilatometer. Samples, of dimensions ~ 5 × 10 × 0.5 mm, were subject to isothermal heating at 1400°C and 1500°C for 20 hours. A calibration run was conducted in order to correct for dimensional change of the alumina push rod.

5.3 Methodology for Investigating the Deposition Behaviour of VA Particulates Inside a Small Gas Turbine Engine

5.3.1 VA Powder Characterisation

The same VA powder, as described in earlier sections, was employed for these experiments. Thus details of the starting bulk chemical composition, phase constitution, particle morphology and DSC properties of this VA may all be found in section 5.2. The specific heat capacity for this VA specimen was measured to be approximately 800 J kg^{-1} K^{-1}. The heat capacity calibration constant, required in order to determine the absolute heat flow, was measured using a sapphire standard.

Four different particle size distributions were used in the experiments, and these were obtained using a Malvern P580 Mastersizer E. The four different sieved fractions are shown in Figure 5-13, for fractions designated as “fine”, “medium 1”, “medium 2” and “coarse”. The average diameters in these cases were approximately 20 μm, 50 μm, 75 μm and 100 μm respectively. These nominal particle sizes were selected since it has been reported [224, 257] that the maximum size of particles ingested into a jet engine is typically about 100 μm.

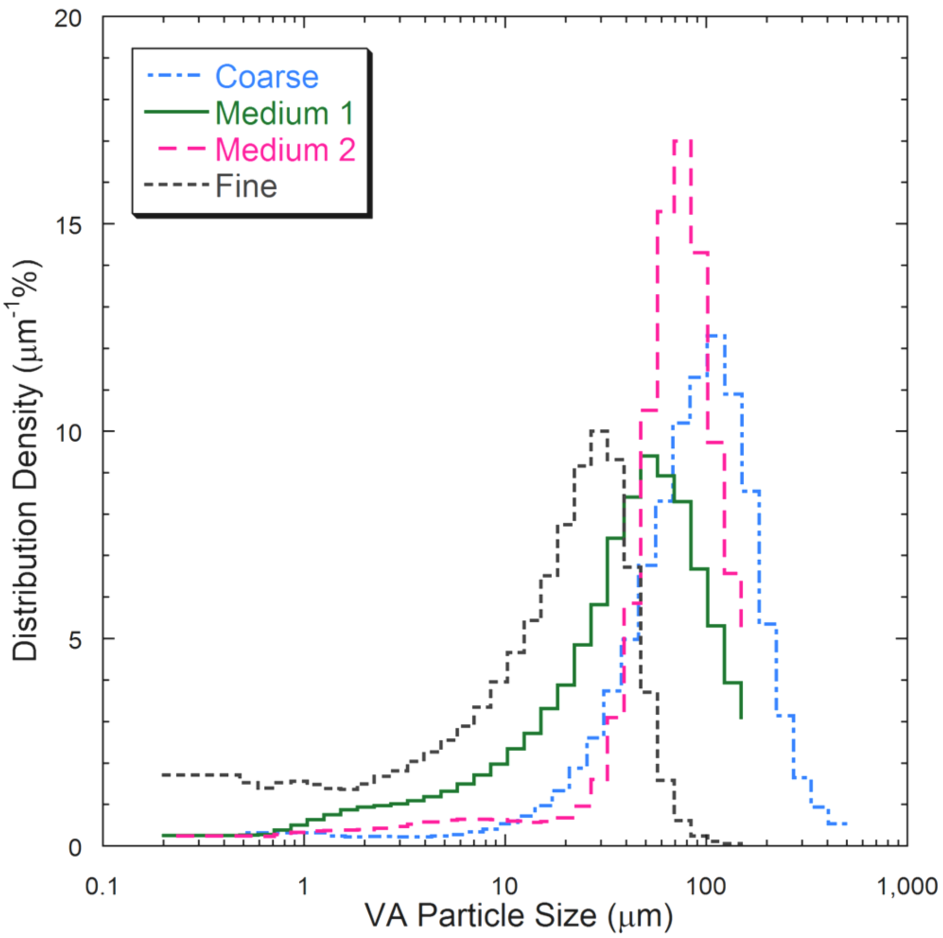

Figure 5-13 Particle size distributions of sieved VA powders (fine, medium 1, medium 2 and coarse), with the bin ranges indicated by the widths of the histogram columns.

5.3.2 Pegasus HP Gas Turbine Engine Technical Specification

The jet engine employed in this work was a Pegasus HP E-Start engine, manufactured by AMT Netherlands. It is a turbojet engine, with no by-pass air flow. The main technical specifications and operational parameters are shown in Table 5-6. The data presented refer to runs carried out with throttle settings at 100% and 50%, corresponding to engine speeds of approximately 120,000 RPM and 62,000 RPM respectively. All engine tests were carried out at the engine testing facility at AMT Netherlands (Geldrop), with the technical assistance of Bennie van de Goor, which is gratefully acknowledged.

Parameter	Engine speed (RPM)	
	120,000	62,000
Engine Diameter (mm)	120	
Engine Length (mm)	342	
Combustion Chamber Length (mm)	100	
Engine Weight (kg)	2.225	
Fuel Type	Kerosene	
Measured Average Thrust (N)	141	22
Pressure Ratio	3.2:1	2.9:1
Air mass flow rate (kg s^{-1})	0.375	0.185
Fuel consumption (kg s^{-1})	0.0081	0.0025
Exhaust gas temperature (˚C)	600	480

Table 5-6 Operational parameters for the jet engine

The complete experimental set-up is shown in Figure 5-14(a), with the engine mounted horizontally, the intake facing the camera and the exhaust pointing towards the extraction unit in the wall. The powder feeding system comprised a Dreschel bottle, containing the VA powder, with the inlet connected to a compressed air line and the outlet secured on a clamp, so that the ash was fed more or less axially into the intake. Compressed air entered the Dreschel bottle via the inlet, which then swirled the VA around, eventually pushing the particles out through the outlet. The feed rate was controlled by adjusting the pressure of the compressed air line.

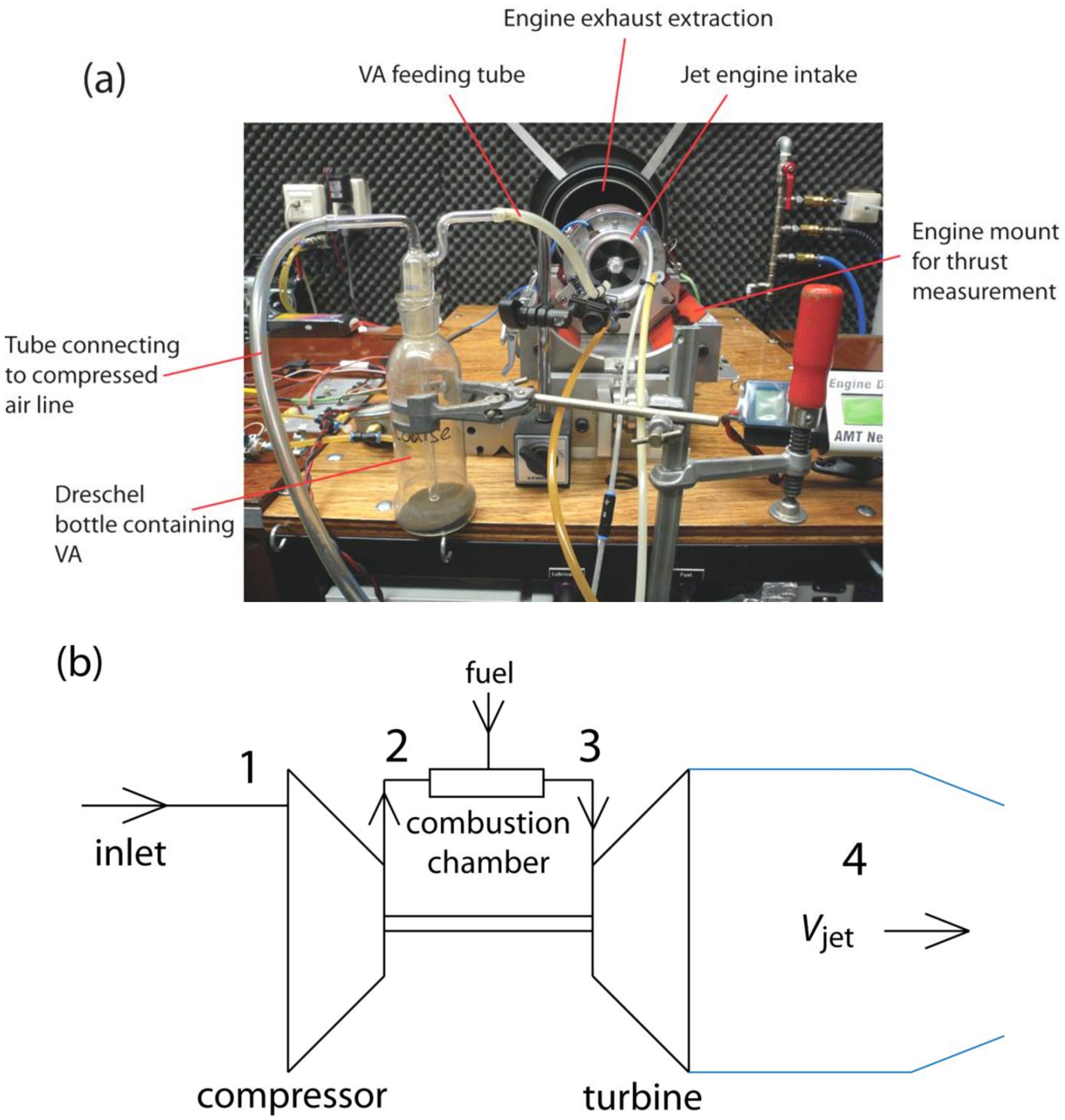

Figure 5-14 (a) Photograph of the experimental set-up and (b) schematic illustration of an ideal, simple gas turbine engine

5.3.3 Borescope for Engine Inspection

The interior of the engine concerned was examined after each run, using a 5.5 mm diameter rigid borescope with 90° direction and 55° field of view (Inspection Optics Ltd.). The endoscope had a focusing eye piece and was connected to a 24 W light source, and an SLR camera, in order to capture the images.

6.0 Prediction of Spallation Lifetime of PS TBCs based on Sintering-Induced Stiffening

In this chapter the effect of sintering-induced stiffening on the driving force for spallation of PS TBCs was investigated. Spallation lifetimes of TBC specimens sprayed onto alumina substrates were measured as a function of coating thickness. A simple fracture mechanics approach was employed in order to deduce a value for the strain energy release rate using measured coating expansion coefficients and stiffness values. The critical strain energy release rate was found to be approximately constant, and if this value had been known beforehand, then the rationale presented here could be used for prediction of coating lifetime. Although experiments presented here are based on the use of a ceramic substrate, the approach could be applied to conventional metallic substrate systems. The results presented in this chapter were published in [258].

6.1 Measurement of TBC Critical Strain Energy Release Rate

In order to experimentally evaluate the critical strain energy release rate for TBC spallation (driven by sintering-induced stiffening), the following global fracture mechanics approach was adopted. The expression for the interfacial strain energy release rate presented earlier (Equation 2-6) was set to equal the interfacial fracture energy. The strain in this case, justified by experimental procedures to follow, originates solely from differential thermal expansion between the coating and the substrate as they are rapidly cooled down (see Equation 2-2). The driving force for spallation is thus given by the expression:

$$G_{\mathrm{i}} = \frac{E_{\mathrm{TBC}} h (\Delta\alpha \Delta T)^2}{2(1-\nu)} \qquad \text{Equation 6-1}$$

Note that this equation assumes that spallation is not initiation-dominated and once the condition of $G_{\mathrm{i}} = G_{\mathrm{ic}}$ is satisfied, the propagation of an interfacial crack becomes energetically favourable. Once a spallation event was observed (after being subject to a well-defined thermal history, as described in section 5.1.4), the value of E_{TBC} at that point (measured by four point bending of free-standing specimen, as described in section 5.1.7) was inserted into Equation 6-1 to determine G_{ic}.

6.2 Thermal Expansion

Dilatometry data in the form of a plot of strain against temperature (during cooling) are shown in Figure 6-1 for the alumina substrate and for the free-standing YSZ coating. It can be seen that the expansivity of the YSZ is appreciably higher than that of the alumina at low temperatures ($\Delta\alpha$ ~ 2.7 × 10^{-6} K^{-1}), although the difference is less pronounced at high temperatures ($\Delta\alpha$ ~ 2.3 × 10^{-6} K^{-1}). The important parameter here is the magnitude of the misfit strain, $\Delta\alpha\Delta T$, where ΔT is the effective temperature change during quenching and $\Delta\alpha$ is the difference in expansivity between coating and substrate, which should be summed over this range. In the present work, ΔT was taken to be from 1100°C to 100°C, giving a misfit strain (obtained by integration of $\Delta\alpha$ over this range) of approximately 2.2 millistrains. The upper temperature was taken to be 1100°C, rather than 1500°C (used for heat treatments), in an attempt to take account of the substantial creep relaxation of stresses expected at temperatures above 1100°C. The TBC is likely to stress relax substantially and maintain a relatively stress-free state at temperatures over 1100°C, even with rapid cooling. This estimate is indeed a crude one, although it is broadly based on information of creep rates obtained both by experimentation [114, 259] and in the modelling work [128, 178, 179] reported in literature.

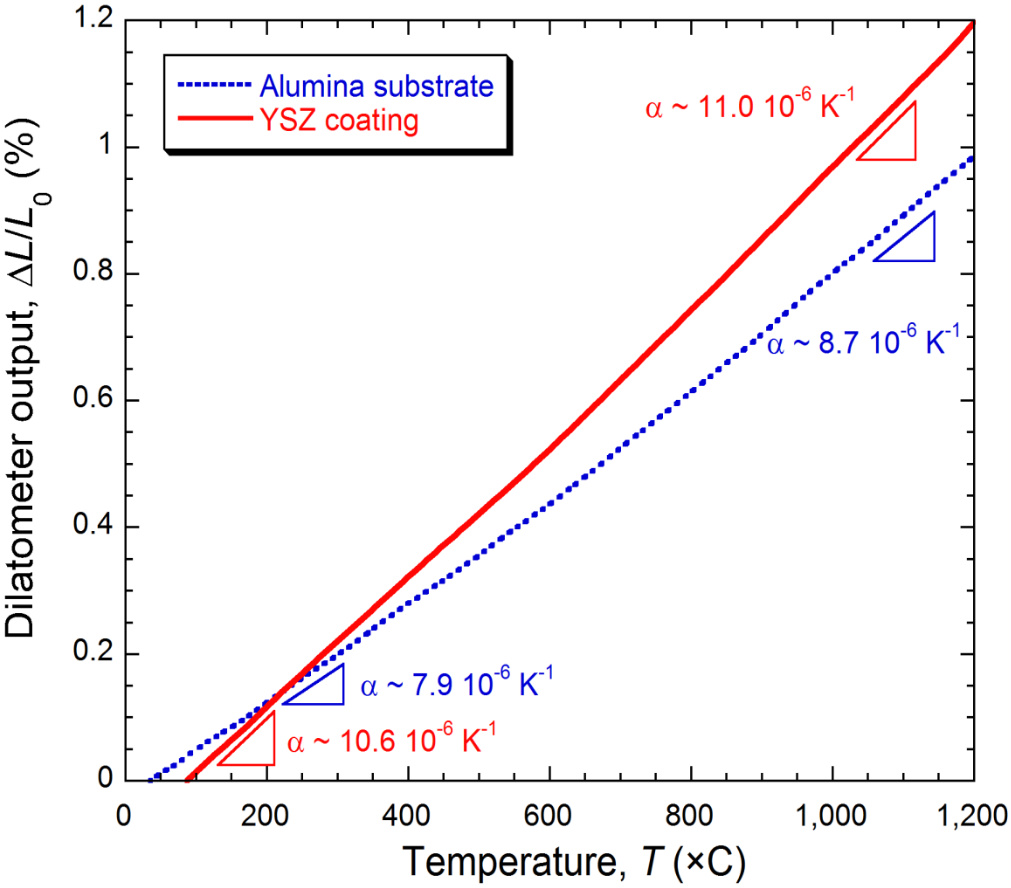

Figure 6-1 Dilatometry data, showing how the expansivities of the alumina substrate and the YSZ coatings vary with temperature

6.3 Sintering-Induced Stiffening

Figure 6-2 shows measured Young's modulus values for free-standing YSZ coatings, as a function of heat treatment time at 1400°C and 1500°C. These measurements were made with and without "weights" - i.e. an alumina plate on top of the specimen, which eliminated the development of curvature. The error bars represent standard deviations on sets of between 2 and 4 specimens in each case.

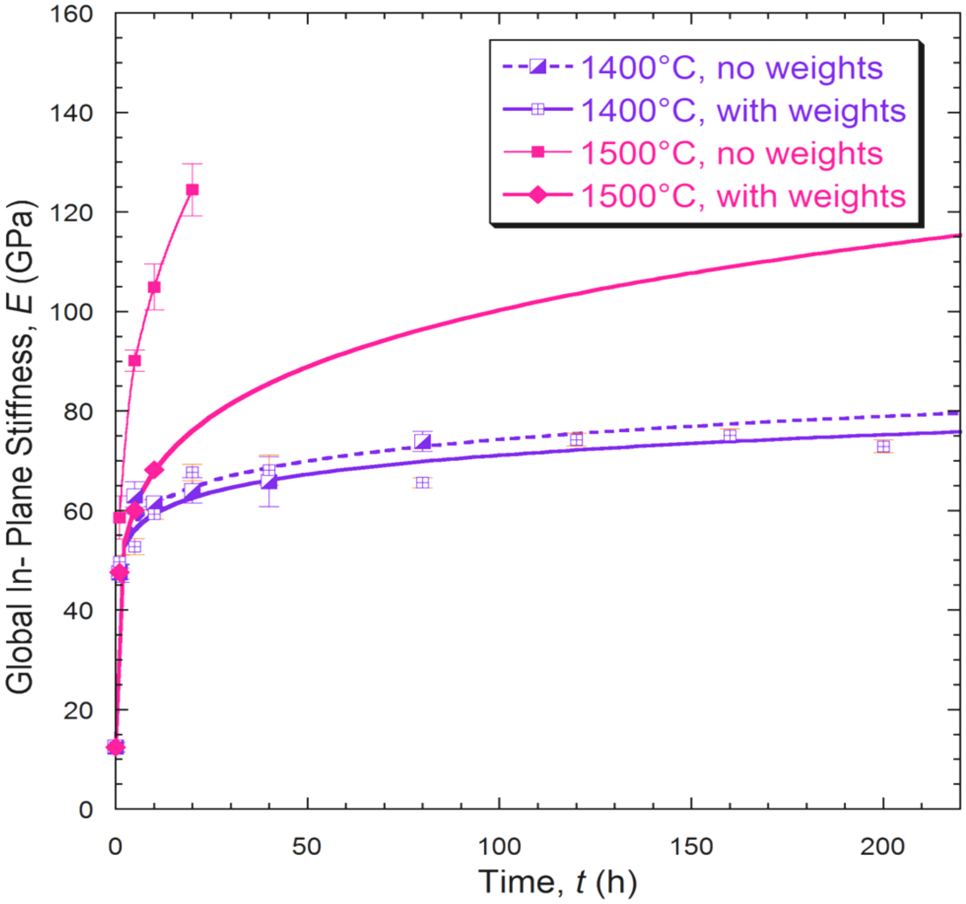

Figure 6-2 Measured stiffness data, obtained via four point bending, for YSZ coatings heat treated at 1400°C and 1500°C. The error bars represent standard deviations on sets of between 2 and 4 specimens in each case.

The mechanisms of sintering operative in plasma sprayed YSZ coatings are well documented [178, 179]. It can be seen in Figure 6-2 that the associated stiffening is rapid at these very high temperatures. It has been found that even at temperatures as low as 1100°C, the initial as-sprayed stiffness of around 10 – 15 GPa is observed to increase by a factor of two or three within a few tens of hours [114, 163, 171, 174, 175, 180]. It is also clear from Figure 6-2 that data obtained by bend testing can be significantly overestimated by curvature development, particularly at 1500°C. Even slight curvature in the transverse direction is known to raise the apparent beam stiffness substantially and in those specimens the curvature was apparent to the naked eye when laid on a flat surface. The origin of the curvature is unclear, but it is likely that it arises from differential shrinkages occurring during sintering and hence this would be a phenomenon associated with grain boundary diffusion, rather than surface diffusion [178]. It is probably caused by different degrees of constraint along the edges/outer surface of the samples compared with the bulk of the coating in the interior, although it is possible that effects such as through-thickness gradients in the microstructure (e.g. due to varying pore architecture) could be at least partly responsible [170]. It tends to be a problem only with relatively high sintering temperatures (i.e. > 1400°C), such as those employed here. The forces generated are low, so the effect can be eliminated by the small weights (2 mm thick alumina plates placed on top) used in the current work. From an alternative point of view, the coatings creep very readily at these temperatures, and so can easily be flattened. It was found that a problem does arise, however, when the specimen are overlaid with weights, in which case they tend to sinter onto the coatings after a while, even with the interruption of periodic quenching. The measurements with weights at 1500°C therefore extend only up to 10 h. Stiffness values for longer times were obtained from the extrapolated curve (“1500°C, with weights”) shown in Figure 6-2. The equation for this curve was found to be:

$$E = 12.5 + 34.9t^{0.20} \qquad \text{Equation 6-2}$$

where E is in GPa and t is in hours.

6.4 Sintering-Induced Changes in Microstructure

Figure 6-3 Shows SEM images of the fracture surface of PS TBCs in its (a) as-sprayed state (using spray parameters shown in Table 5-4) and (b) after 20 h of heat treatment at 1500°C. The usual PS structures are apparent in the first image, with columnar grains visible within overlapping splats. The structures are, however, slightly more fragmented and refined compared to standard APS microstructures as these specimens were prepared under LPPS conditions. In the second image, due to the prolonged high temperature treatment, the columnar grains are no longer distinguishable, primarily due to grain growth and also the removal of fine-scale intra-splat cracks and voids. The remaining larger voids have also taken a spherodized form, probably due to surface diffusion effects. These changes in the microstructure all point towards a consistent picture of a rapid decrease in surface area of the coatings, which results in an almost four-fold increase in the global in-plane stiffness (after approximately 20 h at 1500°C), as seen previously from the stiffness plots in Figure 6-2.

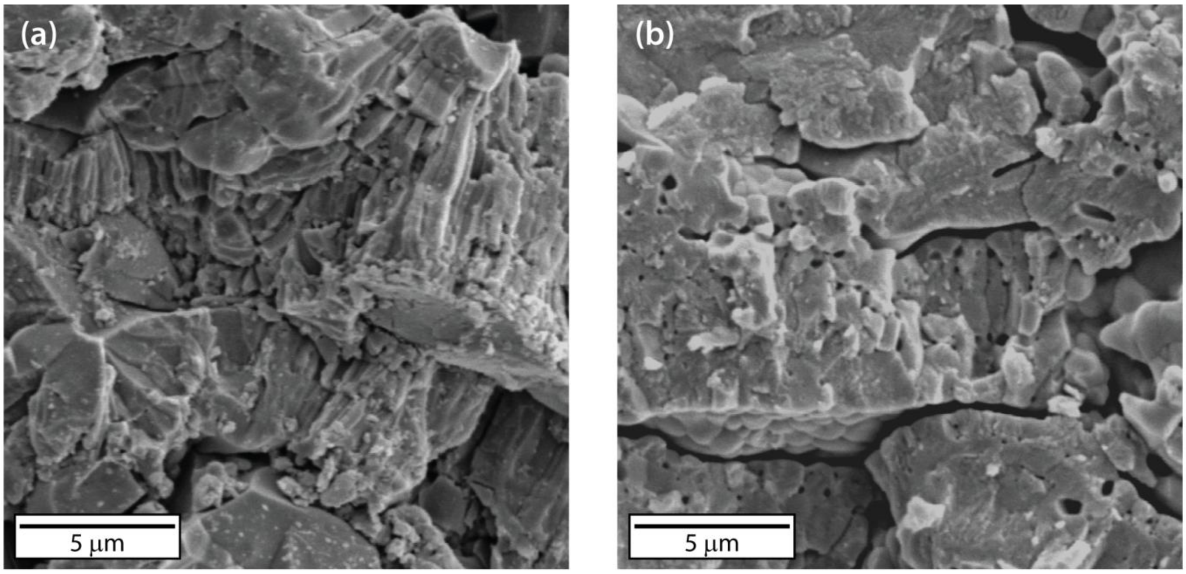

Figure 6-3 (a) Fracture surface of as-sprayed PS TBC (using spray parameters shown in Table 5-4) and (b) fracture surface of the same specimen after 20 h heat treatment at 1500°C.

6.5 Spallation Lifetimes

Spallation results obtained for 1500°C are summarized in Figure 6-4, which presents data from 18 specimens (of YSZ coatings on alumina substrates), with coating thicknesses varying in the range of 300 – 700 μm. The lifetimes, which discounts any time spent during the heating or cooling transients, range from about 40 h to over 150 h. It can be seen that, thicker coatings show a distinct tendency to spall more quickly, and the inverse relationship is seemingly linear. The strong correlation shows that coating failure is mainly driven by elastic stresses induced in the bulk of the coating. This effect of coating thickness is intuitive, as this is due to the greater stored elastic strain energy (see Equation 6-1) in the coating, per unit area of interface, and the theory is familiar for a wide range of coating systems. Nevertheless, these results do illustrate quite clearly that any lifing methodology focussed solely on the chemistry and topography of the interface, or near-interfacial regions is unlikely to be reliable.

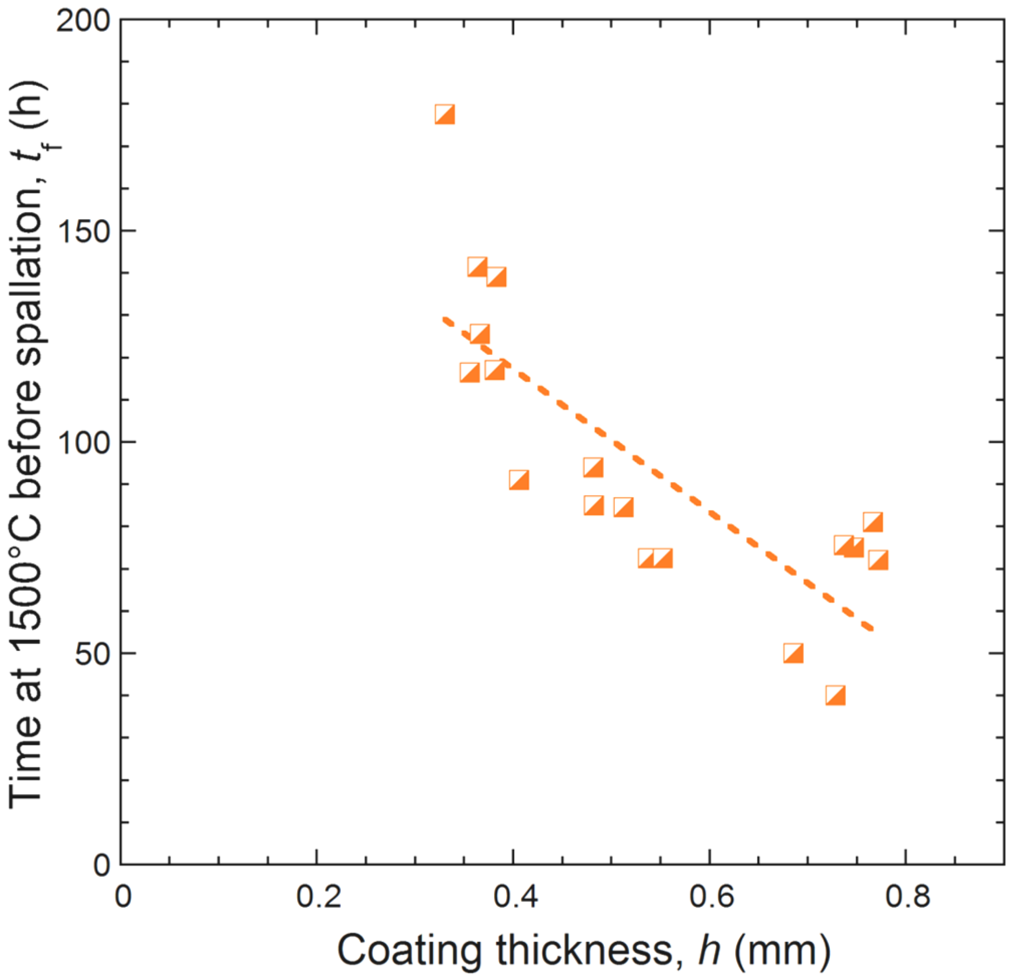

Figure 6-4 Experimentally observed spallation lifetimes at 1500°C for YSZ coatings on alumina substrates, plotted as a function of coating thickness. Each data point represents a single spallation event.

6.6 Edge Relaxation Effects and Segmentation Cracks

In principle, for each of the spallation lifetimes shown in Figure 6-4, it should be possible, using the corresponding coating stiffness value, E_{TBC}, to obtain a value for G_{ic} from Equation 6-1. However, there is a complication associated with the in-plane dimensions of the specimen. These specimens are quite small in the planar directions relative to the coating thickness. There is also a pronounced tendency for through-thickness ("segmentation") cracks to form within the coating when the system is subject to differential thermal contraction stresses - as indeed commonly observed to develop in YSZ coatings on gas turbine components in service. Such through-thickness cracks are presumably created by in-plane tensile stresses. With a conventional Ni alloy substrate, in-plane tensile stresses arise (from differential thermal expansion) during the heating part of the cycle, or it could also occur during cooling under a thermal gradient. With an alumina substrate, which has a lower coefficient of expansion than the YSZ coating, such stresses would be tensile only during cooling in an isothermal system. Nevertheless, deep segmentation cracks appear to form readily in both cases. Furthermore, once formed, they were found to persist throughout prolonged holding at high temperature, suggesting that they rapidly become too wide to be readily healed during the high temperature dwell.

In all spallation cases, “partial spallation” was observed, in the form of debonding and detachment of sections of the coating between segmentation cracks and the edge/corners of the sample. Photographs of samples illustrating this effect are shown in Figure 6-5, and all other specimens in this study were observed to spall in a similar fashion. All such substantial debonding events tended to be classified as spallation (where more than 10% of the total coating area were observed to spall off) when viewed via the webcam. However, this meant that careful geometrical characterisation of the spalled specimens was then required in order to apply an energy-based fracture mechanics analysis. It was necessary to take into account the relatively small area of many of the debonded regions, and a significant fraction of the spalled material was close to either a segmentation crack or the edge.

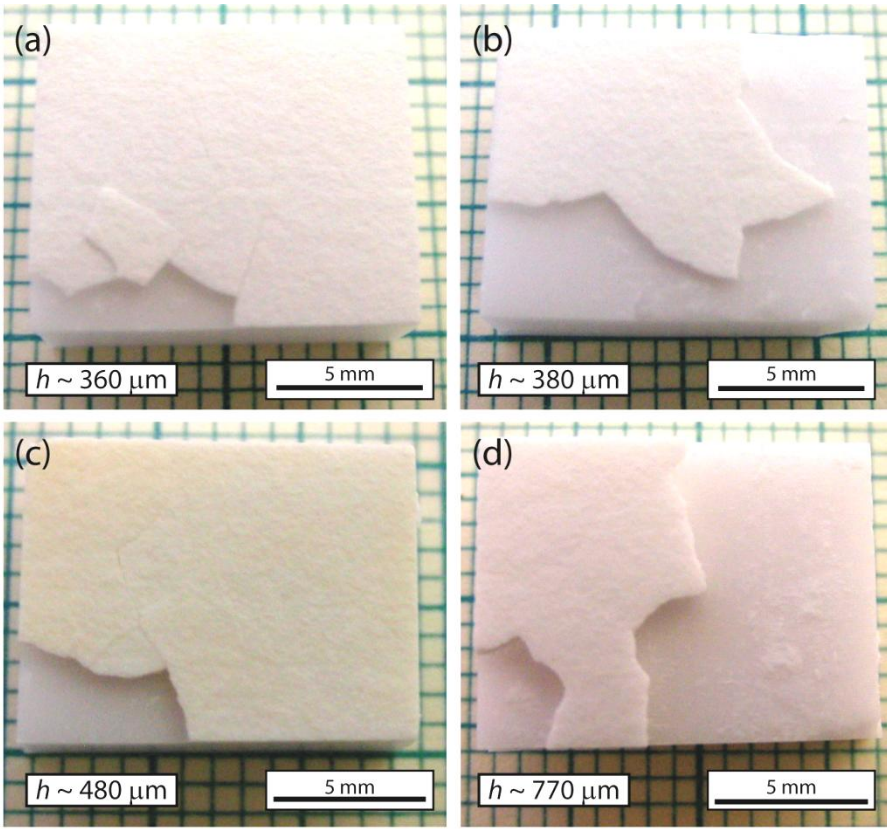

Figure 6-5 Optical photographs of 4 YSZ/alumina samples after heat treatment at 1500°C, showing partial coating spallation.

Within regions of the coating close to segmentation cracks, or to specimen edges, the in-plane stresses responsible for driving spallation become partially relaxed and a correction is required to account for this effect. At such a lateral free surface, the in-plane stress in the coating normal to that plane (which would be the stress driving an interfacial crack from this region) must fall to zero. There will be a characteristic distance, δ, on moving laterally away from the free surface, over which this stress gradually rises to the far field bulk value. The assumption is made here that this stress rises linearly from zero at the edge to σ_0 at a distance δ away from it, as described by the following equations:

$$\begin{aligned} \sigma(x) &= \left(\frac{\sigma_0}{\delta}\right)x \quad \text{for } x \leq \delta \\ \sigma(x) &= \sigma_0 \qquad\quad \text{for } x \geq \delta \end{aligned}$$

Equation 6-3

Equation 6-4 below gives the expression for the stored elastic energy, U, assuming linear elastic behaviour (with an equal biaxial stress state) associated with one of the two in-plane stresses. This expression is derived assuming that only the stress parallel to the crack propagation (of the two components making up the equal biaxial stress state) can be relaxed as the crack passes since the other in-plane stress is still constrained.

$$U = \frac{1}{2}\text{stress} \times \text{strain} \times \text{volume} = \frac{(1-\nu)\sigma^2}{2E} \times \text{volume}$$

Equation 6-4

So that the energy in a relaxed region near a free edge may be written as:

$$\begin{aligned} U_{\text{edge}} &= \frac{(1-\nu)}{2E}\int_0^\delta \sigma(x)^2\, hw\mathrm{d}x = \frac{hw(1-\nu)}{2E}\int_0^\delta \frac{\sigma_0^2 x^2}{\delta^2}\mathrm{d}x \\ &= \frac{hw(1-\nu)\sigma_0^2}{2E\delta^2}\left[\frac{x^3}{3}\right]_0^\delta \end{aligned}$$

Equation 6-5

where w is the width of the region concerned and h is the coating thickness. Equating this width to L, the (measured) perimeter of the relaxed region, leads to the following expression:

$$U_{\text{edge}} = \frac{\sigma_0^2 L h \delta (1-\nu)}{6E}$$

Equation 6-6

The stored elastic energy in regions remote from the edge and the segmentation cracks is given by:

$$U_{\text{bulk}} = \frac{\sigma_0^2(1-\nu)}{2E}\left(A_{\text{f}}h - Lh\delta\right)$$

Equation 6-7

where A_{f} is the total interfacial fracture area.

Hence the total energy stored is given by:

$$\begin{aligned} U_{\mathrm{tot}} &= \frac{\sigma_0{}^2(1-\nu)}{6E}(Lh\delta) + \frac{\sigma_0{}^2(1-\nu)}{2E}(A_{\mathrm{f}}h - Lh\delta) \\ &= \frac{h\sigma_0{}^2(1-\nu)}{2E}\left(A_{\mathrm{f}} - \frac{2L\delta}{3}\right) \end{aligned}$$ Equation 6-8

The interfacial strain energy release rate is obtained on dividing this expression by A_{f}. Equation 6-9 below is the expression for the interfacial strain energy in terms of strain rather than stress. Comparing the resultant expression with Equation 6-1, reveals that the net effect is to introduce a geometric correction factor accounting for stress relaxation effects, which reduces the driving force by a significant fraction:

$$G_i = \frac{hE(\Delta\alpha\Delta T)^2}{2(1-\nu)}\left(1 - \frac{2L\delta}{3A_{\mathrm{f}}}\right)$$ Equation 6-9

The value of δ cannot be obtained rigorously as it is sensitive to details of the way surrounding material is constrained, but its magnitude is expected to be of the order of h, the coating thickness, at least approximately, and this assumption was made in the current work. Poisson's ratio, ν, was taken to be equal to 0.22 [12]. Values of A_{f} and L were measured by processing images of the spalled specimens, such as those shown in Figure 6-5, using the software "ImageJ" (see Figure 6-6). The correction factor of (1 - ($2L\delta/3A_{\mathrm{f}}$)) had a value in the range of 30 – 70% for these specimens, depending on the size of the spalled region, thus having a significant impact on the values for the resulting critical strain energy release rate.

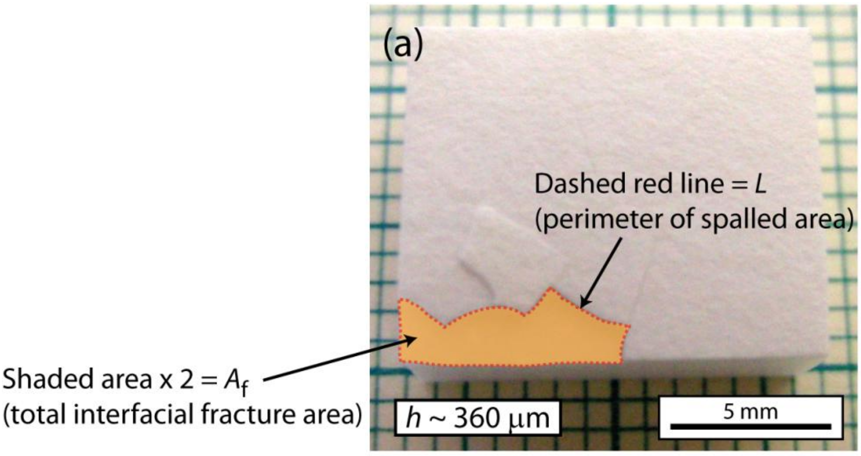

Figure 6-6 The illustration above shows exactly how parameters L (perimeter of the spalled area) and A_f (total interfacial fracture area) were evaluated by image analysis. The spallation specimen corresponds to the one shown in Figure 6-5(a).

6.7 Deduction of Interfacial Fracture Energies

For each of the spallation specimens, estimates of the critical strain energy release rate (G_{ic}) were obtained by substituting measured values of A_{f} and L into Equation 6-9, together with the estimated value for the misfit strain (2.2 millistrain) and the Young's modulus corresponding to the heat treatment concerned (Figure 6-2). There are fewer data points in Figure 6-7 than in Figure 6-4 because for some specimens, the heat treatment (including periodic quenching) was not terminated until it had continued well beyond the initial spallation event. The spallation lifetime (Figure 6-4) for such specimens had been captured on video, but the repeated subsequent exposure to cooling jets caused the coatings to rapidly disintegrate (with further partial spallation taking place), so the image analysis needed to determine variables in Equation 6-9 could not be carried out. Therefore the corresponding points could not be included in Figure 6-7. While there is certainly some scatter in the data (of approximately a factor of 2) shown in Figure 6-7, the results are consistent with an approximately constant value of G_{ic}, having a magnitude of the order of 300 J m^{-2}. This is encouraging, since it might be expected that the (YSZ/alumina) interface would not undergo much microstructural change (morphological or chemical), even when exposed to temperatures as high as 1500°C for extended periods, therefore consistent with an approximately constant value of G_{ic}.

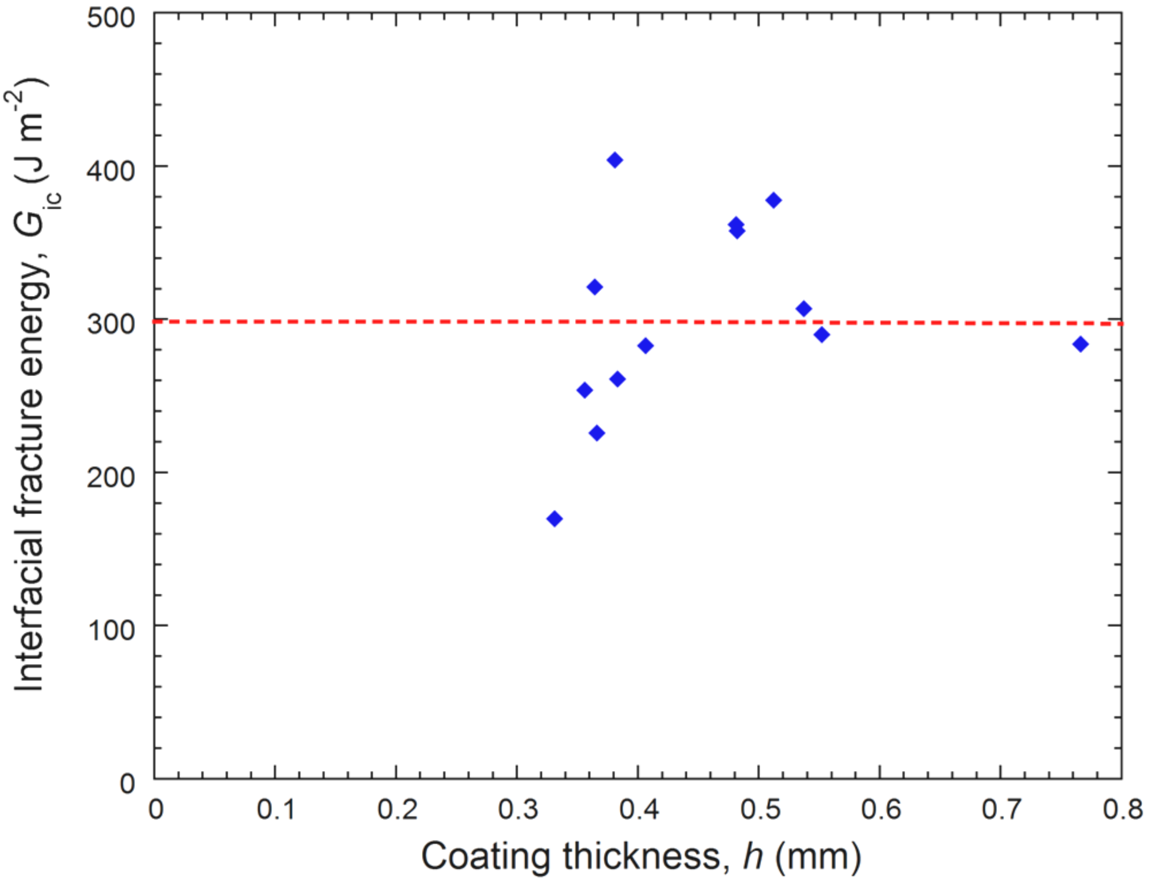

Figure 6-7 Interfacial fracture energy values, plotted as a function of coating thickness. These data were obtained using Equation 6-9, the spallation lifetime data in Figure 6-4 (conducted at 1500°C), the misfit strain during quenching ($\Delta\alpha\Delta T$ ~ 2.2 millistrain), the Young's modulus corresponding to the heat treatment concerned (Figure 6-2) and measured values of A_f and L. Each data point represents a single spallation event.

It is also worth noting that this G_{ic} value implies that the alumina/YSZ interface is a fairly tough one. It may be noted that interfacial cracks propagating under this type of driving force will be doing so under predominantly mode II (shearing mode) loading. The appropriate fracture energy value will therefore be that for mode II, which will tend to be appreciably higher than the value for the same interface under mode I (opening mode) loading conditions [100, 122]. Typically the interfacial fracture energy is found to increase with phase angle loading (a measure of the relative shear to opening mode loading at the crack tip). This is primarily due to crack shielding caused by the non-planarity of the interface. This is consistent with it having a rough topography as a result of the laser treatment, and good mechanical keying having been achieved between the two components due to the use of LPPS for the spraying. If the interface had been less rough, then debonding would have occurred more readily - i.e. without requiring such long exposures at high temperatures. It was indeed found during experimentation that in the cases where the alumina substrate surface was not sufficiently rough or the coating spraying was done by APS rather than LPPS, that premature debonding tended to occur either during the spraying (due to differential misfit strains which incur when the specimen cools in the short period in between spray passes or at the end of the programme), or during the first few hours of heat treatment with periodic quenching. In all spallation specimens fracture occurred predominantly along the interface, with little retention of YSZ splats on the substrate surface and vice versa. This is consistent with the assumption of brittle failure.

6.8 Section Summary

The following conclusions can be drawn from this chapter.

a) A simple methodology has been outlined for prediction of the spallation lifetimes of plasma-sprayed YSZ coatings, based on a global fracture mechanics criterion. This spallation criterion is simply the strain energy release rate associated with debonding reaching a critical value (i.e. the interfacial fracture energy), with this driving force being solely generated by the thermal misfit strain ($\Delta\alpha\Delta T$) associated with cooling from a stress-free upper temperature. In other words at elevated temperature, creep relaxation within the TBC prevents the build up of significantly large stresses. This way any complex analysis involving residual or internal stress states which may play an important role in the delamination process of the ceramic top coat is avoided. Upon rapid cooling of the system, it can often be assumed that all of the thermal misfit strain is accommodated in the coating, making it easy to estimate the associated stresses and thus the strain energy. This is reasonable, since the alumina substrate employed in this work is much thicker and stiffer in comparison. The cooling may in practice not be entirely elastic, depending on the cooling rate, but in cases where some stress relaxation occurs it should be possible to establish an effective temperature drop and hence an effective misfit strain. In this work, rapid cooling was established by gas quenching and considering the low ductility of TBCs below ~ 1100°C, it seems reasonable to assume that elastic response would occur in preference (to diffusive mechanisms such as creep and plastic deformation) during the cooling phase.

b) The experimental procedures presented in this work were designed to isolate the effects of sintering from those associated with any changes in the interfacial microstructure and interactions between the coating and substrate. Effects arising from the presence of thermal gradients in the system were also avoided. This was achieved by using fully dense alumina substrates, as this allowed for specimens to be isothermally heat treated at high temperatures, and ensured that interface remained stable throughout. Misfit strains in this system on cooling to ambient temperature (of the order of a few millistrain) are similar in magnitude to those for conventional YSZ/superalloy combinations, although of opposite sign. Special processing procedures were developed, which involved laser treating the substrate surface in order to create a suitably tough interface. It was also necessary to take account of edge effects and the influence of segmentation cracks on the effective strain energy release rate (as in-plane stresses in the volume of the coating near those regions are partially relaxed).

c) Experimental data were obtained for the change in coating stiffness as a function of heat treatment time and temperature. Spallation lifetime data at 1500°C were also obtained, using a computer-controlled furnace system with a periodic quenching capability, for a number of specimens, covering a range of coating thicknesses. A strong correlation was established between lifetime and coating thickness, as expected for debonding driven by release of stored elastic strain energy, which is directly proportional to the thickness. Measured spallation lifetimes were consistent with an approximately constant value of the interfacial fracture energy (~ 300 J m^{-2}).

d) The methodology presented here should be applicable to conventional coating systems i.e. of TBC/superalloy combination. There are, of course, several complicating issues in real life systems. The interfacial region would undergo microstructural changes (primarily due to bond coat oxidation and interdiffusion of alloying species which may result in the formation of pores, cracks etc) during service. Nevertheless, it should be possible to determine the value of fracture energy of a conventional interface and also measure how this might change with time at temperature, and perhaps even identify an appropriate damage evolution law. It is also important to recognise that the model incorporates certain assumptions, such as the coating being stress-free at elevated temperature and the focus being on crack propagation being energetically favourable, rather than on crack initiation or sub-critical crack growth. The latter point relies on the assumption that suitable flaws where crack propagation may initiate are already present along or near the interface. The likelihood for crack propagation may also be affected by edge effects and specimen geometry. Finally, it may be noted that certain practical points immediately follow from the conclusions of this work, such as the potential value of monitoring the stiffness of the coatings in order to evaluate their remaining lifetime.

7.0 The Effect of Vermiculite and Volcanic Ash on the Degradation and Spallation Lifetime of TBCs

In this chapter the effect of vermiculite (VM) and volcanic ash (VA) contamination on the sintering-induced spallation lifetime of PS TBCs was investigated. Commercially available VM powder was deemed to have a composition similar to siliceous compounds ingested by aviation engines. VA powder was collected from the Laki volcanic vent in Southern Iceland. The presence of both VM and VA was found to induce deleterious microstructural changes in the coatings which accelerated the rise in their Young's modulus. Spallation results show that coating lifetime may be significantly reduced, even at relative low VM/VA addition levels (~ 1 wt.%), due to the loss of strain tolerance caused by the penetration of glassy deposits and accelerated sintering. This simple result gives a clear insight into the role CMAS plays in destabilizing TBCs by degrading its in-plane compliance. The results presented in this chapter were published in [260].

7.1 Effect of VM and VA Deposits on Coating Microstructure

7.1.1 Ingression of VM Melt into the Coating

Figure 7-1 shows BSE images of transverse polished cross sections of detached YSZ coatings, with 1.8 wt.% surface addition of VM, after different heat treatment times at 1200°C. Corresponding EDX mappings for Si are also shown. These images suggest that the initial treatment causes sufficient decrease in the viscosity of the VM that it readily spreads over the coating surface, followed by rapid penetration into the porosity of the regions near the surface of the coating. Typical porosity levels in PS YSZ, and also in those produced by EB-PVD, are about 10 – 15 vol.%, with most of it being interconnected. It seems likely that the glassy amorphous layer retains its integrity, although there are clear indications that a significant proportion of the surrounding zirconia dissolves in it. This of course is a well known thermo-chemical interaction between YSZ and CMAS-type deposits, as outlined in [208]. For example, the depth of the liquid layer is apparently about 70 – 80 μm (after 10 mins of heat treatment), whereas its thickness would be less than half that if it were composed solely of the original VM.

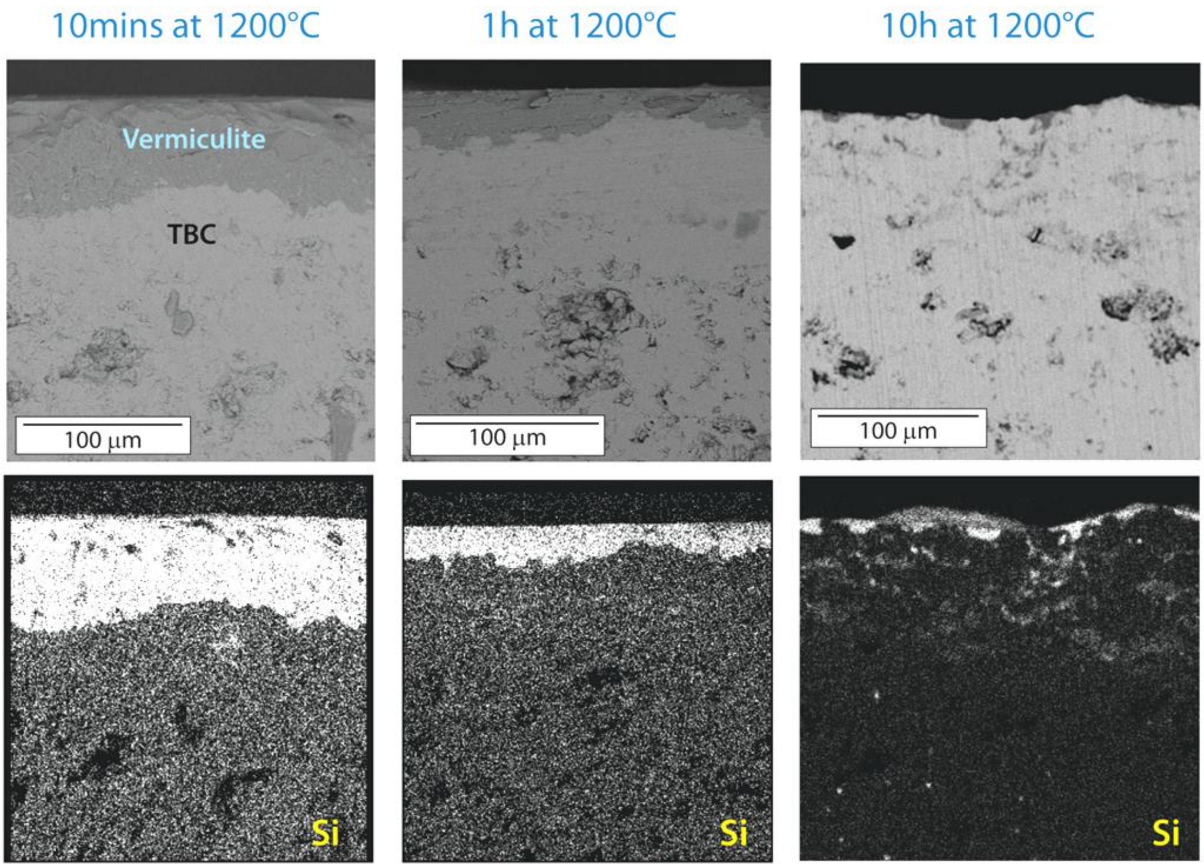

Figure 7-1 Showing transverse section BSE images of PS TBC with 1.8 wt.% surface addition of VM, after 10 minutes, 1 h and 10 h isothermal exposure to 1200°C, and their corresponding EDX mappings, following the movement of Si.

Further evidence show that the Si-rich region created initially (i.e. after 10 minutes) was composed of a mixture of glassy VM species and residual crystalline zirconia. This is provided by the XRD profiles shown in Figure 7-2, obtained from the free surface of a specimen with 3 wt.% VM addition, and data is presented for increasing heat treatment times at 1200°C. It can be seen that the initial XRD profile exhibits essentially just a substantial broad peak at 20 – 30° 2θ, reflecting the presence of an amorphous phase, superimposed with the sharp peaks corresponding to t' YSZ. It was found that the amorphous phase proportion was roughly 50% after 10 minutes of heat treatment at 1200°C. This implies that the dissolution of a substantial proportion of the original zirconia grains had taken place. These figures are of course approximate, and it should be noted that the VM addition level was higher in the specimen used to produce the spectra in Figure 7-2, compared with the one used to create Figure 7-1. However, they both point towards a consistent picture concerning the early stages of the VM infiltration mechanism.

The other Si maps in Figure 7-1 suggest that, after longer heating times (1 h and 10 h), the Si-rich (i.e. the heavily liquid infiltrated) layer gradually disappears, presumably by the diffusion of the VM species into the rest of the coating. This method of monitoring the Si distribution is not suitable for the construction of an accurate composition profile, but it would appear that these species become homogeneously distributed throughout the coating fairly quickly. It seems likely that the diffusion takes place predominantly along the grain boundaries.

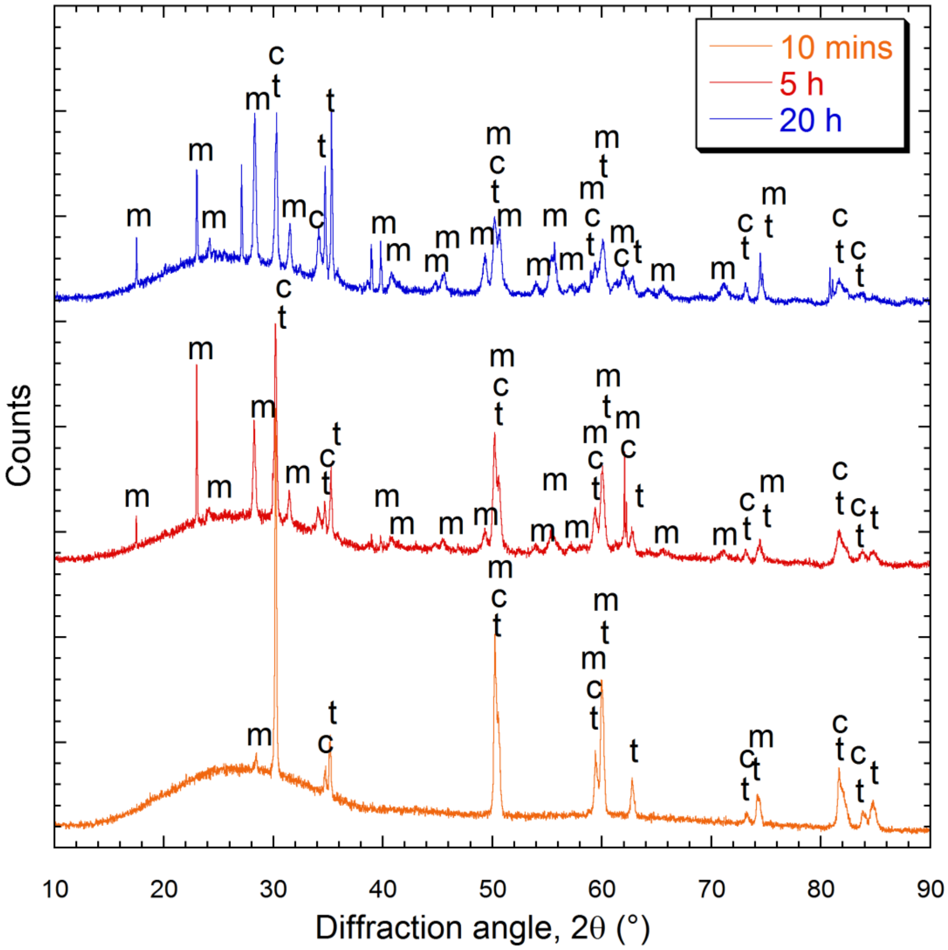

Figure 7-2 XRD profiles from the free surface (the VM infiltrated side) of a YSZ specimen, with 3 wt.% VM surface addition, after different periods of holding at 1200°C (where m = monoclinic, t = tetragonal and c = cubic phases).

The XRD spectra for the longer times shown in Figure 7-2 also give some important insights into the VM ingression mechanism taking place. These show a gradually reducing intensity of the amorphous peak, accompanied by increasing intensities for the tetragonal zirconia peaks and also the appearance of some strong peaks characteristic of monoclinic zirconia - located at around 28° and 32° (2θ). The amorphous phase content had reduced to around 40% (from the initial 50%) after 20 h of heat treatment at 1200°C. This is consistent with a progressive penetration (by viscous flow) of VM species into the bulk of the coating, reducing the amount of residual liquid. It also seems that the dissolution and reprecipitation of zirconia grains simultaneously takes place. It may be noted that peaks corresponding to crystalline VM were not detected. However, a peak (at around 27°) that could possibly be identified as $ZrSiO_4$ becomes apparent after 20 h at 1200°C. Other phases that could conceivably be responsible for this peak include iron oxide, silicon oxide (quartz) and potassium zirconium silicate. Of course this spectrum alone does not allow a confident conclusion regarding the formation of new crystalline phases to be drawn, although it would not be surprising if this phase were to be formed, since it has been reported previously [249] during similar experiments.

Figure 7-3 shows XRD spectra of YSZ, with 3 wt.% VM surface additions, after treatments of 5 h and 20 h at 1200°C. These specimens were subjected to careful mechanical polishing/lapping in order to remove the partially glassy top layer. These spectra indicate that, while the structure is fully crystalline, the presence of VM still induces some monoclinic zirconia to form at this depth. Such results were previously masked by the presence of the large amorphous peak. This is not unexpected, since it is known that high levels of CMAS-type impurities often promote formation of the monoclinic phase, caused by the dissolution (and the leaching out) of yttria by the silica rich amorphous phases that rapidly infiltrate and diffuse into the bulk of the coating [208, 249]. Since this is a diffusion controlled mechanism, it is not surprising that the monoclinic peaks are more prominent after 20 h of heat treatment. This observation is also consistent with the idea that species from the VM rapidly diffuse into the bulk of the coating.

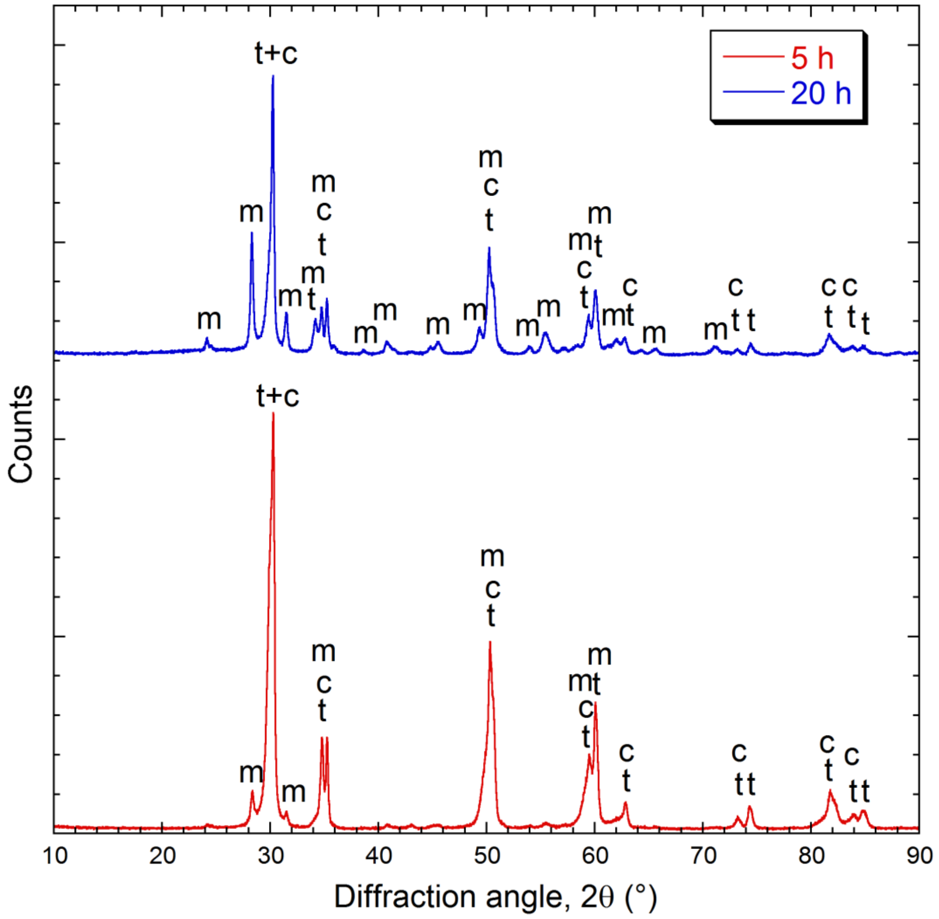

Figure 7-3 XRD profiles of YSZ specimens, with 3 wt.% VM surface additions, after 5 h and 20 h at 1200°C (where m = monoclinic, t = tetragonal and c = cubic phases). These spectra were obtained after the top glassy layer had been removed by polishing (to depths of, respectively, about 100 μm and 60 μm).

7.1.2 Sintering-Induced TBC Stiffening and Shrinkage with VM and VA

The Young's modulus data for free-standing YSZ coatings, with and without surface additions of VM and VA are shown in Figure 7-4 and Figure 7-5. The error bars represent standard deviations on sets of between 2 and 4 specimens in each case. Although data in the cases where CMAS additions were made were only obtained up to 5 – 10 h of heat treatment, it is clear that both VM and VA substantially accelerate the rate of stiffening caused by sintering effects. Measurements were only made up to 5 – 10 h because specimens either had embrittled so much they tended to thermally fracture during subsequent heat treatments, or in other cases measurements were terminated because substantial curvature development was detected. Curvature, particularly in the transverse direction is known to raise the apparent beam stiffness substantially (see section 6.3). The origin of such curvatures in this case are from differential sintering in the through-thickness direction, as CMAS powers were only applied onto one side of the TBC specimens. The increase in stiffness is particularly marked for the case of VM at 1500°C in Figure 7-4, where a substantial amount of liquid present was present, and much of the sintering was liquid-assisted (i.e. involved viscous flow by capillary action into the pores and defects). The high Young's modulus value measured (~ 110 GPa) after just 1 h of heat treatment is plausible since such high level of CMAS incorporation should raise the stiffness value to at least that of typical glasses (E_{glass} ~ 90 GPa) and in fact would be expected to be even higher as dense YSZ has a stiffness value of around 200 GPa. Even at a lower temperature of 1200°C, the effects of such CMAS additions at these levels are very significant. These results are consistent with the microstructural observations presented in section 7.1.1.

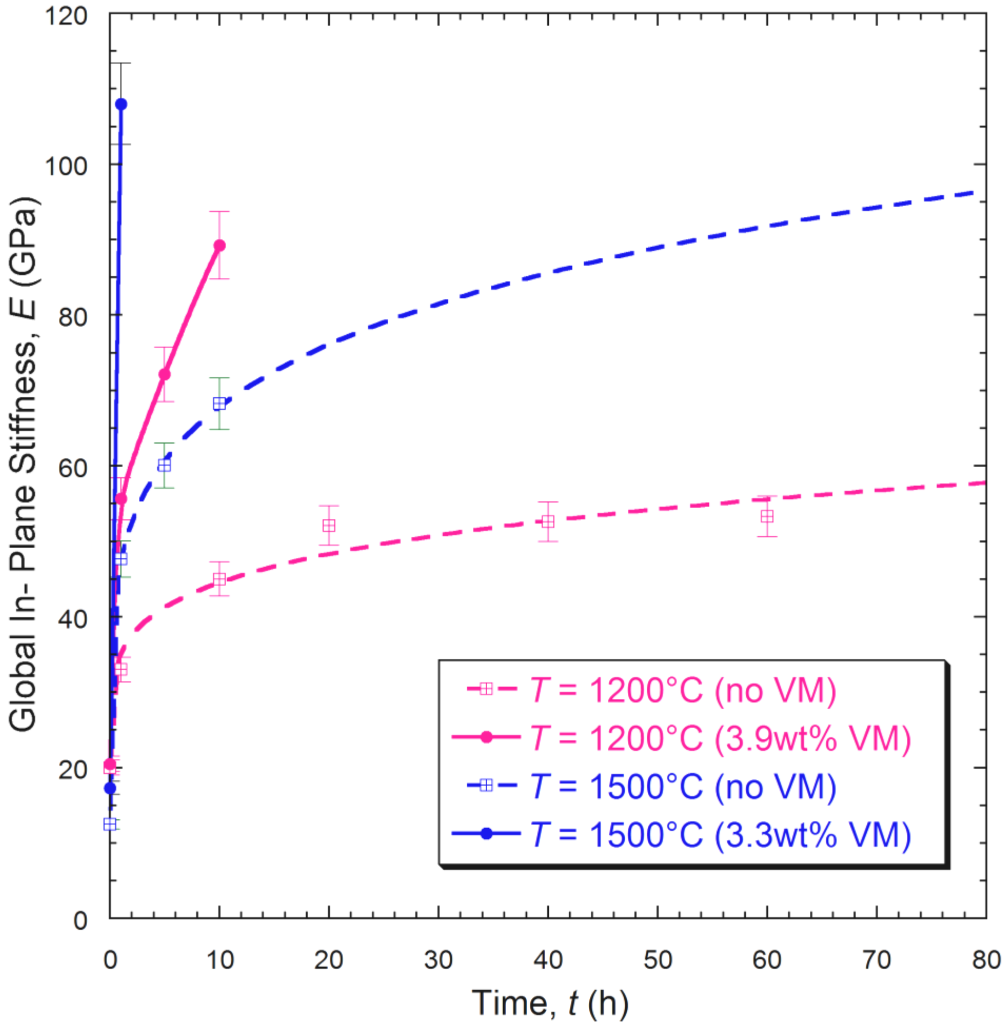

Figure 7-4 Young's modulus data for free-standing YSZ coatings for samples with VM additions, at 1200°C and 1500°C. The error bars represent standard deviations on sets of between 2 and 4 specimens in each case.

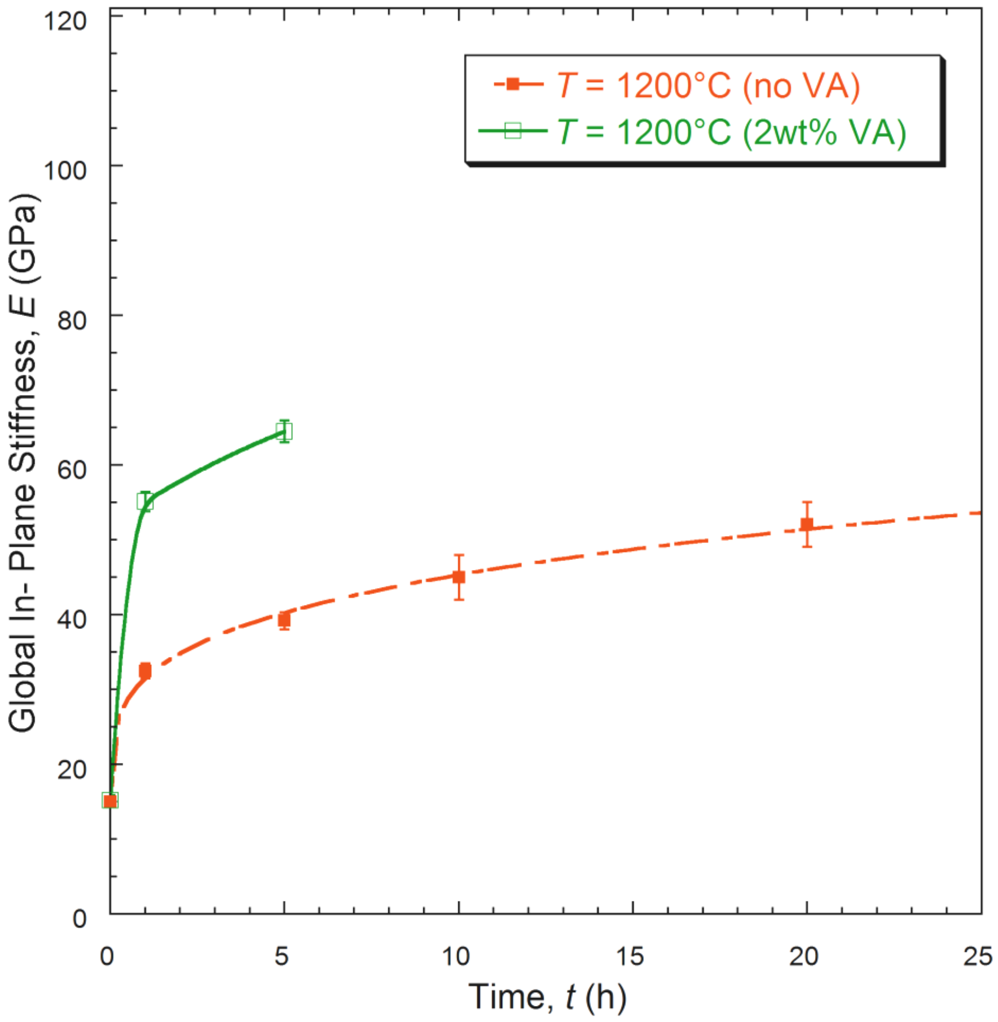

Figure 7-5 Young's modulus data for free-standing YSZ coatings for samples with VA additions, at 1200°C. The error bars represent standard deviations on sets of between 2 and 4 specimens in each case.

Further conclusions on the effect of VM additions on the sintering behaviour at high temperature can be drawn from Figure 7-6, which show dilatometry data. It can be seen that the sintering induced in-plane shrinkage is considerably accelerated by the presence of the VM. It is worth noting that this shrinkage reflects only the effects of grain boundary diffusion, as it is well known that surface diffusion does not cause shrinkage. Although both types of diffusion do contribute to the associated stiffening [178, 179]. The fact that the VM accelerates the shrinkage is consistent with its promotion of sintering being primarily due to substantially enhanced diffusion and mass transport at the grain boundaries and free surfaces.

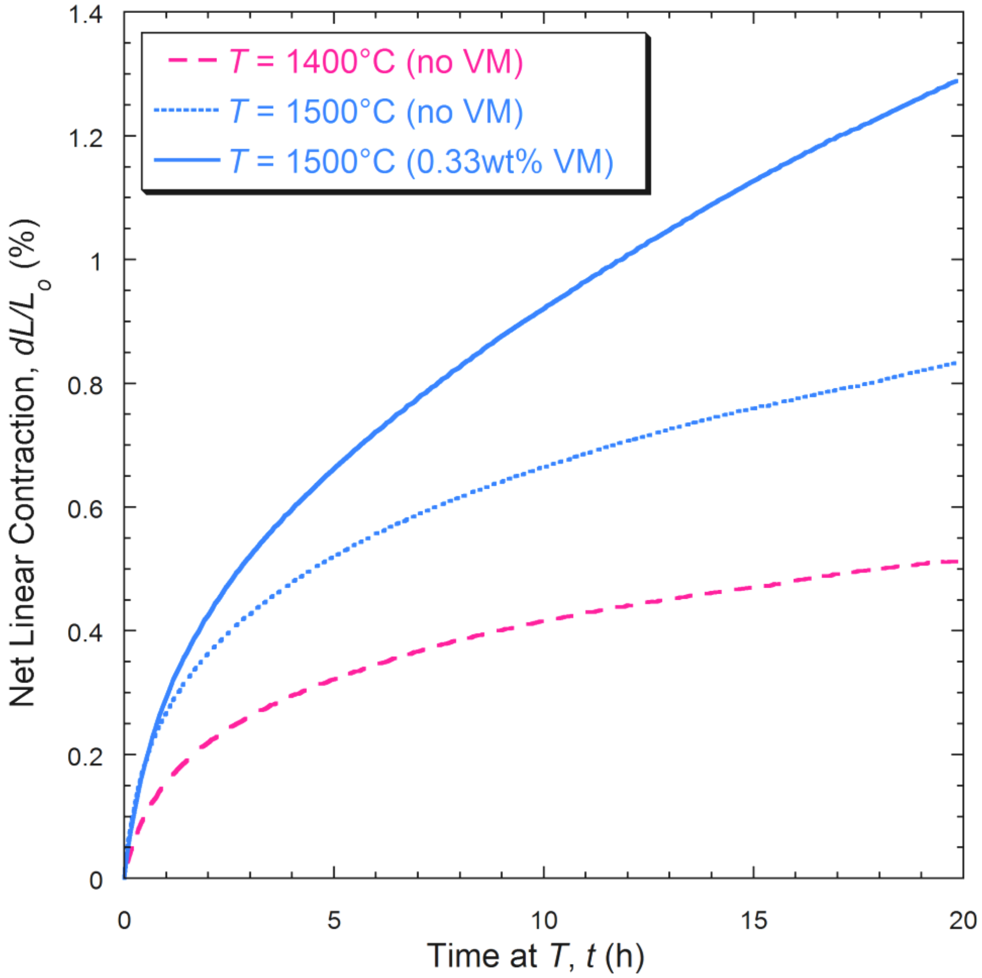

Figure 7-6 Dilatometry data obtained during heating of free-standing YSZ coatings at 1400°C, and also at 1500°C (with and without VM additions).

7.2 Spallation Lifetimes with VM and VA

Spallation lifetimes at 1500°C, measured as a function of VM concentration, are shown in Figure 7-7. It can be seen that even relatively low VM addition levels (less than 1 wt.%) can have a pronounced effect in reducing spallation lifetime at this very high temperature. This is consistent with the stiffness and dilatometry data. The plot in Figure 7-8 shows corresponding spallation data for VA additions, at a lower holding temperature of 1200°C. In this case also, there is a dramatic effect. In fact, considering that the temperature is lower, such that, in the absence of any CMAS, the lifetime is expected to be very long, it can be seen that the VA has a stronger effect than the VM. In fact, coating specimens without any CMAS additions were observed not to fail past 300 h of heat treatment at 1200°C. This is unsurprising in view of the fact that the VA has lower T_g and melting temperatures than the VM (see Figure 5-8). This simple result gives a clear insight into the role CMAS plays in destabilizing TBCs by degrading its in-plane compliance. Significant levels of CMAS infiltration would, of course, lead to other coating property changes such as coefficient of thermal expansion and thermal conductivity. However, regarding spallation resistance, the dominant effect is caused by the substantial rise in coating stiffness.

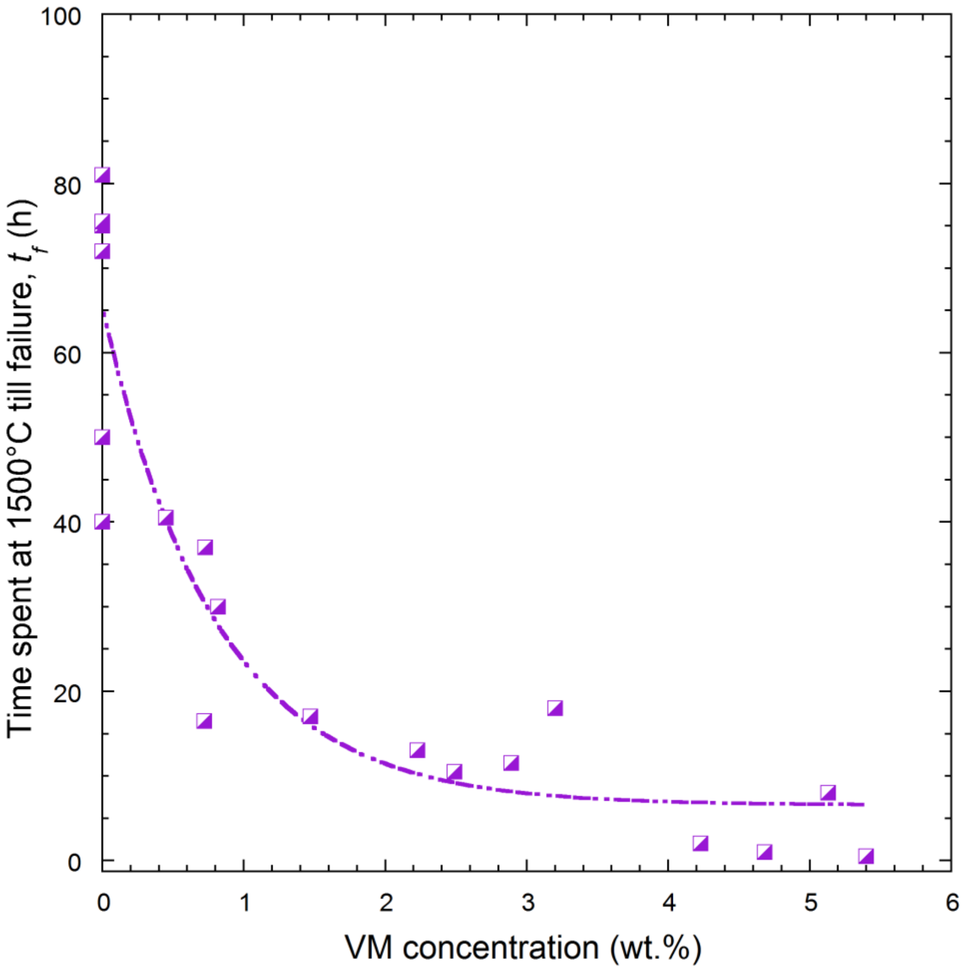

Figure 7-7 Spallation lifetime results obtained for 1500°C, as a function of VM surface addition level. Specimen coating thicknesses were on average 740 μm. When the VM concentrations are expressed as mg cm^{-2} instead, the data points range from 0 – 18.2 mg cm^{-2}. Each data point represents a single spallation event. The line has been included as a guide to the eye.

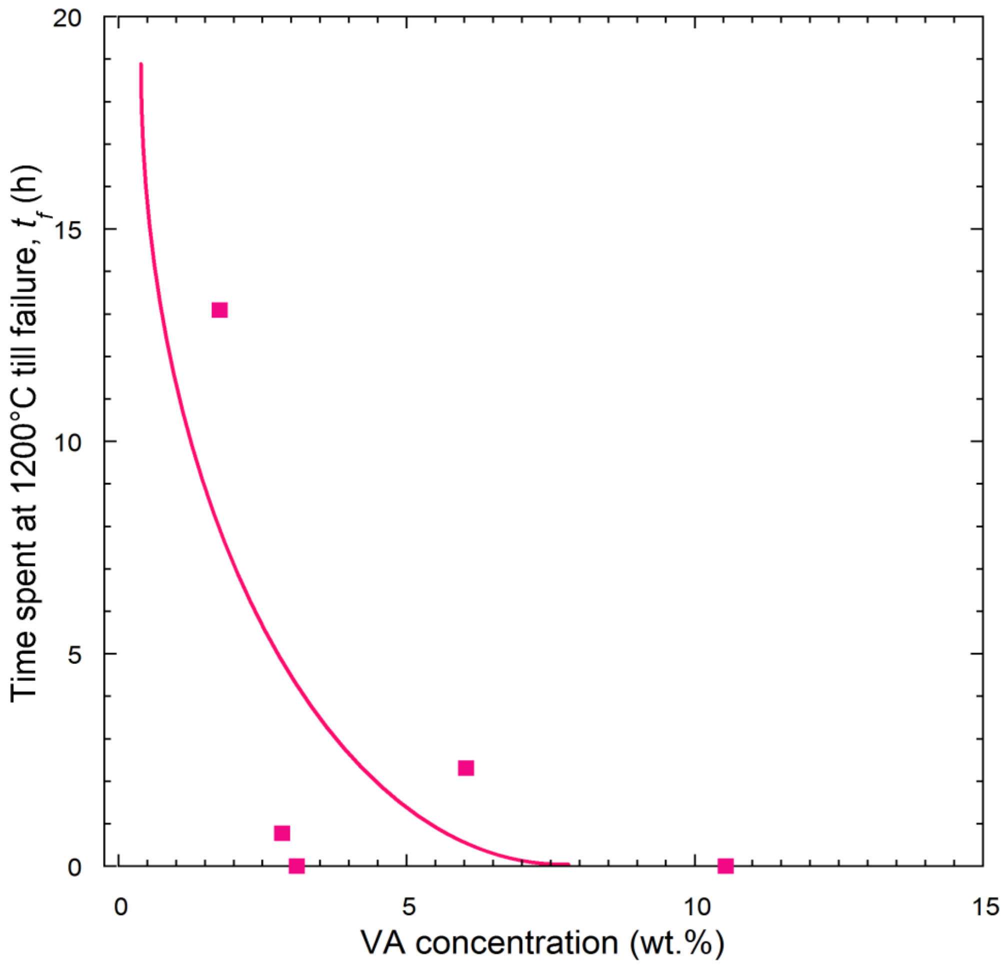

Figure 7-8 Spallation lifetime results obtained for 1200°C, as a function of VA surface addition level. Specimen coating thicknesses were on average 650 μm. Coating specimens without any VA additions were observed not to fail past 300 h of heat treatment. When the VA concentrations are expressed as mg cm^{-2} instead, the data points range from 3.6 – 24.7 mg cm^{-2}. Each data point represents a single spallation event. The line has been included as a guide to the eye.

Previously in sections 5.1 and 6.0, a fracture mechanics based methodology was presented for the estimation of the critical strain energy release rate from a measured spallation lifetime, by knowing the coating stiffness as a function of time at the temperature when failure was observed. It was found that the interfacial fracture energy, for the cases where there was no CMAS, had a value of about 300 ± 100 J m^{-2}. The interface for the specimens used in these CMAS experiments was produced in an identical manner. Thus the fracture energies for cases with CMAS were determined by a similar methodology. However, there were only four data points for which the stiffness as a function of time and CMAS level was available. These data are presented in Table 7-1, where it can be seen that the estimated interfacial fracture energies were about 200 – 500 J m^{-2} for the VM additions and 100 – 200 J m^{-2} for the VA additions. There is an issue, of course, that these values are very approximate and based on minimal data. However, it is still worth noting that they are roughly similar to those obtained in the absence of CMAS, in which case a more systematic set of data was obtained. This is expected, since the interface remained more or less stable (judging by inspection of specimen interfaces post spallation). However, it is plausible that should some CMAS reach the interface, it may possibly contribute to its degradation (creation of voids, cracks etc) and thus reduce the interfacial fracture energy as a result. It is possible this may have happened to some degree in the specimens with VA additions, as the fracture energies are observed to be slightly lower.

Time at T = 1500°C (h)	VM level (wt.%)	Predicted E (GPa)	G_{ic}
2	4.2	199	470
1	4.7	108	240
Time at T = 1200°C (h)	VA level (wt.%)	Predicted E (GPa)	G_{ic}
0.8	2.8	54	110
13.1	1.8	71	150

Table 7-1 Calculated values of the critical strain energy release rate, G_{ic}, using spallation lifetime to estimate its stiffness.

7.3 Section Summary

The following conclusions may be drawn from this chapter.

a) A study was undertaken on the effects of the addition of two types of CMAS (calcia-magnesia-alumina-silica) powders (Vermiculite (VM) and a volcanic ash, (VA)) to the free surfaces of plasma-sprayed zirconia coatings, either free-standing or attached to an alumina substrate. These specimens were subject to heat treatments (in the temperature range 1200 – 1500°C). Attention has been drawn on both the microstructural changes induced as the powders softened/melted and infiltrated the coatings and how this affected the sintering behaviour. Coating stiffness and shrinkage was monitored (as a measure of the progression of sintering) and their spallation lifetimes as a function of CMAS addition level were measured.

b) It was found that molten VM and VA penetrate rapidly into the bulk of the coating. Depending on the heat treatment temperature, a layer is formed which is a mixture of liquid and residual zirconia grains, where some of the original zirconia were dissolved in the liquid and then subsequently reprecipitated. This liquid infiltrated layer progressively lessens, as species within it diffuse deeper into the coating. Diffusion takes place predominantly via the grain boundaries and free surfaces, and eventually the elements concerned become uniformly distributed throughout the coating. This tends to happen fairly quickly. For example, a near homogenous distribution of VM is achieved in a few tens of hours at 1200°C, for a coating thickness of about 500 – 700 μm and a surface CMAS addition level of a few wt.%.

c) This ingression of VM and VA accelerates the coating sintering behaviour, predominantly by promoting grain boundary diffusion. This is demonstrated by enhanced coating shrinkage and more rapid stiffening. As a consequence, when the coating is subject to heat treatment and periodic quenching, the more additions are made, the higher the likelihood of spalling. This is because upon cooling (from a stress-free upper temperature), a misfit strain arises (due to differential thermal contraction) and the resultant strain energy release rate is increased by the accelerated stiffening of the coating.

d) It is clearly shown here that the penetration of VM and VA species has the potential to compromise the thermo-mechanical stability of YSZ coatings. While the present work has only been carried out on plasma-sprayed TBCs, it is expected that the conclusions apply equally to those produced by EB-PVD. However, it is important to note that this type of damage can only occur if particles (ingested by the gas turbine engine) do sufficiently impinge on TBC surfaces and also subsequently deposit at significant concentration levels. There are several basic conditions which must be met for efficient sticking of ingested CMAS. For example, these particles must have low glass transition/melting point such that sufficient softening/melting must be achieved before impact. The heating and acceleration behaviour is also a function of particle size. Particle size also determines the amount of inertia a particle has, and when it is carried by a fast moving gas stream, this will affect whether the particle will follow the streamline or deflect away from it, if the flow happens to turn rapidly. These ideas are explored further in chapter 8.0.

e) Novel coating formulations may be devised (and indeed a few candidates have been reported in recent literature, see section 4.4) with improved resistance to the CMAS-induced microstructural changes responsible for enhanced sintering. Understanding the complex thermochemical and thermomechanical reaction between CMAS and YSZ is essential for developing alternate coating compositions, which should be designed to mitigate CMAS attack.

8.0 Deposition of Volcanic Ash on Surfaces in the Turbine of a Small Jet Engine

In this chapter the adhesion characteristics of ingested volcanic ash has been studied using a small jet engine. The effects of two engine speeds and four particle size distributions were investigated. Particulates were fed into the air intake at a controlled rate and deposition on turbine surfaces was qualitatively assessed using an optical fibre borescope. Deposition mainly occurred on the nozzle guide vane leading edges and the adjoining blade platform. It was not observed on the rotor blades. A simple numerical model was used to predict particle acceleration and heating in flight. It was observed and predicted that relatively large particles (~ 100 μm) are more likely to adhere than smaller ones, because they have greater inertia and thus are more likely to impact a turbine surface. Estimated values of Stokes numbers for the different particle sizes, in the gas environment concerned, are broadly consistent with this. The temperature of the larger particles at the end of their flight was predicted to be below their softening point. However, since the stationary component surface temperatures are expected to be hotter than the particles themselves, adhesion of such particles is apparently probable, by softening straight after impact. Particles larger than around 100 μm would probably not adhere, since they would be much too cold, but also the ingestion of such large particulates is not very likely. The results presented in this chapter are currently in press for publication [261].

8.1.1 Numerical Modelling of Particle Acceleration

Particle acceleration and heating were modelled in a 1-D Lagrangian frame of reference. Particles are assumed to move predominantly under the influence of the drag force exerted by the gas, F_{drag}, so that particle location is determined by the following equations [220, 227]:

$$\frac{\mathrm{d}x_{\mathrm{p}}}{\mathrm{d}t} = U_{\mathrm{p}} \quad \text{Equation 8-1}$$

$$\frac{m_{\mathrm{p}}\,\mathrm{d}U_{\mathrm{p}}}{\mathrm{d}t} = F_{\mathrm{drag}} = \frac{\rho_{\mathrm{f}} A (U_{\infty} - U_{\mathrm{p}})^2 C_{\mathrm{D}}}{2} \quad \text{Equation 8-2}$$

where x_{p} is the particle displacement, m_{p} is the particle mass, U_{p} is the particle velocity, A is the particle frontal area, C_{D} is the drag coefficient, ρ_{f} is the carrier fluid (air) density and U_{∞} the free stream velocity.

The following assumptions are also made:

- Particles are rigid spheres
- Gas flow is laminar
- The density of the particulate is much higher than that of the gas ($\rho_\mathrm{p} >> \rho_\mathrm{f}$)

Under these conditions, the particle equation of motion reduces to:

$$\frac{\mathrm{d}U_\mathrm{p}}{\mathrm{d}t} = \frac{3}{4}\frac{\rho_\mathrm{f}}{\rho_\mathrm{p}}\frac{C_\mathrm{D}}{D_\mathrm{p}}\left(U_\infty - U_\mathrm{p}\right)^2 \qquad \text{Equation 8-3}$$

where D_p is the particle diameter. A constant value of 0.5 was used for C_D, which is typical for a sphere at relatively high Reynolds numbers (of the order of 10^3). The particle Reynolds number is given by:

$$\mathrm{Re}_\mathrm{p} = \frac{\rho_\mathrm{f} D_\mathrm{p}\left|U_\infty - U_\mathrm{p}\right|}{\mu_\mathrm{f}} \qquad \text{Equation 8-4}$$

where μ_f is the air dynamic viscosity. Typical values for the particle Reynolds number calculated in this study were in the range 140 – 700, which are broadly consistent with those reported in literature of CMAS particles inside a gas turbine engine, which are in the range of 0 – 2300 [262].

The Stokes number (ratio of characteristic time, τ, of a particle suspended in fluid flow to the characteristic time of the fluid flow over an obstacle) can be expressed as:

$$\mathrm{Stk} = \frac{\tau U_\infty}{D_\mathrm{p}} \approx \frac{\rho_\mathrm{p} D_\mathrm{p}^2 U_\infty}{18\mu_\mathrm{f} L_\mathrm{c}} \qquad \text{Equation 8-5}$$

where L_c is the characteristic dimension of the obstacle. The Stokes number, as obtained using Equation 8-5, and taking the free stream velocity to be 365 m s^{-1}, particle density to be 2400 kg m^{-3}, gas viscosity to be 4.4×10^{-5} kg s^{-1} m^{-1} and obstacle dimension to be 10 mm (approximate turbine blade chord length of this particular gas turbine engine used), has a value of about 1,000 (representing a strong tendency to deviate from the gas streamlines) for a particle diameter of 100 µm, but a value of about 0.1 (representing a strong tendency to follow streamlines) for a particle diameter of 1 µm.

8.1.2 Numerical Modelling of Particle Heating

The particle was taken to be isothermal throughout its volume (i.e. Newtonian cooling conditions), initially at temperature T_0, and surrounded throughout by gas at T_∞. The equation describing convective heat exchange between gas and particle may be written:

$$Q = m_\mathrm{p} c_\mathrm{p,p} \frac{\mathrm{d}T_\mathrm{p}}{\mathrm{d}t} = h S_\mathrm{p} \left(T_\infty - T_\mathrm{p} \right) \qquad \text{Equation 8-6}$$

where Q is the heat flux, h is the convective heat transfer coefficient, $c_\mathrm{p,p}$ is the specific heat capacity of the particle, T_p is the particle temperature and S_p is the particle surface area. By expressing S_p and m_p in terms of D_p and ρ_p, the following equation is obtained:

$$\frac{\mathrm{d}T_\mathrm{p}}{\mathrm{d}t} = \frac{6h}{\rho_\mathrm{p} c_\mathrm{p,p} D_\mathrm{p}} \left(T_\infty - T_\mathrm{p} \right) \qquad \text{Equation 8-7}$$

Radiation is unlikely to have a significant effect over the temperature range of interest here and has hence been neglected. The heat transfer coefficient was estimated, as a function of the relative velocity between particle and surrounding gas, using the Ranz-Marshall correlation for the Nusselt number [263, 264]:

$$\frac{h D_\mathrm{p}}{k_\mathrm{f}} = \mathrm{Nu} = 2.0 + 0.6\,\mathrm{Re}_\mathrm{p}^{1/2}\,\mathrm{Pr}^{1/3} \qquad \text{Equation 8-8}$$

where k_f is the thermal conductivity of the gas and Pr is its Prandtl number, given by

$$\mathrm{Pr} = \frac{c_\mathrm{f} \mu_\mathrm{f}}{k_\mathrm{f}} \qquad \text{Equation 8-9}$$

with a value of about ~ 0.70 for air. Typical values for the heat transfer coefficient calculated in this study were in the approximate range 10 – 30 kW $\mathrm{m}^{-2}\,\mathrm{K}^{-1}$.

The input data used in the model are listed in Table 5-6. The free stream gas velocity was assumed to be equal to the calculated jet speed, V_jet. The jet speed was evaluated from the measured gross thrust, F_G, the inlet air mass flow rate, $\dot{m}_\mathrm{air}$, and the fuel consumption rate, $\dot{m}_\mathrm{fuel}$. The thrust is simply equated to the momentum flux:

$$F_\mathrm{G} = (\dot{m}_\mathrm{air} + \dot{m}_\mathrm{fuel}) V_\mathrm{jet} \qquad \text{Equation 8-10}$$

The far field gas temperature was assumed to be equal to the calculated turbine entry temperature, corresponding to the temperature at location 3 (T_3) in the schematic of a simple gas turbine engine, shown in Figure 5-14(b). This was evaluated assuming isentropic compression across the compressor (from the pressure ratios in Table 5-6) and using the perfect gas relationship for isentropic change:

$$\frac{T}{p^{(\gamma-1)/\gamma}} = \text{const.}$$

Equation 8-11

where p and T are the gas pressure and temperature, and γ is the ratio of the specific heat capacities of air (taken to be equal to 1.4 in this case). The combustion process was modelled as reversible and isobaric. The fluid (air) was modelled as an ideal gas throughout the cycle. The steady flow energy equation was used to evaluate the rate of heat release for the combustion process:

$$Q_{\text{combustion}} = \dot{m}_{\text{air}} c_{\text{p,air}} (T_3 - T_2) = \dot{m}_{\text{fuel}} LCV$$

Equation 8-12

where T_4 is the exhaust gas temperature (see Figure 5-14(b)), $c_{\text{p,air}}$ is the specific heat capacity of air (taken to be 1005 J kg^{-1} K^{-1}) and H_{fuel} is the calorific value of the kerosene (taken to be 43 MJ kg^{-1}). The total power input from combustion (at engine speed of 120,000 RPM) was found to be around 350 kW.

Finally, the following finite difference equations were used in order to solve Equation 8-1, Equation 8-2 and Equation 8-7 numerically, using Euler's method in Matlab:

$$x_{\text{p}}^{n+1} = U_{\text{p}}^{n} \Delta t$$

Equation 8-13

$$U_{\text{p}}^{n+1} = \frac{3}{4} \frac{\rho_{\text{f}}}{\rho_{\text{p}}} \frac{C_{\text{D}}}{D_{\text{p}}} \left(U_{\infty} - U_{\text{p}}^{n} \right)^2 \Delta t$$

Equation 8-14

$$T_{\text{p}}^{n+1} = \frac{6h}{\rho_{\text{p}} c_{\text{p,p}} D_{\text{p}}} \left(T_{\infty} - T_{\text{p}}^{n} \right) \Delta t$$

Equation 8-15

where Δt is the time step used in order to conduct the iteration. A value of 10^{-7} s was used, which gave adequate accuracy and stability of the modelling results.

The validity of the assumption of Newtonian cooling conditions (i.e. the particles are isothermal throughout) was checked for all cases studied by evaluating the Biot number:

$$\text{Bi} = \frac{hD_{\text{p}}}{k_{\text{p}}}$$

Equation 8-16

which needs to be well below unity for this to be a reliable approximation. The Bi values obtained were in the range 0.17 – 0.32, which is considered acceptable in the context of (order of magnitude) calculations of the type being carried out here.

The schematic shown below in Figure 8-1 summarizes the parameters and boundary condition used in this numerical modelling of particle acceleration and heating through the combustion chamber. Finally, all the input parameters used in the numerical modelling are listed in Table 8-1.

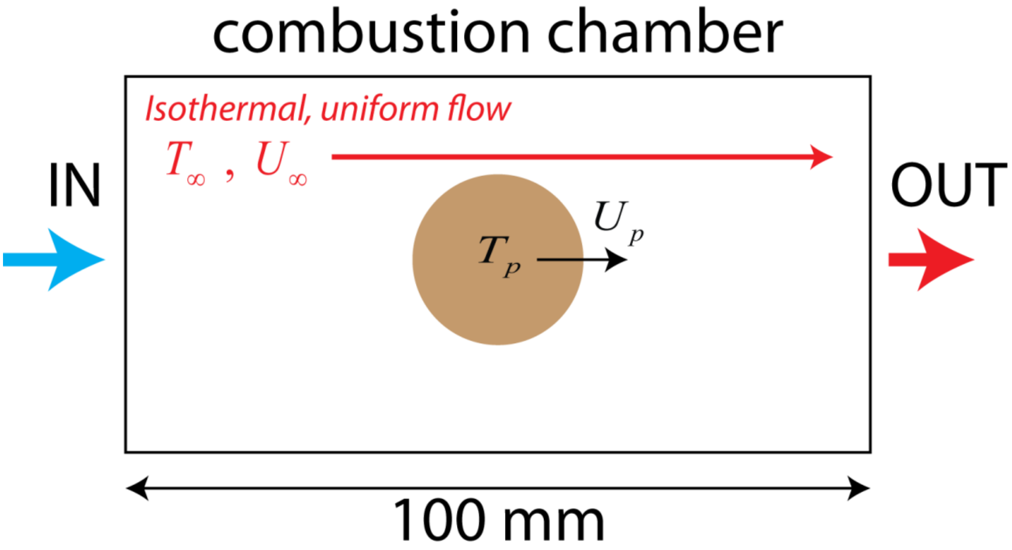

Figure 8-1 Schematic illustration showing parameters and boundary conditions used in the numerical modelling of particle acceleration and heating through the combustion chamber (not to scale).

Parameter	Engine speed (RPM)	
	120,000	62,000
Free stream velocity, U_∞ (m s^{-1})	365	115
Far field gas temperature, T_∞ (°C)	1070	710
Air density at T_3 and p_3, ρ_f (kg m^{-3})	0.84	1.04
Air dynamic viscosity at T_3, μ_f (kg s^{-1} m^{-1})	4.4×10^{-5}	4.0×10^{-5}
Air Prandtl number, $\mathrm{Pr_f}$	0.70	0.71
Air thermal conductivity at T_3, k_f (W m^{-1} K^{-1})	0.08	0.06
Particle density, ρ_p (kg m^{-3}) [265]	2400	
Particle thermal conductivity, k_p (W m^{-1} K^{-1}) [266]	2	
Particle specific heat capacity, $c_{p,p}$ (J kg^{-1} K^{-1})	800	
Initial particle velocity, U_0 (m s^{-1})	0	
Initial particle temperature, T_0 (°C)	20	
Drag coefficient, C_D (-)	0.5	

Table 8-1 Input parameters for particle acceleration and heating model

8.2 VA Powder Adhesion Characteristics

8.2.1 Observed Deposition Behaviour

Experimental parameters and deposition observations are summarized in Table 8-2. The observed deposition was assessed according to “Engine Damage Level”, the definition for which is found in Table 8-3. It is worth noting that the engine was completely stripped and any damaged components were re-serviced after each run. No deposition was observed when the engine was running at 62,000 RPM. This is not surprising, since the estimated turbine entry temperature, T_3, in this case was 710°C. Both the component surfaces and particle temperature at the end of flight was probably insufficient to cause deposition, the particles would have bounced off upon impact - and indeed signs of abrasion was apparent in some areas of the nozzle guide vane. On the other hand, when the engine was run at 120,000 RPM, for which the turbine entry temperature was estimated to be 1070°C, deposition was observed to be extensive in several cases. These cases will now be studied in some detail.

Run Code	VA grade	Engine speed (RPM)	VA feed rate (g min^{-1})	Duration (s)	VA injected (g)	VA concentration (g m^{-3})	Engine Damage Level
A	Fine	120,000	10.9	110	20	0.59	1
B	Medium 1	120,000	6.7	90	10	0.36	0
C	Medium 1	120,000	15	180	45	0.82	5
D	Medium 1	120,000	24	50	20	1.31	2
E	Medium 2	120,000	41.9	43	30	2.28	3
F	Coarse	120,000	2	30	1	0.11	0
G	Coarse	120,000	30	60	30	1.63	4
H	Fine	62,000	15.4	78	20	1.70	0
I	Fine	62,000	32.4	37	20	3.58	0
J	Medium 1	62,000	23.1	52	20	2.55	0

Table 8-2 Experimental parameters and deposition observations

Engine Damage Level	Description
0	No deposition
1	Small amounts deposition on blades and blade platform
2	Larger lumps of deposition on blades and blade platform
3	Larger lumps of deposition on blades and deposition observed over a significant area (~ 30%) of the blade platform
4	More deposition on blades and lumps deposited on blade platform cover a greater area (> 50%) with deposit layer height exceeding ~ 1 mm
5	Large amounts of deposition on blade surfaces (more than 50% of the blades were affected), film deposition all over the blade platform and overall engine performance was significantly reduced during the run

Table 8-3 Engine damage level key

The images of deposition shown in Figure 8-2, Figure 8-3, Figure 8-4 and Figure 8-5 were obtained using the borescope, when the engine was run at 120,000 RPM. In all cases, there was no deposition on the rotor blades and the images shown are of the nozzle guide vanes and the adjoining blade platform, both of which were uncoated and made of Inconel alloy. They are organised in increasing order of damage level to the engine (1 being the lowest and 5 the most severe).

Figure 8-2 shows images taken after run A (fine VA, with a total of 20 g injected). The sample of VA injected in this case had an average particle size of ~ 20 μm. Small amounts of VA have deposited (a) on the leading edge of the blades, and (b) as a thin layer on the adjoining blade platform. Deposition on the leading edge was only observed on one or two vanes (out of a total of 22). This was classified as damage level 1.

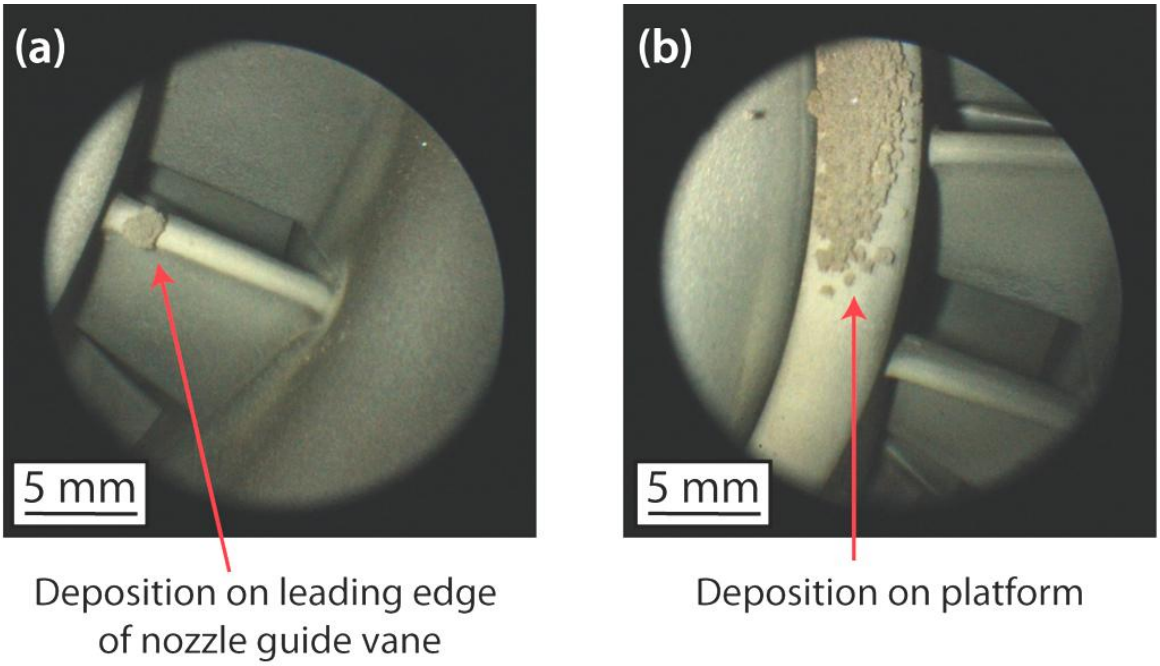

Figure 8-2 Run A (fine VA, total of 20 g injected) borescope images. Small amounts of VA have deposited (a) on the leading edge of the vanes, and (b) a small area of thin layer deposition is observed on the blade platform. (damage level 1)

Figure 8-3 shows images taken after run D (medium 1 VA, with a total of 20 g injected). The sample of VA injected in this case had an average particle size of ~ 50 µm. More pronounced lumps of VA have deposited (a) on the leading edge of the vanes and (b) a similar coverage of thin layer deposition was observed on the blade platform. This was classified as damage level 2. Compared to damage level 1, the height of the deposit lumps were more pronounced, although it was still restricted to a few locations (two or three vanes). It is noticeable that, particularly from Figure 8-3 (a), once adhesion of a significant amount of VA has taken place, further deposition seems to build up in the same locations, i.e. the prior presence of adhered particles promotes further adhesion [216, 223, 225]. This can be explained in terms of increased surface roughness (and possibly substrate temperature, by creating local hot spots), which raises the likelihood of particle impact leading to adhesion.

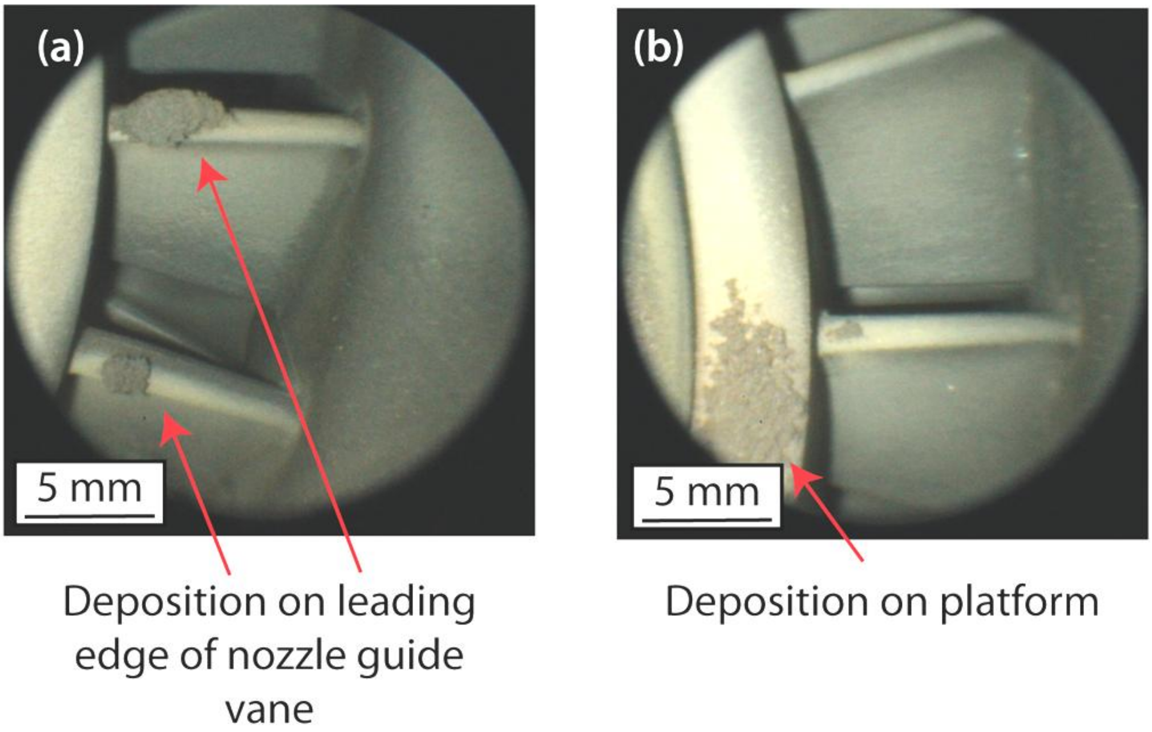

Figure 8-3 Run D (medium 1 VA, total of 20g injected) borescope images. More pronounced lumps of VA have deposited (a) on the leading edge of 2 – 3 vanes and (b) similar coverage of thin layer deposition observed on the adjoining platform. (damage level 2)

Figure 8-4 relates to run E (medium 2 VA, total of 30 g injected). The sample of VA injected in this case had an average particle size of ~ 75 µm and the observed damage was classified as level 3. It can be seen that deposition is now more substantial, and extends to a larger proportion of the available surface, demonstrating that coarser particles deposit more effectively, and that deposition is indeed progressive. The discolouration of the leading edge and suction side of the blades also indicates heavy abrasion. This observation supports the conjecture that larger particles are more likely to impact surfaces and a larger fraction of it are also more likely to be too cold to deposit, hence contribute more to erosive effects. However, more powder was injected in run E compared to previous runs A and D.

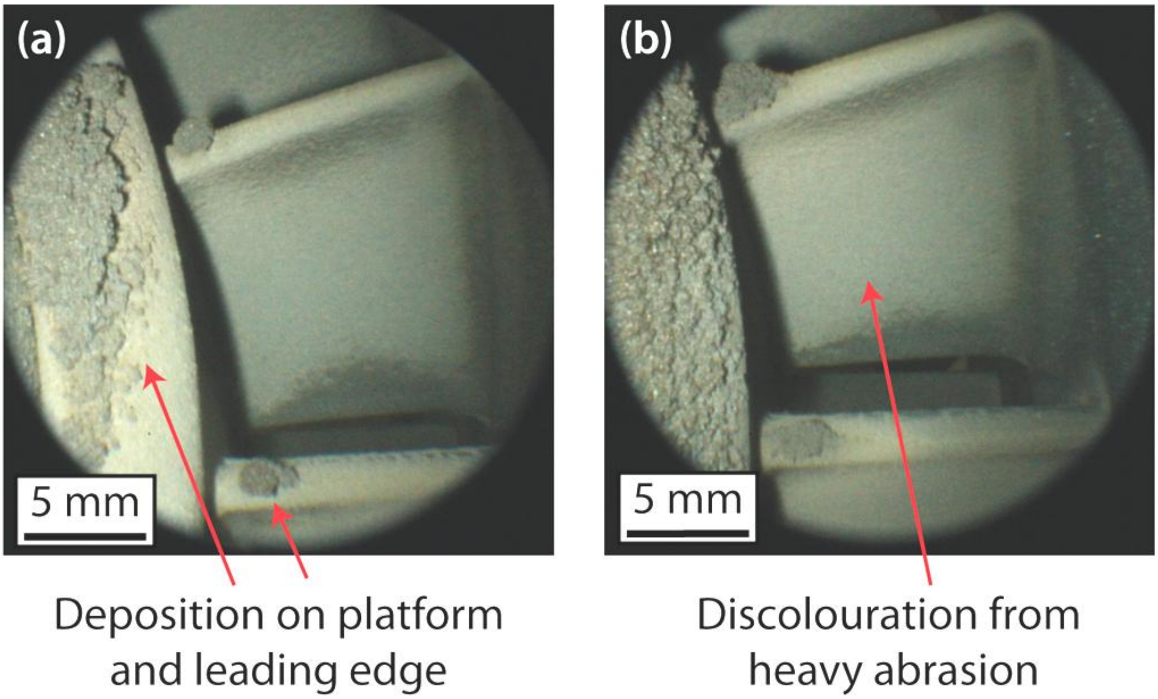

Figure 8-4 Run E (medium 2 VA, total of 30 g injected) borescope images. (a) Larger lumps and larger area of deposition were observed, both on the blades and the platform. (b) More pronounced signs of erosion (seen from the discolouration) on the leading edge and suction side of the blades. (damage level 3)

Finally, Figure 8-5 relates to run G (coarse VA, total of 30 g injected). The sample of VA injected in this case had an average particle size of ~ 100 μm, which was the coarsest specimen. The observed damage was classified as level 4. Deposition layer was seen all along the blade platform (covering more than 50% of the exposed area) and large lumps of deposition was observed on a few vanes. Again, extensive erosive damage was observed all along the leading edge and across entire surface of the suction side of the blades. Approximately the same amount of powder was injected as run E, demonstrating the strong effect of average particle size on the level of adhesion.

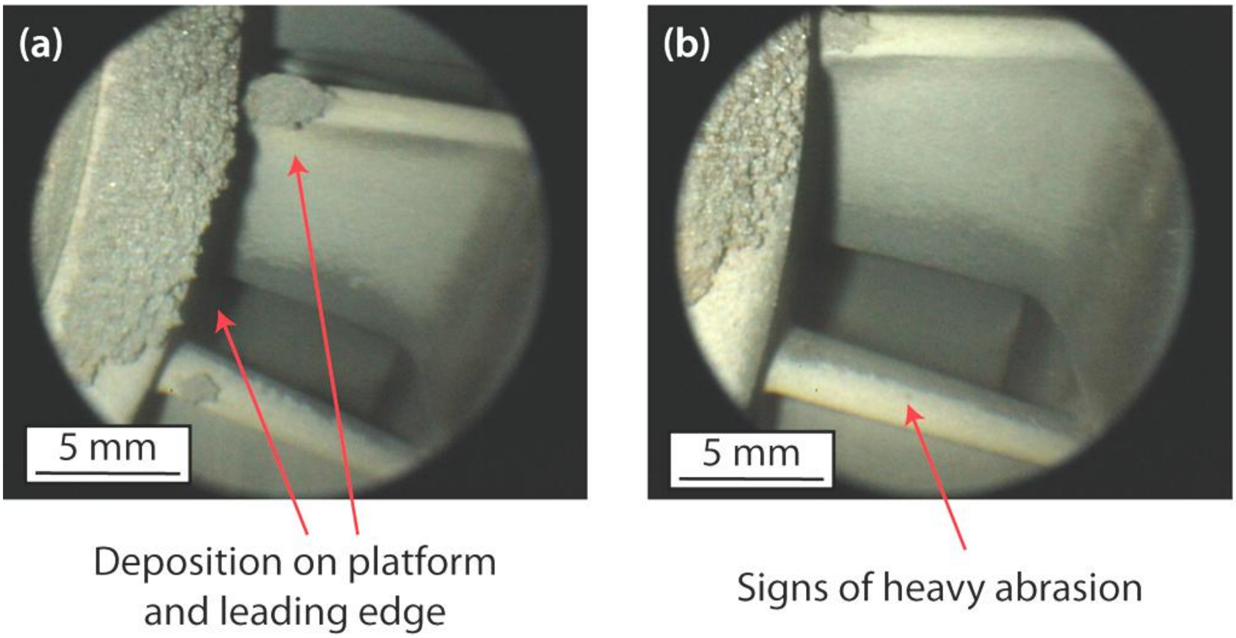

Figure 8-5 Run G (coarse VA, total of 30 g injected) borescope images. (a) Deposition layer seen all along the blade platform, covering more than 50% of the exposed area, and some large lumps on the blade leading edges. (b) Extensive blade erosion seen on leading edge and suction side of vanes. (damage level 4)

The observed deposition behaviour and damage characteristics exhibited are summarised in Figure 8-6, which basically indicates that more extensive deposition occurred with the coarser particles. In all cases, the deposition was progressive with continued injection of powder, i.e. the more powder was injected (for a certain particle size), the more deposition tended to take place.

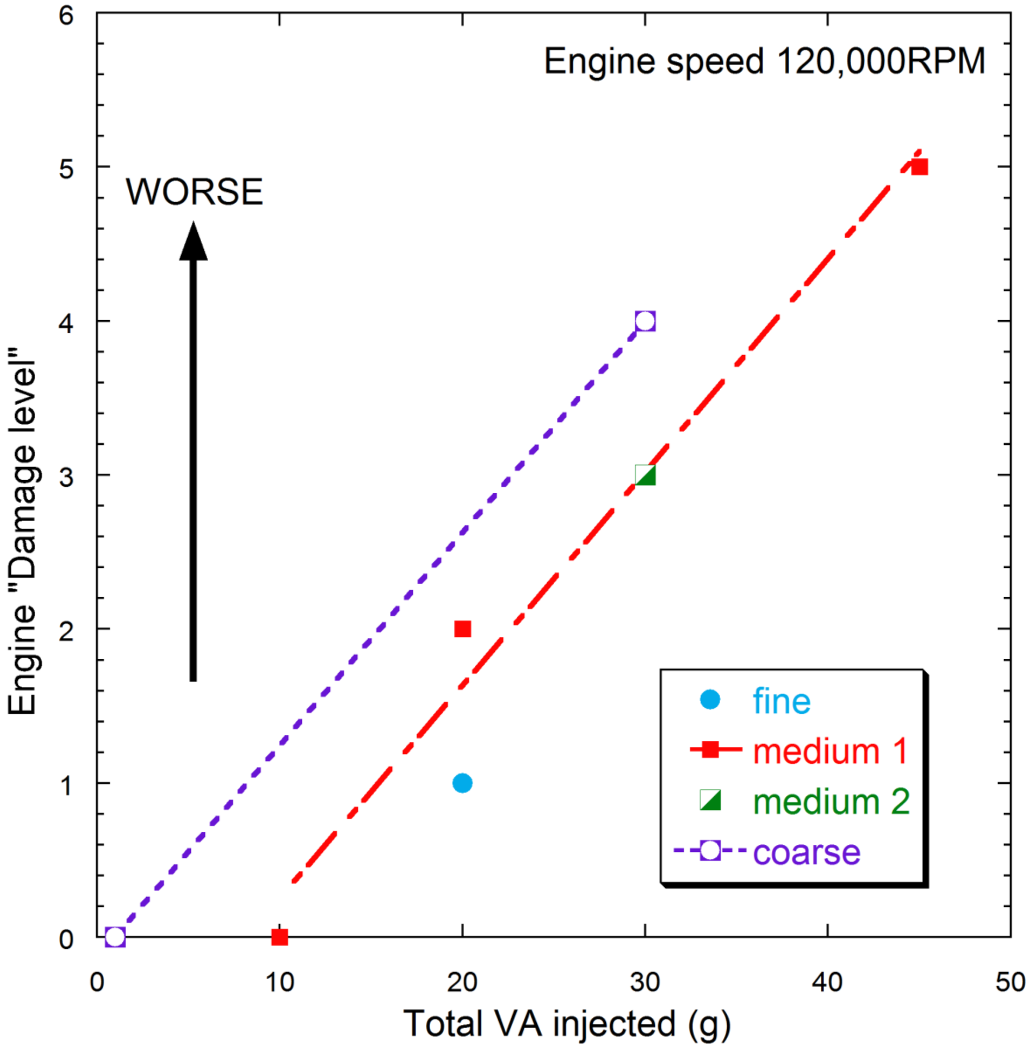

Figure 8-6 Damage level index as a function of the total amount of VA injected, for the four particle sizes, with an engine speed of 120,000 RPM.

8.2.2 Correlation with Modelled Particle Acceleration and Heating

Predicted particle displacement and thermal histories (for an engine speed of 120,000 RPM) are shown in Figure 8-7 and Figure 8-8, for all four particle sizes. Assuming a flight distance (combustion chamber length) of 100 mm, the time of flight and the particle temperature at the end of flight are shown in Table 8-4, for each particle size. Several features are apparent from these predictions. Firstly, as expected, smaller particles become appreciably hotter during flight. The fine particles reach temperatures fairly close to the gas combustion temperature (1070°C) by the time they enter the turbine (after about 0.7 ms), whereas the coarsest particle (100 μm) have only reached about 400°C by that point, despite the fact that its flight takes almost twice as long (1.3 ms). Of course, it may be noted that while 1070°C is well above T_g (~ 600°C), and close to the melting temperature, 400°C is appreciably below T_g. Therefore, whilst the fine particles are basically molten, the coarse particle is solid just before the point of impact. Secondly, the velocity of the finest particles at that point (226 m s^{-1}) is considerably higher than that of the coarsest particles (137 m s^{-1}).

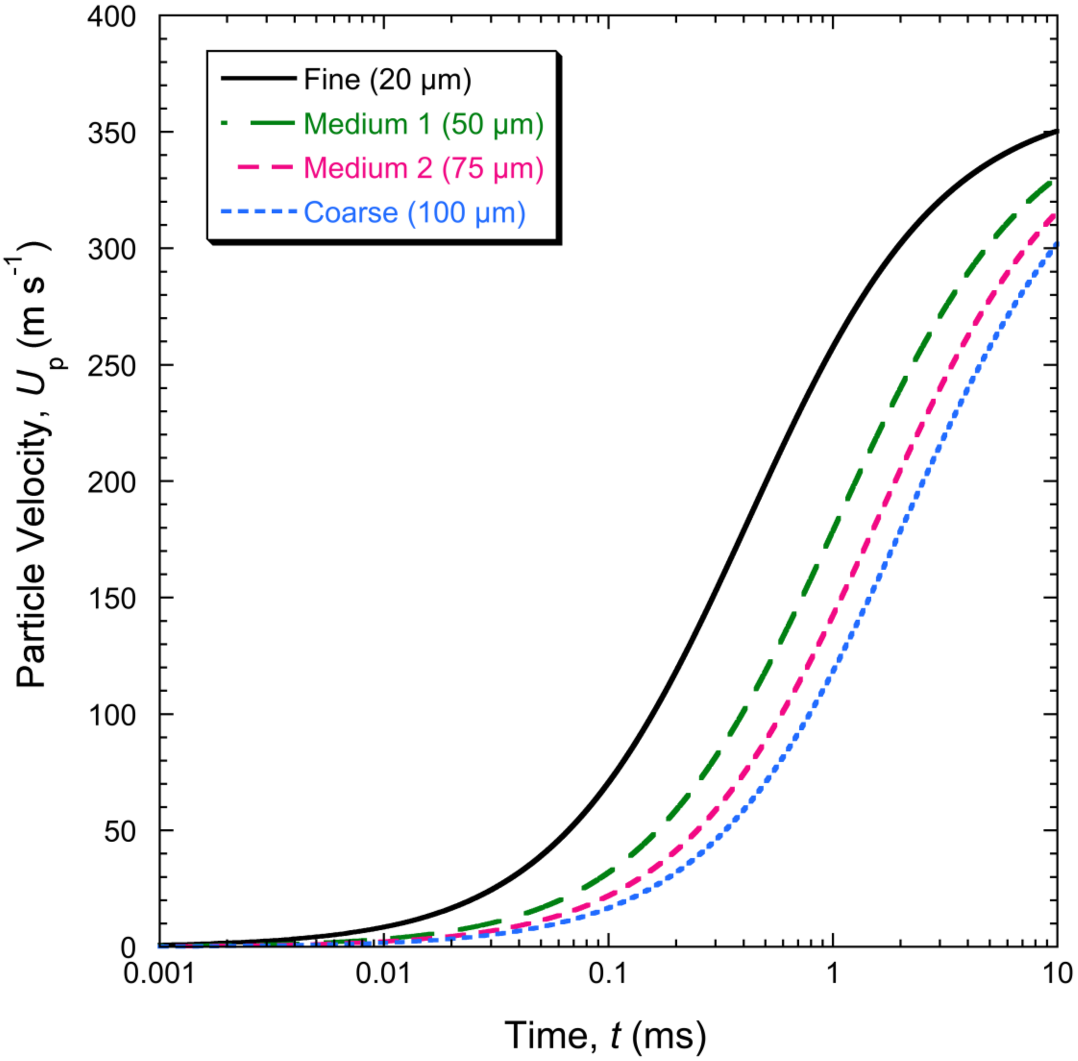

Figure 8-7 Predicted particle velocity as a function of time, for a free stream velocity of 365 m s^{-1} (which is the estimated jet speed for an engine speed of 120,000 RPM).

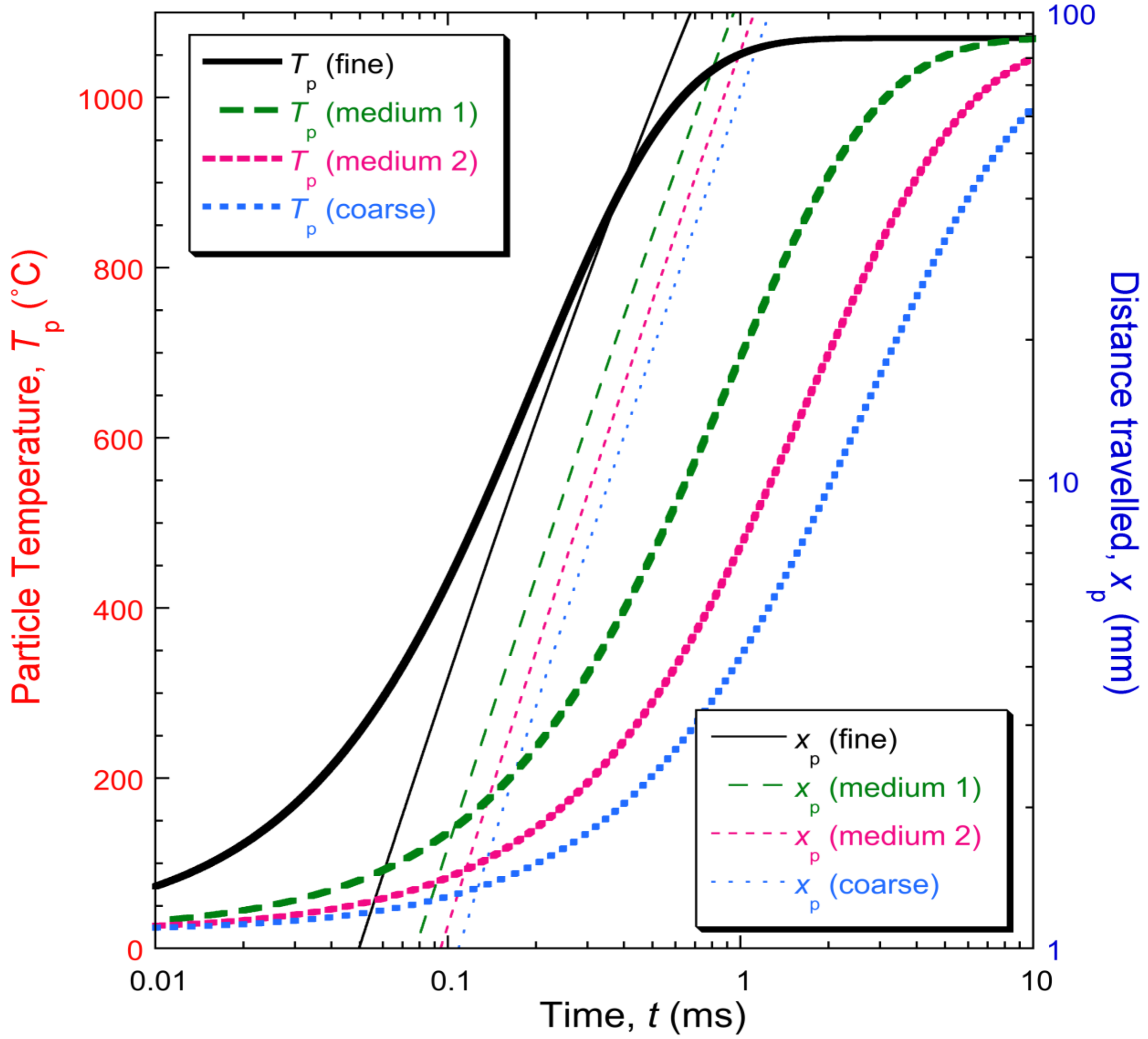

Figure 8-8 Predicted particle temperature and displacement as a function of time, for a free stream velocity of 365 m s^{-1} and a far field temperature of 1070°C (these are estimated values for the jet speed and turbine entry temperature for an engine speed of 120,000 RPM).

D_p	Time of flight (ms)	U_p at end of flight (m s^{-1})	T_p at end of flight (°C)
Fine (~ 20 μm)	0.68	226	1011
Medium 1 (~ 50 μm)	0.95	174	677
Medium 2 (~ 75 μm)	1.12	152	507
Coarse (~ 100 μm)	1.26	137	403

Table 8-4 Calculated time of flight values (assuming 100 mm long combustion chamber), and corresponding particle speed and temperatures (for an engine speed 120,000 RPM).

Now these modelling outcomes should be considered in relation to the observation made that coarser particles more readily adhere than the finer ones. Two points should be highlighted. Firstly, particle size has a strong influence on the particle inertia. Finer particles tend to follow gas streamlines, whereas larger ones may have sufficient inertia to ensure that they do not deflect with the gas flow when its direction changes sharply. The gas flow would, for example, turn rapidly as it flows past the nozzle guide vanes and the adjoining blade platform. Only when particles are not readily carried with the gas stream would they be likely to strike a component surface, and it seems that the fine particles in these experiments did not do this. In other words, they would rapidly accelerate to match the gas stream velocity and then subsequently be carried straight through the engine. The calculated values for the Stokes number for all particle sizes tabulated below supports this idea:

D_p	Stk
Fine (~ 20 μm)	44
Medium 1 (~ 50 μm)	277
Medium 2 (~ 75 μm)	622
Coarse (~ 100 μm)	1106

Table 5 Calculated values for the particle Stokes number

Secondly, while the coarse particles are predicted to be relatively cold on impact (400°C), the temperature of the stationary surfaces concerned (nozzle guide vanes and the platform) are expected to be well above this level. Since the turbine entry temperature of the gas is estimated to be above 1000°C, the stationary surface temperature may indeed be above the T_g of the VA (~ 600°C), in which case the particles may soften immediately upon impact, which makes spreading and subsequent adhesion highly probable. Of course, in order to predict rigorously whether adhesion is expected, it would be necessary to model the impact and spreading phenomena, including the associated heat transfer between the particle and the hot surface. However, in general it seems plausible to suggest that particles of around 50 – 100 μm are moving fast enough, and have sufficient inertia, to strike these substrates on entering the turbine and that, when they do, their temperature, and that of the substrate, taking into account the (relatively low) T_g value of this particular VA, are such that they soften sufficiently to spread and adhere on impact.

8.3 Section Summary

The following conclusions can be drawn from this chapter.

a) A small gas turbine engine has been used in order to investigate the deposition behaviour of ingested volcanic ash (VA) powder. There are virtually no reports in the open literature where such an experimental set-up (using a real gas turbine engine) has been employed. Therefore, there is considerable interest in quantifying the factors which affect the likelihood of ingested particles adhering to internal surfaces, since it is clear that adhesion can rapidly lead to severe degradation (as discussed previously in

Chapter 7.0) and may substantially affect component longevity. Two engine speeds (62,000 RPM and 120,000 RPM) and four different particle size distributions of VA particles were used in the experiments, with average particle diameters of around 20 μm, 50 μm, 75 μm and 100 μm. The VA powder had an approximate T_g value of around 600°C. This sample of VA was also found to have a substantial amorphous content of ~ 80 – 90% (as is commonly found in naturally occurring volcanic ash).

b) No deposition was observed when the engine was run at the lower engine speed. There was also no deposition observed in any run on the rotating turbine blade surfaces. However, significant deposition on stationary surfaces (nozzle guide vanes and adjoining blade platform) was seen in several cases with the engine at full power. It was noticeable that the coarser the particles (and the more particles were fed through), the more deposition took place.

c) A simple numerical model was used to predict particle displacement and thermal histories within the combustion chamber. It was thus possible to predict the time of flight and the particle temperature upon entry to the turbine section. At full power, the gas turbine entry temperature was estimated to be about 1070°C. Fine particles (~ 20 μm) were predicted to practically reach this temperature after flight through the combustion chamber, which takes less than 1 ms. The relatively limited deposition observed with the fine particles is mainly attributed to their low inertia, which means they tend to be carried with the gas streamline (without impacting any surfaces), even if it were to rapidly turn. These particles are predicted to be travelling at about 200 – 250 m s^{-1} as they enter the turbine, with the surrounding gas stream velocity estimated to be about 350 m s^{-1}. No systematic modelling has been attempted of the expected trajectories such particles will follow when the gas stream deviates around obstacles, but their Stokes number is estimated to be relatively low, suggesting that they will tend to follow the streamlines and hence avoid impact with solid surfaces.

d) Larger particles (~ 100 μm) are predicted to be no hotter than about 400°C, which is below T_g, upon entry to the turbine. However, it appears likely that their relatively large inertia leads to a high probability of them striking solid surfaces within the turbine. In addition, these stationary surfaces are likely to be well above T_g as a result of heating by the gas stream, and therefore it is likely that the particles tend to become soft enough to spread and adhere on impact. One would expect that particles much larger than this (e.g. ~ 200 μm) would be much too cold on impact for this to occur, but the present experimental work has been limited to particles of up to around 100 μm diameter.

e) While these experimental observations are qualitative, and the model used is crude, the results appear to be consistent and to give at least some insights into the main deposition phenomena involved. The main conclusion is that VA of this type, which often has a relatively low T_g and a large amorphous content, can exhibit a marked tendency to adhere to stationary components within the turbine, particularly at full engine power and when the particles are relatively large. Since it is already established that such adhering of VA can have highly deleterious effects within a turbine, on both short and longer timescales, this is clearly an issue of concern, particularly regarding the lifetime of thermal barrier coatings. This work highlights the importance of characterising the physical properties of VA (notably the particle size distribution, T_g and its amorphous content) as a practical measure in assessing the kind of damage it may cause if ingested in substantial quantities.

9.0 Conclusions

- **A simple methodology for the prediction of (sintering-induced) spallation lifetimes of PS YSZ TBCs was outlined**

This spallation criterion is simply that, if the strain energy release rate associated with debonding reaches a critical value (i.e. the interfacial fracture toughness), then spallation is energetically favourable. Experiments were designed so that spallation was driven solely by a thermal misfit strain, associated with rapid cooling from a stress-free upper temperature. This misfit strain was assumed to be accommodated entirely by the coating, which is reasonable, since the alumina substrate employed in this work is much thicker and stiffer. The experimental set up was such that rapid cooling was achieved by gas quenching, hence it was reasonable to assume that the coating response would be predominantly elastic. The use of an alumina substrate meant that effects arising from changes in the coating/substrate interface (such as the development of a TGO) could be avoided. In addition, specimens could be isothermally heat treated, so complications that may arise from the presence of a thermal gradient were avoided.

Experimental data were obtained for the change in coating stiffness as a function of temperature (1400°C and 1500°C). Spallation lifetime data were obtained at 1500°C, using a computer controlled system with a periodic quenching capability. A strong correlation between lifetime and coating thickness was established, which was expected, since the stored elastic strain energy (the driving force for spallation) is proportional to coating thickness. Measured spallation lifetimes (with appropriate corrections being made for edge effects and the presence of segmentation cracks) were consistent with constant interfacial fracture energy of approximately 300 J m^{-2}.

- **This global fracture mechanics based methodology is also applicable to conventional TBC systems**

There are, of course, a few obvious differences between conditions created in this study and real life gas turbine systems. For example, the interfacial region is often not chemically stable in a real system, due to bond coat oxidation and interdiffusion of alloying species. However, if one were able to ascertain how this morphological and chemical change to the interface (with exposure to high temperature) is reflected in the value of the fracture energy, combined with the effects of coating sintering, then the rationale presented here may be used for prediction of coating lifetime. This work also highlights the practical importance of monitoring stiffness of coatings in service (as a degradation indicator), which may be implemented relatively easily. The stiffness may, of course, also be drastically altered by adhesion and ingression of glassy deposits of foreign ingested particulates or CMAS (calcia-magnesia-alumina-silica compounds), such as sand and volcanic ash.

- **The effects of two types of CMAS (vermiculite and volcanic ash) on the sintering behaviour of PS TBCs were investigated**

Surface additions of CMAS on PS TBCs, either free-standing or attached to an alumina substrate, was made and were subject to heat treatments in the temperature range 1200°C – 1500°C. It was found that molten vermiculite (VM) and volcanic ash (VA) penetrate rapidly into the coating, at least initially, by viscous flow. A heavily liquid infiltrated layer is initially formed, followed by diffusion, mainly via the grain boundaries. It was found that, similarly to reports found in literature, the presence of VM at high temperature promotes formation of the monoclinic phase. This is caused by dissolution of the zirconia grains into the silica-rich amorphous phase (which results in yttria being leached out of the zirconia). The yttria-lean zirconia is subsequently reprecipitated out upon cooling, in the characteristic spherodized form, as monoclinic zirconia. The ingression of VM and VA was observed to accelerate the sintering behaviour, and this was demonstrated by enhanced coating stiffening and shrinkage. Understanding the complex thermochemical reactions between CMAS and YSZ is an essential aid to developing alternative coating compositions, designed to mitigate CMAS-induced degradation.

- **The effect of CMAS on the spallation lifetime of PS TBCs were investigated**

As a consequence of enhanced sintering, and hence stiffening of the TBC, it has been shown (using the periodic quenching furnace) that even small additions of CMAS (a few ~ wt.%) may compromise the thermomechanical stability of the YSZ coatings. This result highlights the fact that, whilst low level exposure may not cause immediate catastrophic damage to TBC performance, it will nonetheless affect component longevity by accelerating the sintering-induced stiffening. This study has concentrated on the sintering behaviour and spallation lifetime of PS TBCs (with or without CMAS), but the same conclusions should, in principle, apply to EB-PVD coatings. However, it is important to note that this type of TBC damage (CMAS-induced sintering) can only occur if particulates do sufficiently impinge on TBC surfaces and subsequently deposit, at significant levels. It is therefore also important to study the parameters which affect the deposition behaviour of CMAS on turbine internal surfaces, in order to assess the scale of the overall damage caused.

- **A small gas turbine engine was used to investigate the deposition behaviour of ingested volcanic ash**

A small gas turbine engine has been used in order to investigate the deposition behaviour of ingested volcanic ash (VA) powder. There are virtually no reports in the open literature where such an experimental set-up, using a real gas turbine engine, has been employed. Therefore, there is considerable interest in quantifying the factors which affect the likelihood of ingested particles adhering to internal surfaces, since it is clear that adhesion can rapidly lead to severe degradation and may substantially affect component longevity. Two engine speeds and four different particle size distributions of VA particles were used in the experiments, with average particle diameters of around 20 μm, 50 μm, 75 μm and 100 μm. The VA powder had an approximate T_g value of around 600°C. Although this sample of VA was found to have a substantial amorphous content of ~ 80 – 90% (as is commonly found in volcanic ash), a melting temperature of around 1100°C was also evaluated by DSC. The main conclusion is that VA of this type can exhibit a marked tendency to adhere to stationary components within the turbine, particularly at full engine power and when the particles are relatively large. In other words, larger particles (with greater inertia) in hotter gas (at full engine speed) stick better to hotter surfaces (stationary components). The deposition behaviour was also observed to be progressive i.e. particles are more likely to stick to where deposition has already taken place. This is due to the increased surface roughness and possible hot spots created in deposited areas.

- **Comparison with numerical modelling results show that the characterisation of the physical properties of the volcanic ash, in order to assess likelihood of adhesion, is of practical importance**

A simple numerical model has been used to predict particle acceleration and heating in flight. It was observed and predicted that relatively large particles (~ 100 μm) are more likely to adhere than smaller ones, because they have greater inertia, and thus are more likely to deflect away from gas streamline and impact a turbine surface. The temperature of the larger particles at the end of its flight was predicted to be below its softening point. However, since the stationary component surface temperatures are expected to be at least as hot as, and perhaps hotter than, the particles themselves, adhesion of such particles is apparently probable, by melting/softening straight after impact. Particles larger than around 100 μm would probably not adhere, since they would be much too cold, but also the ingestion of such large particulates is not very likely. This work highlights the importance of characterising the physical properties of VA (notably the particle size distribution, T_g and its amorphous content) as a practical measure in assessing the kind of damage it may cause if ingested in substantial quantities.

10.0 Future Work

In this study, the effect of sintering-induced stiffening on the spallation behaviour of PS YSZ TBCs, deposited on alumina substrates, was investigated. Of course, in real life systems, the interfacial region undergoes microstructural changes during service, such as the formation of a TGO. In order to predict spallation lifetimes of conventional systems of TBCs on a metallic substrate, independently measuring the change in fracture energy with the growth of the TGO would be the next logical step. In addition, it would be of interest to see how the formation of segmentation cracks affect TGO growth. One would expect that growth would occur preferentially near the root of deep segmentation cracks, where oxygen and corrosive elements may easily reach the metallic interface. How the TGO growth may be affected by contact with CMAS species (if they ingress far enough to reach the interface at sufficient quantities), would also be of interest. It was found in this work that segmentation cracks, once formed, tended to persist, even when exposed to hundreds of hours at very high temperature (~ 1500°C). How the formation and persistence of segmentation cracks may be affected by the presence of CMAS is also of interest (i.e. whether CMAS aids or discourages crack healing by segregating at free surfaces).

Improved understanding of the mechanism of CMAS penetration into YSZ coatings is required, with particular focus on the effect of TBC pore architecture and also the chemical composition of CMAS (which affects its glass transition, amorphous fraction and crystalline melting point). If one could identify the type of pore architecture which resists CMAS penetration, this would be valuable information for the development of TBCs which are more resistant to CMAS attack. The mechanism of penetration will affect the nature of the thermo-chemical interactions between the CMAS glass and TBC material, which will also aid the search for novel coating formulations.

Finally, better understanding of the adhesion behaviour of impinging particulates on turbine surfaces is required. In particular, the modelling of the spreading of softened particulates straight after impact should be looked at in further detail. Such modelling should include the effects of substrate temperature (and also perhaps its topography) and the appropriate heat transfer parameters. In addition, inertial effects of whether particles follow the gas streamline or not, should be incorporated into the particle acceleration model. This may provide a threshold particle diameter, below which particles are not expected to hit turbine surfaces by inertial impaction. All such information would contribute to the refinement of guidelines for safe ingestion limits for both the aviation and power generation industry.

References

[1] B. Gleeson, "Thermal barrier coatings for aeroengine applications," *Journal of Propulsion and Power,* vol. 22, pp. 375-383, Mar-Apr 2006.

[2] D. R. Clarke, "Materials Selection Guidelines for Low Thermal Conductivity Barrier Coatings," *Surface and Coatings Technology,* vol. 163-164, pp. 67-74, 2003.

[3] D. R. Clarke and C. G. Levi, "Materials Design for the Next Generation Thermal Barrier Coatings," *Annual Review of Materials Research,* vol. 33, pp. 383-417, 2003.

[4] D. R. Clarke, C. G. Levi, and A. G. Evans, "Enhanced zirconia thermal barrier coating systems," *Proceedings of the Institution of Mechanical Engineers Part a-Journal of Power and Energy,* vol. 220, pp. 85-92, Feb 2006.

[5] N. P. Padture, M. Gell, and E. H. Jordan. (2002) Thermal Barrier Coatings for Gas Turbine Engine Applications. *Science*. 280-284.

[6] M. Peters, C. Leyens, U. Schulz, and W. A. Kaysser, "EB-PVD Thermal Barrier Coatings for Aeroengines and Gas Turbines," *Advanced Engineering Materials,* vol. 3, pp. 193-204, 2001.

[7] J. T. DeMasi-Marcin and D. K. Gupta, "Protective Coatings in the Gas Turbine Engine," *Surface and Coatings Technology,* vol. 68/69, pp. 1-9, 1994.

[8] U. Schulz, C. Leyens, K. Fritscher, M. Peters, B. Saruhan-Brings, O. Lavigne, J.-M. Dorvaux, M. Poulain, R. Mevrel, and M. Caliez, "Some Recent Trends in Research and Technology of Advanced Thermal Barrier Coatings," *Aerospace Science and Technology,* vol. 7, pp. 73-80, 2003.

[9] D. R. Clarke, M. Oechsner, and N. P. Padture, "Thermal-barrier coatings for more efficient gas-turbine engines," *MRS Bulletin,* vol. 37, pp. 891-898, 2012.

[10] A. G. Evans, D. R. Mumm, J. W. Hutchinson, G. H. Meier, and F. S. Pettit, "Mechanisms controlling the Durability of Thermal Barrier Coatings," *Progress in Materials Science,* vol. 46, pp. 505-553, 2001.

[11] A. C. Fox and T. W. Clyne, "Oxygen Transport through the Zirconia Layer in Plasma Sprayed Thermal Barrier Coatings," *Surface and Coatings Technology,* vol. 184, pp. 311-321, 2004.

[12] X. Q. Cao, R. Vassen, and D. Stoever, "Ceramic Materials for Thermal Barrier Coatings," *Journal of the European Ceramic Society,* vol. 24, pp. 1-10, 2004.

[13] S. Paul, A. Cipitria, S. A. Tsipas, and T. W. Clyne, "Sintering Characteristics of Plasma Sprayed Zirconia Coatings containing

different Stabilisers," *Surface and Coatings Technology,* vol. 203, pp. 1069-1074, 2009.
[14] C. G. Levi, "Emerging Materials and Processes for Thermal Barrier Systems," *Current Opinion in Solid State & Materials Science,* vol. 8, pp. 77-91, 2004.
[15] S. Stecura, "New ZrO2-Yb2O3 Plasma-Sprayed Coatings for Thermal Barrier Applications," *Thin Solid Films,* vol. 150, pp. 15-40, 1987.
[16] J. Matejicek, C. Sampath, P. C. Brand, and H. J. Prask, "Quenching, Thermal and Residual Stress in Plasma Sprayed Deposits: NiCrAlY and YSZ Coatings," *Acta Materialia,* vol. 47, pp. 607-617, 1999.
[17] M. A. Helminiak, N. M. Yanar, F. S. Pettit, T. A. Taylor, and G. H. Meier, "The behavior of high-purity , low-density air plasma sprayed thermal barrier coatings," *Surface and Coatings Technology,* vol. 204, pp. 793-796, 2009.
[18] V. K. Tolpygo, K. S. Murphy, and D. R. Clarke, "Effect of Hf, Y and C in the underlying superalloy on the rumpling of diffusion aluminide coatings," *Acta Materialia,* vol. 56, pp. 489-499, 2008.
[19] W. Chi, S. Sampath, and H. Wang, "Microstructure–thermal conductivity relationships for plasma-sprayed yttria-stabilized zirconia coatings," *Journal of American Ceramic Society,* vol. 91, pp. 2636-2645, 2008.
[20] D. D. Hass, A. J. Slifka, and H. N. G. Wadley, "Low Thermal conductivity Vapor Deposited Zirconia Microstructures," *Acta Materialia,* vol. 49, pp. 973-983, 2001.
[21] A. G. Evans, D. R. Clarke, and C. G. Levi, "The influence of oxides on the performance of advanced gas turbines," *Journal of the European Ceramic Society,* vol. 28, pp. 1405-1419, 2008.
[22] C. Mercer, J. R. Williams, D. R. Clarke, and A. G. Evans, "On a ferroelastic mechanism governing the toughness of metastable tetragonal-prime (t′) yttria-stabilized zirconia," *Proceedings of the Royal Society A: Mathematical, Physical and Engineering Science,* vol. 463, pp. 1393-1408, 2007.
[23] A. V. Virkar and R. L. K. Matsumoto, "Ferroelastic Domain Switching as a Toughening Mechanism in Tetragonal Zirconia," *Journal of the American Ceramic Society,* vol. 69, pp. C-224-C-226, 1986.
[24] E. M. Donohue, N. R. Philips, M. R. Begley, and C. G. Levi, "Thermal barrier coating toughness: Measurement and identification of a bridging mechanism enabled by segmented microstructure," *Materials Science and Engineering: A,* vol. 564, pp. 324-330, 2013.
[25] T. Xu, S. Faulhaber, C. Mercer, M. Maloney, and A. Evans, "Observations and analyses of failure mechanisms in thermal barrier

systems with two phase bond coats based on NiCoCrAlY," *Acta Materialia,* vol. 52, pp. 1439-1450, 2004.

[26] N. S. Bornstein, M. A. Decrescente, and J. G. Smeggil, "The influence of sulfur on the oxidation of coatings," *Materials Science and Engineering A,* vol. 120, pp. 175-178, 1989.

[27] Y. Ikeda, M. Tosa, K. Yoshihara, and K. Nii, "Adherence of Al2O3 Coating Layers to Steels: The Detrimental Effect of Sulphur and the Beneficial Effect of Rare Metals," *Materials Science and Engineering A,* vol. 120, pp. 179-184, 1989.

[28] J. L. Smialek, "Maintaining Adhesion of Protective Al_2O_3 Scales," *JOM,* vol. 52, pp. 22-25(4), 2000.

[29] I. G. Wright and B. A. Pint, "Bond coating issues in thermal barrier coatings for industrial gas turbines," *Journal of Power and Energy,* vol. 219 Part A, pp. 101-107, 2005.

[30] H. M. Tawancy and L. M. Al-hadhrami, "Role of Platinum in Thermal Barrier Coatings Used in Gas Turbine Blade Applications," *Journal of Engineering for Gas Turbines and Power,* vol. 132, pp. 1-6, 2010.

[31] K. A. Marino and E. A. Carter, "The effect of platinum on Al diffusion kinetics in b-NiAl : Implications for thermal barrier coating lifetime," *Acta Materialia,* vol. 58, pp. 2726-2737, 2010.

[32] H. E. Evans and M. P. Taylor, "Oxidation of high-temperature coatings," *Aerospace Engineering,* vol. 220, pp. 1-10, 2006.

[33] T. M. Pollock, D. M. Lipkin, and K. J. Hemker, "Multifunctional coating interlayers for thermal-barrier systems," *MRS Bulletin,* vol. 37, pp. 923-931, 2012.

[34] D. D. Hass, "Directed Vapour Deposition of Thermal Barrier Coatings," Ph. D., Department of Materials Science and Engineering, University of Virginia, Charlottesville, 2000.

[35] I. Sevostianov and M. Kachanov, "Elastic and conductive properties of plasma-sprayed ceramic coatings in relation to their microstructure : An overview," *Journal of Thermal Spray Technology,* vol. 18 (5-6), pp. 822-834, 2009 2009.

[36] S. H. Leigh and C. C. Berndt, "Quantitative Evaluation of Void Distributions Within a Plasma-Sprayed Ceramic," *Journal of the American Ceramic Society,* vol. 82, pp. 17-21, 1999.

[37] T. W. Clyne, I. O. Golosnoy, J. C. Tan, and A. E. Markaki, "Porous Materials for Thermal Management under Extreme Conditions," *Philosophical Transactions of the Royal Society A - Mathematical Physical and Engineering Sciences,* vol. 364, pp. 125-146, Jan 2006.

[38] K. von Niessen and M. Gindrat, "Vapor Phase Deposition Using a Plasma Spray Process," *Journal of Engineering for Gas Turbines and Power,* vol. 133, pp. 061301-7, 2011.

[39] U. Schulz, B. Saruhan, K. Fritscher, and C. Leyens, "Review on Advanced EB-PVD Ceramic Topcoats for TBC Applications," *International Journal of Applied Ceramic Technology,* vol. 1, pp. 302-315, 2004.

[40] D. D. Hass, P. A. Parrish, and H. N. G. Wadley, "Electron beam directed vapor deposition of thermal barrier coatings," *Journal of Vacuum Science and Technology A: Vacuum, Surfaces and Films,* vol. 16, pp. 3396-3401, 1998.

[41] A. Shinozawa, K. Eguchi, M. Kambara, and T. Yoshida, "Feather-like structured YSZ coatings at fast rates by plasma spray physical vapor deposition," *Journal of Thermal Spray Technology,* vol. 19, pp. 190-197, 2010.

[42] P. Fauchais and G. Montavon, "Latest Developments in Suspension and Liquid Precursor Thermal Spraying," *Journal of Thermal Spray Technology,* vol. 19, pp. 226-239, 2010.

[43] M. Gell, L. Xie, X. Ma, E. H. Jordan, and N. P. Padture, "Highly Durable Thermal Barrier Coatings made by the Solution Precursor Plasma Spray Process," *Surface and Coatings Technology,* vol. 177-178, pp. 97-102, 2004.

[44] M. Gell, E. H. Jordan, M. Teicholz, B. M. Cetegen, N. P. Padture, L. Xie, and D. Chen, "Thermal Barrier Coatings Made by the Solution Precursor Plasma Spray Process," *Journal of Thermal Spray Technology,* vol. 17, pp. 124-135, 2008.

[45] B. Zhou and K. Kokini, "Effect of pre-existing surface crack morphology on the interfacial thermal fracture of thermal barrier coatings: a numerical study," *Materials Science and Engineering: A,* vol. 348, pp. 271-279, 2003.

[46] X. L. Fan, R. Xu, W. X. Zhang, and T. J. Wang, "Effect of periodic surface cracks on the interfacial fracture of thermal barrier coating system," *Applied Surface Science,* vol. 258, pp. 9816-9823, 2012.

[47] C.-W. Wu, G.-N. Chen, K. Zhang, G.-X. Luo, and N.-G. Liang, "The effect of periodic segmentation cracks on the interfacial debonding: Study on interfacial stresses," *Surface and Coatings Technology,* vol. 201, pp. 287-291, 2006.

[48] G. W. Schulze and F. Erdogan, "Periodic cracking of elastic coatings," *International Journal of Solids and Structures,* vol. 35, pp. 3615-3634, 1998.

[49] A. Mézin, "An analytical solution for stress relaxation in cracked coatings," *Surface and Coatings Technology,* vol. 166, pp. 160-166, 2003.

[50] K. Kokini, A. Banurjee, and T. A. Taylor, "Thermal Fracture of Interfaces in Precracked Thermal Barrier Coatings," *Materials Science and Engineering,* vol. A323, pp. 70-82, 2002.

[51] N. P. Padture, K. W. Schlichting, T. Bhatia, A. Ozturk, B. Cetegen, E. H. Jordan, M. Gell, S. Jiang, T. D. Xiao, P. R. Strutt, E. Garcia, P. Miranzo, and M. I. Osendi, "Towards Durable Thermal Barrier Coatings with Novel Microstructures deposited by Solution-Precursor Plasma Spray," *Acta Materialia,* vol. 49, pp. 2251-2257, 2001.

[52] R. Vassen, A. Stuke, and D. Stöver, "Recent developments in the field of thermal barrier coatings," *Journal of Thermal Spray Technology,* vol. 18, pp. 181-186, 2009.

[53] A. Guignard, G. Mauer, R. Vaßen, and D. Stöver, "Deposition and characteristics of submicrometer-structured thermal barrier coatings by suspension plasma spraying," *Journal of Thermal Spray Technology,* vol. 21, pp. 416-424, 2012.

[54] T. W. Clyne and S. C. Gill, "Residual Stresses in Thermally Sprayed Coatings and their Effect on Interfacial Adhesion - A Review of Recent Work," *Journal of Thermal Spray Technology,* vol. 5, pp. 1-18, 1996.

[55] P. Scardi, M. Leoni, L. Bertini, and L. Bertamini, "Residual Stress in Partially-Stabilised Zirconia TBCs: Experimental Measurement and Modelling," *Surface and Coatings Technology,* vol. 94-5, pp. 82-88, 1997.

[56] R. Hamacha, B. Dionnet, A. Grimaud, and F. Nardou, "Residual Stress Evolution during the Thermal Cycling of Plasma-sprayed Zirconia Coatings," *Surface and Coatings Technology,* vol. 80, pp. 295-302, 1996.

[57] R. Elsing, O. Knotek, and U. Balting, "Calculation of Residual Thermal Stress in Plasma-Sprayed Coatings," *Surface and Coatings Technology,* vol. 43/44, pp. 416-425, 1990.

[58] O. Kesler, J. Matejicek, S. Sampath, S. Suresh, T. Gnaeupel-Herold, P. C. Brand, and H. J. Prask, "Measurement of Residual Stress in Plasma-Sprayed Metallic, Ceramic and Composite Coatings," *Materials Science and Engineering,* vol. A257, pp. 215-224, 1998.

[59] S. Kuroda, T. Fukushima, and S. Kitahara, "Quenching Stress in Plasma Sprayed Coatings and Its Correlation with the Deposit Microstructure," *Journal of Thermal Spray Technology,* vol. 4, pp. 75-84, 1995.

[60] P. Fauchais, "Understanding Plasma Spraying " *Journal of Physics D: Applied Physics,* vol. 37, pp. R86-R108, 2004.

[61] S. Kuroda and T. W. Clyne, "The Quenching Stress in Thermally Sprayed Coatings," *Thin Solid Films,* vol. 200, pp. 49-66, 1991.

[62] S. Kuroda, T. Fukushima, and S. Kitahara, "Generation Mechanisms of Residual-Stresses in Plasma-Sprayed Coatings," *Vacuum,* vol. 41, pp. 1297-1299, 1990.

[63] J. Brandon and R.Taylor, "Phase Stability of Zirconia-Based Thermal Barrier Coatings Part I. Zirconia-Yttria alloys," *Surface and Coatings Technology,* vol. 46, pp. 75-90, 1991.

[64] S. A. Tsipas, "Effect of dopants on the phase stability of zirconia-based plasma sprayed thermal barrier coatings," *Journal of the European Ceramic Society,* vol. 30, pp. 61-72, 2010.

[65] J. R. Brandon and R. Taylor, "Phase Stability of Zirconia-Based Thermal Barrier Coatings Part II. Zirconia-Ceria Alloys," *Surface & Coatings Technology,* vol. 46, pp. 91-101, 1991.

[66] S. Fabris, A. T. Paxton, and M. W. Finnis, "A stabilization mechanism of zirconia based on oxygen vacancies only," *Acta Materialia,* vol. 50, pp. 5171-5178, 2002.

[67] J. D. Ballard, J. Davenport, C. Lewis, W. Nelson, R. H. Doremus, and L. S. Schadler, "Phase Stability of Thermal Barrier Coatings Made From 8 wt.% Yttria Stabilized Zirconia: A Technical Note," *Journal of Thermal Spray Technology,* vol. 12 (1), pp. 34-37, 2003.

[68] J. Ilavsky, J. K. Stalick, and J. Wallace, "Thermal Spray yttria-Stabilized Zirconia Phase Changes during Annealing," *Journal of Thermal Spray Technology,* vol. 10, pp. 491-501, 2001.

[69] R. C. Garvie, R. H. J. Hannink, and R. T. Pascoe, "Ceramic Steel?," *Nature,* vol. 258, pp. 703-704, 1975.

[70] D. Zhu and D. A. Miller, "Development of Advanced Low Thermal Conductivity Thermal Barrier Coatings," *International Journal of Applied Ceramic Technology,* vol. 94, pp. 14-18, 2004.

[71] S. Raghavan, H. Wang, R. B. Dinwiddie, W. D. Porter, and M. J. Mayo, "The Effect of Grain Size, Porosity and Yttria Content on the Thermal Conductivity of Nanocrystalline Zirconia," *Scripta Materialia,* vol. 39, pp. 1119-1125, 1998.

[72] D. Zhu, J. A. Nesbitt, T. R. Mccue, C. A. Barrett, and R. A. Miller, "Furnace Cyclic Behavior of Plasma-Sprayed Zirconia-Yttria and Multi-Component Rare Earth Oxide Doped Thermal Barrier Coatings," *Ceramic Engineering and Science Proceedings,* vol. 23, pp. 533 -545, 2002.

[73] S. T. Aruna, N. Balaji, and K. S. Rajam, "Phase transformation and wear studies of plasma sprayed yttria stabilized zirconia coatings containing various mol% of yttria," *Materials Characterization,* vol. 62, pp. 697-705, 2011.

[74] R. G. Wellman and J. R. Nicholls, "A review of the erosion of thermal barrier coatings," *Journal of Physics D: Applied Physics,* vol. 40, pp. 293-305, 2007.

[75] A. H. Heuer, R. Chaim, and V. Lanteri, "The Displacive Cubic Tetragonal Transformation in ZrO_2 Alloys," *Acta Metallurgica,* vol. 35, pp. 661-666, 1987.

[76] H. G. Scott, "Phase Relationships in the ZrO_2-Y_2O_3 System," *Journal of Materials Science,* vol. 10, pp. 1527-1535, 1975.

[77] S. A. Tsipas, "Thermophysical Properties of Plasma Sprayed TBCs," PhD thesis, Department of Materials Science and Metallurgy, University of Cambridge, 2005.

[78] D. Baither, M. Bartsch, B. Baufeld, A. Tikhonovsky, A. Foitzik, M. Rühle, and U. Messerschmidt, "Ferroelastic and Plastic Deformation of t′ - Zirconia Single Crystals," *Journal of the American Ceramic Society,* vol. 84, pp. 1755-1762, 2001.

[79] S. C. Gill and T. W. Clyne, "Stress Distributions and Material Response in Thermal Spraying of Metallic and Ceramic Deposits," *Metallurgical Transactions,* vol. 21B, pp. 377-385, 1990.

[80] C. C. Berndt and C.-K. Lin, "Measurement of adhesion of thermally sprayed materials," *Journal of Adhesion Science Technology,* vol. 7, pp. 1235-1264, 1993.

[81] C.-O. Moon and S.-B. Lee, "Analysis on failures of protective-oxide layers and cyclic oxidation," *Oxidation of Metals,* vol. 39, pp. 1-13, 1993.

[82] K. Kokini and Y. R. Takeuchi, "Initiation of surface cracks in multilayer ceramic thermal barrier coatings under thermal loads," *Materials Science and Engineering,* vol. A189, pp. 301-309, 1994.

[83] K. Kokini and Y. Takeuchi, "Transient thermal fracture of an interface crack in the presence of a surface crack," *Journal of Thermal Stresses,* vol. 17, pp. 63-74, 1994.

[84] G. Bolelli, L. Lusvarghi, T. Varis, E. Turunen, M. Leoni, P. Scardi, C. L. Azanza-Ricardo, and M. Barletta, "Residual stresses in HVOF-sprayed ceramic coatings," *Surface and Coatings Technology,* vol. 202, pp. 4810-4819, 2008.

[85] V. Teixeira, M. Andritschky, W. Fischer, H. P. Buchkremer, and D. Stover, "Analysis of Residual Stresses in Thermal Barrier Coatings," *Journal of Materials Processing Technology,* vol. 93, pp. 209-216, 1999.

[86] Q. Chen, W. G. Mao, Y. C. Zhou, and C. Lu, "Effect of Young's modulus evolution on residual stress measurement of thermal barrier coatings by X-ray diffraction," *Applied Surface Science,* vol. 256, pp. 7311-7315, 2010.

[87] M. Levit, I. Grimberg, and B. Z. Weiss, "Residual stresses in ceramic plasma-sprayed thermal barrier coatings: measurement and calculation," *Materials Science and Engineering: A,* vol. 206, pp. 30-38, 1996.

[88] M. Tanaka, M. Hasegawa, A. F. Dericioglu, and Y. Kagawa, "Measurement of residual stress in air plasma-sprayed Y_2O_3–ZrO_2 thermal barrier coating system using micro-Raman spectroscopy," *Materials Science and Engineering,* vol. A419, pp. 262-268, 2006.

[89] A. Portinha, V. Teixeira, J. Carneiro, M. G. Beghi, C. E. Bottani, N. Franco, R. Vassen, D. Stoever, and A. D. Sequeira, "Residual stresses and elastic modulus of thermal barrier coatings graded in porosity," *Surface and Coatings Technology,* vol. 188-189, pp. 120-128, 2004.

[90] V. Teixeira, M. Andritschky, W. Fischer, H. P. Buchkremer, and D. Stover, "Effects of deposition temperature and thermal cycling on residual stress state in zirconia-based thermal barrier coatings," *Surface and Coatings Technology,* vol. 121, pp. 103-111, 1999.

[91] S. C. Gill and T. W. Clyne, "Investigation of Residual Stress Generation during Thermal spraying by Continuous Curvature Measurement," *Thin Solid Films,* vol. 250, pp. 172-180, 1994.

[92] P. Bengtsson and C. Persson, "Modelled and Measured Residual Stresses in Plasma Sprayed Thermal Barrier Coatings," *Surface and Coatings Technology,* vol. 92, pp. 78-86, 1997.

[93] Y. C. Tsui and T. W. Clyne, "An Analytical Model for Predicting Residual Stresses in Progressively Deposited Coatings. Part 1: Planar Geometry," *Thin Solid Films,* vol. 306, pp. 23-33, 1997.

[94] S. Takeuchi, M. Ito, and K. Takeda, "Modelling of Residual Stress in Plasma-Sprayed Coatings: Effect of Substrate Temperature," *Surface and Coatings Technology,* vol. 43/44, pp. 426-435, 1990.

[95] Y. C. Tsui and T. W. Clyne, "An Analytical Model for Predicting Residual Stresses in Progressively Deposited Coatings. Part 3: Further Development and Applications," *Thin Solid Films,* vol. 306, pp. 52-61, 1997.

[96] Y. C. Tsui and T. W. Clyne, "An Analytical Model for Predicting Residual Stresses in Progressively Deposited Coatings. Part 2: Cylindrical Geometry," *Thin Solid Films,* vol. 306, pp. 34-51, 1997.

[97] T. C. Totemeier and J. K. Wright, "Residual stress determination in thermally sprayed coatings--a comparison of curvature models and X-ray techniques," *Surface and Coatings Technology,* vol. 200, pp. 3955-3962, 2006.

[98] M. D. Thouless, "Modeling the development and relaxation of stresses in films," *Annual Review of Materials Science,* vol. 25, pp. 69-96, 1995.

[99] J. L. Beuth, "Cracking of Thin Bonded Films in Residual Tension," *International Journal of Solids and Structures,* vol. 29, pp. 1657-1675, 1992.

[100] M. D. Drory, M. D. Thouless, and A. G. Evans, "On the Decohesion of Residually Stressed Thin Films," *Acta Metallurgica,* vol. 36, pp. 2019-2028, 1988.

[101] M. S. Hu, M. D. Thouless, and A. G. Evans, "The decohesion of thin films from brittle substrates," *Acta Metallurgica,* vol. 36, pp. 1301-1307, 1988.

[102] M. S. Hu and A. G. Evans, "The Cracking and Decohesion of Thin Films on Ductile Substrates," *Acta Metallurgica,* vol. 37, pp. 917-925, 1987.

[103] L. Xie, D. Chen, E. H. Jordan, A. Ozturk, F. Wu, X. Ma, B. M. Cetegen, and M. Gell, "Formation of vertical cracks in solution-precursor plasma-sprayed thermal barrier coatings," *Surface and Coatings Technology,* vol. 201, pp. 1058-1064, 2006.

[104] J. Go, Y. G. Jung, S. Kim, and U. Paik, "Analysis of thermoelastic characteristics for vertical-cracked thermal barrier coatings through mathematical approaches," *Surface and Coatings Technology,* vol. 206, pp. 1615-1620, 2011.

[105] T. A. Schaedler, R. M. Leckie, S. Krämer, A. G. Evans, and C. G. Levi, "Toughening of Nontransformable t′ -YSZ by Addition of Titania," *Journal of the American Ceramic Society,* vol. 90, pp. 3896-3901, 2007.

[106] F. M. Pitek and C. G. Levi, "Opportunities for TBCs in the ZrO_2–$YO_{1.5}$–$TaO_{2.5}$ system," *Surface and Coatings Technology,* vol. 201, pp. 6044-6050, 2007.

[107] M. Watanabe, Mercer, C., Levi, C. G. and Evans, A. G., "A Probe for the High Temperature Deformation of Thermal Barrier Oxides," *Acta Materialia,* vol. 52, pp. 1479-1487, 2004.

[108] G. Thurn, G. A. Schneider, H. A. Bahr, and F. Aldinger, "Toughness anisotropy and damage behavior of plasma sprayed ZrO_2 thermal barrier coatings," *Surface and Coatings Technology,* vol. 123, pp. 147-158, 2000.

[109] X. Wang, C. Wang, and A. Atkinson, "Interface fracture toughness in thermal barrier coatings by cross-sectional indentation," *Acta Materialia,* vol. 60, pp. 6152-6163, 2012.

[110] S. R. Choi, J. W. Hutchinson, and A. G. Evans, "Delamination of Multilayer Thermal Barrier Coatings," *Mechanics of Materials,* vol. 31, pp. 431-447, 1999.

[111] R. G. Hutchinson, N. A. Fleck, and A. C. F. Cocks, "A Sintering Model for Thermal Barrier Coatings," *Acta Materialia,* vol. 54, pp. 1297-1306, 2006.

[112] J. P. Berry, "Some kinetic Considerations of the Griffith Criterion for Fracture-I: Equations of Motion at Constant Force," *Journal of the Mechanics and Physics of Solids,* vol. 8, pp. 194-206, 1960.

[113] S. Sampath, U. Schulz, M. O. Jarligo, and S. Kuroda, "Processing science of advanced thermal-barrier systems," *MRS Bulletin,* vol. 37, pp. 903-910, 2012.

[114] M. Ahrens, S. Lampenscherf, R. Vassen, and D. Stover, "Sintering and creep processes in plasma-sprayed thermal barrier coatings," *Journal of Thermal Spray Technology,* vol. 13, pp. 432-442, Sep 2004.

[115] C. W. Wu, G. N. Chen, K. Zhang, G. X. Luo, and N. G. Liang, "The effect of periodic segmentation cracks on the interfacial debonding: Study on interfacial stresses," *Surface and Coatings Technology,* vol. 201, pp. 287-291, 2006.

[116] J. C. Grosskreutz, "Mechanical Properties of Metal Oxide Films," *Journal of the Electrochemical Society,* vol. 116, pp. 1232-1237, 1969.

[117] S. P. Timoshenko and J. N. Goodier, *Theory of Elasticity*. New York: McGraw-Hill, 1982.

[118] S. Ochiai and K. Osamura, "Stress distribution in a segmented coating film on metal fibre under tensile loading," *Journal of Materials Science,* vol. 21, pp. 2744-2752, 1986.

[119] M. M. Nagl and W. T. Evans, "The mechanical failure of oxide scales under tensile or compressive load," *Journal of Materials Science,* vol. 28, pp. 6247-6260, 1993.

[120] M. D. Thouless, "Crack spacing in brittle films on elastic substrates," *Journal of the American Ceramic Society,* vol. 73, pp. 2144-2146, 1990.

[121] M. D. Thouless, E. Olsson, and A. Gupta, "Cracking of brittle films on elastic substrates," *Acta Metallurgica et Materialia,* vol. 40, pp. 1287-1292, 1992.

[122] J. W. Hutchinson and Z. Suo, "Mixed mode cracking in layered materials," *Advances in Applied Mechanics,* vol. 29, pp. 63-191, 1992.

[123] F. Delannay and P. Warren, "On Crack Interaction and Crack Density in Strain-Induced Cracking of Brittle Films on Ductile Substrates," *Acta Metallurgica,* vol. 39, pp. 1061-1072, 1991.

[124] M. S. Hu, M. D. Thouless, and A. G. Evans, "The Decohesion of Thin Films from Brittle Substrates," *Acta Metallurgica,* vol. 36, pp. 1301-1307, 1988.

[125] A. G. Evans, M. Rühle, B. J. Dalgleish, and P. G. Charalambides, "The Fracture Energy of Bimaterial Interfaces," *Materials Science and Engineering,* vol. A126, pp. 53-64, 1990.

[126] T. W. Clyne, "Residual Stresses in Surface Coatings and their Effects on Interfacial Debonding," *Key Engineering Materials,* vol. 116/7, pp. 307-330, 1996.

[127] S. Paul, "Assessing Coating Reliability Through Pore Architecture Evaluation," *Journal of Thermal Spray Technology,* vol. 19, pp. 779-786, 2010.

[128] G. Qian, T. Nakamura, and C. C. Berndt, "Effects of thermal gradient and residual stresses on thermal barrier coating fracture," *Mechanics of Materials,* vol. 27, pp. 91-110, 1998.

[129] H. Balke, I. Hofinger, C. Hausler, H. A. Bahr, H. J. Weiss, and G. Kirchhoff, "Fracture mechanical damage modelling of thermal barrier coatings," *Archive of Applied Mechanics,* vol. 70, pp. 193-200, 2000.

[130] T. Patterson, D. I. Orloff, and F. Bloom, "Delamination buckling and spalling of plasma-sprayed thermal barrier coatings," *Mathematical and Computer Modelling,* vol. 35, pp. 165-190, 2002.

[131] A. G. Evans and J. W. Hutchinson, "The mechanics of coating delamination in thermal gradients," *Surface and Coatings Technology,* vol. 201, pp. 7905 - 7916, 2007.

[132] P. Y. Théry, M. Poulain, M. Dupeux, and M. Braccini, "Spallation of two thermal barrier coating systems: experimental study of adhesion and energetic approach to lifetime during cyclic oxidation," *Journal of Materials Science,* vol. 44, pp. 1726-1733, 2009.

[133] H. E. Evans, "Oxidation failure of TBC systems: An assessment of mechanisms," *Surface and Coatings Technology,* vol. 206, pp. 1512–1521, 2011.

[134] A. N. Khan and J. Lu, "Thermal cyclic behavior of air plasma sprayed thermal barrier coatings sprayed on stainless steel substrates," *Surface and Coatings Technology,* vol. 201, pp. 4653-4658, 2007.

[135] C. A. Johnson, J. A. Ruud, R. Bruce, and D. Wortman, "Relationships between Residual Stress, Microstructure and Mechanical Properties of Electron Beam Physical Vapor Deposition Thermal Barrier Coatings," *Surface and Coatings Technology,* vol. 109, pp. 80-85, 1998.

[136] H. Zhao, Z. Yu, and H. N. G. Wadley, "The influence of coating compliance on the delamination of thermal barrier coatings," *Surface and Coatings Technology,* vol. 204, pp. 2432-2441, 2010.

[137] D. L. Ruckle, "Plasma-Sprayed Ceramic Thermal Barrier Coatings for Turbine Vane Platforms," *Thin Solid Films,* vol. 73, pp. 455-461, 1980.

[138] Y.-D. Lee and F. Erdogan, "Residual Thermal Stresses in FGM and Laminated Thermal Barrier Coatings," *International Journal of Fracture,* vol. 69, pp. 145-165, 1994.

[139] A. R. Akisanya and N. A. Fleck, "The Edge Cracking and Decohesion of Thin Films," *International Journal of Solids and Structures,* vol. 31, pp. 3175 - 3199, 1994.

[140] Y. C. Tsui, S. J. Howard, and T. W. Clyne, "Application of a Model for the Effect of Residual Stresses on Debonding of Coatings under

Applied Loads," in *Advances in Inorganic Films and Coatings*, P. Vincenzini, Ed., ed: Techna Srl., 1995, pp. 19-26.

[141] H. C. Cao, M. D. Thouless, and A. G. Evans, "Residual Stresses and Cracking in Brittle Solids Bonded with a Thin Ductile Layer," *Acta Metallurgica,* vol. 36, pp. 2037-2046, 1988.

[142] L. L. Shaw, B. Barber, E. H. Jordan, and M. Gell, "Measurements of interfacial fracture energy of thermal barrier coatings," *Acta Metallurgica,* vol. 39, pp. 209-222, 1998.

[143] D. Z. Guo and L. J. Wang, "Measurement of the Critical Strain Energy Release Rate of Plasma-Sprayed Coatings," *Surface and Coatings Technology,* vol. 56, pp. 19-25, 1992.

[144] Y. Yamazaki, A. Schmidt, and A. Scholz, "The determination of the delamination resistance in thermal barrier coating system by four-point bending tests," *Surface and Coatings Technology,* vol. 201, pp. 744 - 754, 2006.

[145] M. R. Begley, D. R. Mumm, A. G. Evans, and J. W. Hutchinson, "Analysis of a wedge impression test for measuring the interface toughness between films/coatings and ductile substrates," *Acta Materialia,* vol. 48, pp. 3211-3220, 2000.

[146] A. Vasinonta and J. L. Beuth, "Measurement of interfacial toughness in thermal barrier coating systems by indentation," *Engineering Fracture Mechanics,* vol. 68, pp. 843-860, 2001.

[147]Y. Zhao, A. Shinmi, X. Zhao, P. J. Withers, S. Van Boxel, N. Markocsan, P. Nylen, and P. Xiao, "Investigation of interfacial properties of atmospheric plasma sprayed thermal barrier coatings with four-point bending and computed tomography technique," *Surface and Coatings Technology,* vol. 206, pp. 4922-4929, 2012.

[148] Y. C. Tsui, X. L. Peng, and T. W. Clyne, "Modelling of Residual Stresses generated during Progressive Deposition of a Surface Coating using Analytical and Numerical Techniques," in *5th International Conference on Residual Stresses*, T. Ericsson, M. Oden, and A. Andersson, Eds., ed Linkoping: Linkoping University Press, 1998, pp. 442-447.

[149] A. G. Evans and J. W. Hutchinson, "Effects of Non-planarity on the Mixed Mode Fracture Resistance of Bimaterial Interfaces," *Acta Metallurgica,* vol. 37, pp. 909-916, 1989.

[150] M. Arai, Y. Okajima, and K. Kishimoto, "Mixed-mode interfacial fracture toughness for thermal barrier coating," *Engineering Fracture Mechanics,* vol. 74, pp. 2055-2069, 2007.

[151] J. W. Hutchinson and A. G. Evans, "On the delamination of thermal barrier coatings in a thermal gradient," *Surface and Coatings Technology,* vol. 149, pp. 179-184, 2002.

[152] K. Vaidyanathan, E. H. Jordan, and M. Gell, "Surface geometry and strain energy effects in the failure of a (Ni,Pt)Al/EB-PVD thermal barrier coating," *Acta Materialia,* vol. 52, pp. 1107-1115, 2004.
[153] R. A. Miller and C. E. Lowell, "Failure Mechanisms of Thermal Barrier Coatings Exposed to Elevated Temperatures," *Thin Solid Films,* vol. 95, pp. 265-273, 1982.
[154] P. A. Langjahr, R. Oberacker, and M. J. Hoffmann, "Long-term behaviour and application limits of plasma sprayed zirconia thermal barrier coatings," *Journal of the American Ceramic Society,* vol. 84, pp. 1301-1308, 2001.
[155] H. Jamali, R. Mozafarinia, R. Shoja Razavi, and R. Ahmadi-Pidani, "Comparison of thermal shock resistances of plasma-sprayed nanostructured and conventional yttria stabilized zirconia thermal barrier coatings," *Ceramics International,* vol. 38, pp. 6705-6712, 2012.
[156] D. Zhu, S. R. Choi, and R. A. Miller, "Development and thermal fatigue testing of ceramic thermal barrier coatings," *Surface and Coatings Technology,* vol. 188-189, pp. 146-152, 2004.
[157] R. C. Rossi, "Prediction of the Elastic Moduli of Composites," *Journal of the American Ceramic Society,* vol. 51, pp. 433-440, 1968.
[158] R. M. Spriggs, "Expression for effect of porosity on elastic modulus of polycrystalline refractory materials, particularly aluminum oxide," *Science of Sintering,* vol. 18, pp. 68-70, 1986.
[159] P. K. Wright, "Influence of cyclic strain on life of a PVD TBC," *Materials Science and Engineering,* vol. A245, pp. 191-200, 1998.
[160] F. Kroupa, "Nonlinear behavior in compression and tension of thermally sprayed ceramic coatings," *Journal of Thermal Spray Technology,* vol. 16, pp. 84-95, 2007.
[161] Y. Liu, T. Nakamura, V. Srinivasan, A. Vaidya, A. Gouldstone, and S. Sampath, "Non-linear elastic properties of plasma-sprayed zirconia coatings and associated relationships with processing conditions," *Acta Materialia,* vol. 55, pp. 4667-4678, 2007.
[162] E. F. Rejda, D. F. Socie, and T. Itoh, "Deformation behavior of plasma-sprayed thick thermal barrier coatings," *Surface and Coatings Technology,* vol. 113, pp. 218-226, 1999.
[163] J. A. Thompson and T. W. Clyne, "The Effect of Heat Treatment on the Stiffness of Zirconia Top Coats in Plasma-Sprayed TBCs," *Acta Materialia,* vol. 49, pp. 1565-1575, 2001.
[164] S. R. Choi, D. Zhu, and R. A. Miller, "Deformation and Tensile Cyclic Fatigue of Plasma-Sprayed ZrO_2-8wt % Y_2O_3 Thermal barrier Coatings," *Ceramic Engineering and Science Proceedings,* vol. 22, pp. 427-434, 2001.

[165] T. Wakui, J. Malzbender, and R. W. Steinbrech, "Strain dependent stiffness of plasma sprayed thermal barrier coatings," *Surface and Coatings Technology,* vol. 200, pp. 4995-5002, Apr 2006.
[166] Y. Tan, A. Shyam, W. B. Choi, E. Lara-Curzio, and S. Sampath, "Anisotropic elastic properties of thermal spray coatings determined via resonant ultrasound spectroscopy," *Acta Materialia,* vol. 58, pp. 5305-5315, 2010.
[167] J. Malzbender and R. W. Steinbrech, "Determination of the Stress-Dependent Stiffness of Plasma-Sprayed Thermal Barrier Coatings Using Depth-Sensitive Indentation," *Journal of Materials Research,* vol. 18, pp. 1975-1984, 2003.
[168] D. M. Zhu and R. A. Miller, "Thermal Conductivity and Elastic Modulus Evolution of Thermal Barrier Coatings under High Heat Flux Conditions," *Journal of Thermal Spray Technology,* vol. 9, pp. 175-180, 2000.
[169] P. K. Wright and A. G. Evans, "Mechanisms Governing the Performance of Thermal Barrier Coatings," *Current Opinion in Solid State and Materials Science,* vol. 4, pp. 255-265, 1999.
[170] E. A. Olevsky, "Theory of sintering: from discrete to continuum," *Materials Science and Engineering: R: Reports,* vol. 23, pp. 41-100, 1998.
[171] S. R. Choi, D. M. Zhu, and R. A. Miller, "Effect of sintering on mechanical properties of plasma-sprayed zirconia-based thermal barrier coatings," *Journal of the American Ceramic Society,* vol. 88, pp. 2859-2867, Oct 2005.
[172] L. Xie, M. R. Dorfman, A. Cipitria, S. Paul, I. O. Golosnoy, and T. W. Clyne, "Properties and Performance of High Purity Thermal Barrier Coatings," in *International Thermal Spray Conference*, Beijing, China, 2007.
[173] S. A. Tsipas, I. O. Golosnoy, and T. W. Clyne, "The Effect of a High Thermal Gradient on Sintering and Stiffening in the Top Coat of a Thermal Barrier Coating (TBC) System," in *International Thermal Spray Conference 2003*, Orlando, Florida, USA, 2003, pp. 1547-1552.
[174] C. Pfeiffer, E. Affeldt, and M. Göken, "Miniaturized bend tests on partially stabilized EB-PVD ZrO_2 thermal barrier coatings," *Surface and Coatings Technology,* vol. 205, pp. 3245-3250, 2011.
[175] F. Traeger, M. Ahrens, R. Vaßen, and D. Stöver, "A life time model for ceramic thermal barrier coatings," *Materials Science and Engineering: A,* vol. 358, pp. 255-265, 2003.
[176] M. van Roode, "Ceramic Gas Turbine Development: Need for a 10 Year Plan," *Journal of Engineering for Gas Turbines and Power,* vol. 132, pp. 1-10, 2010.

[177] S. Paul, A. Cipitria, I. O. Golosnoy, and T. W. Clyne, "Effects of Impurity Content on the Sintering Characteristics of Plasma Sprayed Zirconia," *Journal of Thermal Spray Technology* vol. 16, pp. 798-803, 2007.
[178] A. Cipitria, I. O. Golosnoy, and T. W. Clyne, "A Sintering Model for Plasma-Sprayed Zirconia TBCs. Part I: Free-Standing Coatings," *Acta Materialia,* vol. 57, pp. 980–992, 2009.
[179] A. Cipitria, I. O. Golosnoy, and T. W. Clyne, "A Sintering Model for Plasma-Sprayed Zirconia TBCs. Part II: Coatings bonded to a Rigid Substrate," *Acta Materialia,* vol. 57, pp. 993–1003, 2009.
[180] S. A. Tsipas, I. O. Golosnoy, R. Damani, and T. W. Clyne, "The Effect of a High Thermal Gradient on Sintering and Stiffening in the Top Coat of a Thermal Barrier Coating (TBC) System," *Journal of Thermal Spray Technology,* vol. 13, pp. 370-376, 2004.
[181] S. C. Gill and T. W. Clyne, "Monitoring of Residual Stress Generation during Thermal Spraying by Curvature Measurements," in *Thermal Spray Industrial Applications*, C. C. Berndt and S. Sampath, Eds., ed Materials Park, Ohio: ASM, 1994, pp. 581-586.
[182] H. J. Ratzer-Scheibe, U. Schulz, and T. Krell, "The effect of coating thickness on the thermal conductivity of EB-PVD PYSZ thermal barrier coatings," *Surface and Coatings Technology,* vol. 200, pp. 5636-5644, May 2006.
[183] I. O. Golosnoy, A. Cipitria, and T. W. Clyne, "Heat Transfer Through Plasma-Sprayed Thermal Barrier Coatings in Gas Turbines : A Review of Recent Work," *Journal of Thermal Spray Technology,* vol. 18, pp. 809-821, 2009.
[184] W. J. Parker, R. J. Jenkins, C. P. Butler, and G. L. Abbott, "Flash Method of Determining Thermal Diffusivity, Heat Capacity and Thermal Conductivity," *Journal of Applied Physics,* vol. 32, pp. 1679-1684., 1961.
[185] L. M. Clark and R. E. Taylor, "Radiation loss in the flash method for thermal diffusivity," *Journal of Applied Physics,* vol. 46, pp. 714-719, 1975.
[186] S. E. Gustafsson, "Transient Plane Source Techniques for Thermal Conductivity and Thermal Diffusivity Measurements of Solid Materials," *Review of Scientific Instruments,* vol. 62, pp. 797-804, 1990.
[187] J. C. Tan, S. A. Tsipas, I. O. Golosnoy, S. Paul, J. A. Curran, and T. W. Clyne, "A Steady-State Bi-Substrate Technique for Measurement of the Thermal Conductivity of Ceramic Coatings," *Surface and Coatings Technology,* vol. 201, pp. 1414-1420, 2006.
[188] H. Wang and R. B. Dinwiddie, "Reliability of the Laser Flash Thermal Diffusivity Measurements of the Thermal Barrier Coatings," *Journal of Thermal Spray Technology,* vol. 9, pp. 210-214, 2000.

[189] C. Degueldre, P. Tissot, H. Lartigue, and M. Pouchon, "Specific heat capacity and Debye temperature of zirconia and its solid solution," *Thermochimica Acta,* vol. 403, pp. 267-273, 2003.

[190] A. Mogro-Campero, C. A. Johnson, P. J. Bednarczyk, R. B. Dinwiddie, and H. Wang, "Effect of Gas Pressure on Thermal Conductivity of Zirconia Thermal Barrier Coatings," *Surface and Coatings Technology,* vol. 94-5, pp. 102-105, 1997.

[191] F. Cernuschi, L. Lorenzoni, S. Ahmaniemi, P. Vuoristo, and T. Mäntylä, "Studies of the Sintering Kinetics of Thick Thermal Barrier Coatings by Thermal Diffusivity Measurements," *Journal of the European Ceramic Society,* vol. 25, pp. 393-400, 2005.

[192] R. Vassen, N. Czech, W. Mallener, W. Stamm, and D. Stoever, "Influence of Impurity Content and Porosity of Plasma-Sprayed Yttria-Stabilized Zirconia Layers on the Sintering Behaviour," *Surface and Coatings Technology,* vol. 141, pp. 135-140, 2001.

[193] D. P. F. De Souza and M. F. De Souza, "Liquid phase sintering of RE_2O_3: YSZ ceramics," *Journal of Materials Science,* vol. 34, pp. 4023-4030, 1999.

[194] H. E. Eaton and R. C. Novak, "Sintering Studies of Plasma Sprayed Zirconia," *Surface and Coatings Technology,* vol. 32, pp. 227-236, 1987.

[195] H. C. Chen, E. Pfender, and J. Heberlein, "Plasma-Sprayed ZrO_2 Thermal Barrier Coatings Doped with an Appropriate Amount of SiO_2," *Thin Solid Films,* vol. 315, pp. 159-169, 1998.

[196] S. Stemmer, J. Vleugels, and O. Van Der Biest, "Grain boundary segregation in high-purity yttria-stabilized tetragonal zirconia polygrystals (T-TZP)," *Journal of the European Ceramic Society,* vol. 18, pp. 1565-1570, 1998.

[197] R. K. Bordia and R. Raj, "Sintering Behaviour of Ceramic Films Constrained by a Rigid Substrate," *Journal of the American Ceramic Society,* vol. 68, pp. 287-292, 1985.

[198] Y. Zhao and L. R. Dharani, "Theoretical model for the analysis of a ceramic thin film sintering on a non-sintering substrate," *Thin Solid Films,* vol. 245, pp. 109-114, 1994.

[199] K. Kokini, Y. R. Takeuchi, and B. D. Choules, "Surface thermal cracking of thermal barrier coatings owing to stress relaxation: zirconia vs. mullite," *Surface and Coatings Technology,* vol. 82, pp. 77-82, 1996.

[200] B. D. Choules, K. Kokini, and T. A. Taylor, "Thermal Fracture of Thermal Barrier Coatings in a High Temperature Heat Flux Environment," *Surface and Coatings Technology,* vol. 106, pp. 23-9, 1998.

[201] U. Schulz, "Phase Transformation in EB-PVD Yttria Partially Stabilized Zirconia Thermal Barrier Coatings during Annealing," *Journal of the American Ceramic Society,* vol. 83, pp. 904-910, 2000.

[202] J. Moon, H. Choi, H. Kim, and C. Lee, "The effects of heat treatment on the phase transformation behaviour of plasma-sprayed stabilized ZrO_2 coatings," *Surface and Coatings Technology,* vol. 155, pp. 1-10, 2002.

[203] J. R. VanValzah and H. E. Eaton, "Cooling Rate Effects on the Tetragonal to Monoclinic Phase Transformation in Aged Plasma-Sprayed Yttria Partially Stabilised Zirconia," *Surface and Coatings Technology,* vol. 46, pp. 289-300, 1991.

[204] P. Scardi, M. Leoni, and L. Bertarmini, "Influence of Phase Stability on the Residual Stress in Partially Stabilised Zirconia TBC Produced by Plasma Spray," *Surface and Coatings Technology,* vol. 76/77, pp. 106-112, 1995.

[205] C. G. Levi, J. W. Hutchinson, M. H. Vidal-Sétif, and C. A. Johnson, "Environmental degradation of thermal-barrier coatings by molten deposits," *MRS Bulletin,* vol. 37, pp. 932-941, 2012.

[206] M. H. Vidal-Setif, N. Chellah, C. Rio, C. Sanchez, and O. Lavigne, "Calcium-Magnesium-Alumino-Silicate (CMAS) degradation of EB-PVD thermal barrier coatings: Characterization of CMAS damage on ex-service high pressure blades TBCs," *Surface and Coatings Technology,* vol. 208, pp. 39-45, 2012.

[207] A. Aygun, A. L. Vasiliev, and N. P. Padture, "Novel thermal barrier coatings that are resistant to high-temperature attack by glassy deposits," *Acta Materialia,* vol. 55, pp. 6734-6745, 2007.

[208] S. Kramer, J. Yang, C. G. Levi, and C. A. Johnson, "Thermochemical Interaction of Thermal Barrier Coatings with Molten $CaO–MgO–Al2O_3 –SiO_2$ (CMAS) Deposits," *Journal of American Ceramic Society,* vol. 89, pp. 3167-3175, 2006.

[209] M. P. Borom, C. A. Johnson, and L. A. Peluso, "Role of environmental deposits and operating surface temperature in spallation of air plasma sprayed thermal barrier coatings," *Surface and Coatings Technology,* vol. 87, pp. 116-126, 1996.

[210] S. Kramer, S. Faulhaber, M. Chambers, D. R. Clarke, C. G. Levi, J. W. Hutchinson, and A. G. Evans, "Mechanisms of cracking and delamination within thick thermal barrier systems in aero-engines subject to calcium-magnesium-alumino-silicate (CMAS) penetration," *Materials Science and Engineering A,* vol. 490, pp. 26-35, 2008.

[211] X. Chen, "Calcium–magnesium–alumina–silicate (CMAS) delamination mechanisms in EB-PVD thermal barrier coatings " *Surface and Coatings Technology,* vol. 200, pp. 3418-3427, 2006.

[212] L. Li, N. Hitchman, and J. Knapp, "Failure of thermal barrier coatings subjected to CMAS attack," *Journal of Thermal Spray Technology,* vol. 19, pp. 148-155, 2010.

[213] J. Wu, H.-b. Guo, Y.-z. Gao, and S.-k. Gong, "Microstructure and thermo-physical properties of yttria stabilized zirconia coatings with CMAS deposits," *Journal of the European Ceramic Society,* vol. 31, pp. 1881-1888, 2011.

[214] L. Li and D. R. Clarke, "Effect of CMAS Infiltration on Radiative Transport Through an EB-PVD Thermal Barrier Coating," *International Journal of Applied Ceramic Technology,* vol. 5, pp. 278-288, 2008.

[215] K. Brun, M. Nored, and R. Kurz, "Particle Transport Analysis of Sand Ingestion in Gas Turbine Engines," *Journal of Engineering for Gas Turbines and Power,* vol. 134, p. article number 012402, 2012.

[216] W. Ai and T. H. Fletcher, "Computational Analysis of Conjugate Heat Transfer and Particulate Deposition on a High Pressure Turbine Vane," *Journal of Turbomachinery,* vol. 134, p. article number 041020, 2012.

[217] J. P. Bons, J. Crosby, J. E. Wammack, B. I. Bentley, and T. H. Fletcher, "High-Pressure Turbine Deposition in Land-Based Gas Turbines From Various Synfuels," *Journal of Engineering for Gas Turbines and Power,* vol. 129, pp. 135-143, 2007.

[218] J. P. Bons, R. P. Taylor, S. T. McClain, and R. B. Rivir, "The Many Faces of Turbine Surface Roughness," *Journal of Turbomachinery,* vol. 123, pp. 739-748, 2001.

[219] A. Hamed, W. Tabakoff, and R. Wenglarz, "Erosion and Deposition in Turbomachinery," *Journal of Propulsion and Power,* vol. 22, pp. 350-360, 2006.

[220] A. Shah and D. K. Tafti, "Transport of Particulates in an Internal Cooling Ribbed Duct," *Journal of Turbomachinery,* vol. 129, pp. 816-825, 2007.

[221] S. A. Lawson and K. A. Thole, "Effects of Simulated Particle Deposition on Film Cooling," *Journal of Turbomachinery,* vol. 133, pp. 021009-021009, 2010.

[222] A. Guha, "Transport and deposition of particles in turbulent and laminar flow," *Annual Review of Fluid Mechanics,* vol. 40, pp. 311-341, 2008.

[223] W. S. Walsh, K. A. Thole, and C. Joe, "Effects of sand ingestion on the blockage of film-cooling holes," in *Proceedings of GT2006 ASME Turbo Expo 2006: Power for Land, Sea and Air*, Barcelona, Spain, 2006, pp. 81-90.

[224] J. W. Jensen, S. W. Squire, J. P. Bons, and T. H. Fletcher, "Simulated Land-Based Turbine Deposits Generated in an Accelerated Deposition Facility," *Journal of Turbomachinery,* vol. 127, pp. 462-470, 2005.

[225] J. M. Crosby, S. Lewis, J. P. Bons, W. Ai, and T. H. Fletcher, "Effects of Temperature and Particle Size on Deposition in Land Based Turbines," *Journal of Engineering for Gas Turbines and Power,* vol. 130, p. article number 051503, 2008.

[226] W. Ai, N. Murray, T. H. Fletcher, S. Harding, S. Lewis, and J. P. Bons, "Deposition Near Film Cooling Holes on a High Pressure Turbine Vane," *Journal of Turbomachinery,* vol. 134, p. article number 041013, 2011.

[227] A. Rozati, D. K. Tafti, and S. S. Sreedharan, "Effects of Syngas Ash Particle Size on Deposition and Erosion of a Film Cooled Leading Edge," *Journal of Turbomachinery,* vol. 133, p. article number 011010, 2011.

[228] C. Mercer, S. Faulhaber, A. G. Evans, and R. Darolia, "A delamination mechanism for thermal barrier coatings subject to calcium–magnesium–alumino-silicate (CMAS) infiltration " *Acta Materialia,* vol. 53, pp. 1029-1039, 2005.

[229] J. M. Drexler, A. D. Gledhill, K. Shinoda, A. L. Vasiliev, K. M. Reddy, S. Sampath, and N. P. Padture, "Jet Engine Coatings for Resisting Volcanic Ash Damage," *Advanced Materials,* vol. 23, pp. 2419-2424, 2011.

[230] A. D. Gledhill, K. M. Reddy, J. M. Drexler, K. Shinoda, S. Sampath, and N. P. Padture, "Mitigation of damage from molten fly ash to air-plasma-sprayed thermal barrier coatings," *Materials Science and Engineering: A,* vol. 528, pp. 7214-7221, 2011.

[231] A. Aygun, A. L. Vasiliev, N. P. Padture, and X. Ma, "Novel Thermal Barrier Coatings that are Resistant to High-Temperature Attack by Glassy Deposits," *Acta Materialia,* vol. 55, pp. 6734-6745, 2007.

[232] B. J. Harder, J. Ramìrez-Rico, J. D. Almer, K. N. Lee, and K. T. Faber, "Chemical and Mechanical Consequences of Environmental Barrier Coating Exposure to Calcium–Magnesium–Aluminosilicate," *Journal of the American Ceramic Society,* vol. 94, pp. s178-s185, 2011.

[233] G. Mauer and R. Vaßen, "Current developments and challenges in thermal barrier coatings," *Surface Engineering,* vol. 27, pp. 477-479, 2011.

[234] H. Peng, L. Wang, L. Guo, W. Miao, H. Guo, and S. Gong, "Degradation of EB-PVD thermal barrier coatings caused by CMAS deposits," *Progress in Natural Science: Materials International,* 2012.

[235] D. J. de Wet, R. Taylor, and F. H. Stott, "Corrosion mechanisms of ZrO_2-$Y2O_3$ thermal barrier coatings in the presence of molten middle-east sand," *Le Journal de Physique IV,* vol. 03, pp. 655-663, 1993.

[236] J. Smialek, F. Archer, and R. Garlick, "Turbine airfoil degradation in the persian gulf war," *JOM Journal of the Minerals, Metals and Materials Society,* vol. 46, pp. 39-41, 1994.

[237] W. Braue and P. Mechnich, "Recession of an EB-PVDYSZ Coated Turbine Blade by $CaSO_4$ and Fe, Ti-Rich CMAS-Type Deposits," *Journal of the American Ceramic Society,* vol. 94, pp. 4483-4489, 2011.

[238] H. Djohari, J. I. Martínez-Herrera, and J. J. Derby, "Transport mechanisms and densification during sintering: I. Viscous flow versus vacancy diffusion," *Chemical Engineering Science,* vol. 64, pp. 3799-3809, 2009.

[239] H. Djohari and J. J. Derby, "Transport mechanisms and densification during sintering: II. Grain boundaries," *Chemical Engineering Science,* vol. 64, pp. 3810-3816, 2009.

[240] R. M. German, *Liquid Phase Sintering*. New York: Plenum Press, 1985.

[241] W. D. Kingery, "Densification during Sintering in the Presence of a Liquid Phase. I. Theory," *Journal of Applied Physics,* vol. 30, 1958.

[242] M.-P. Bacos, J.-M. Dorvaux, S. Landais, R. Mévrel, M. Poulain, C. Rio, and M. Vidal-Sétif, "10 Years-Activities at Onera on Advanced Thermal Barrier Coatings," *AerospaceLab,* pp. 1-14, 2011.

[243] J. M. Drexler, C.-H. Chen, A. D. Gledhill, K. Shinoda, S. Sampath, and N. P. Padture, "Plasma sprayed gadolinium zirconate thermal barrier coatings that are resistant to damage by molten Ca–Mg–Al–silicate glass," *Surface and Coatings Technology,* vol. 206, pp. 3911-3916, 2012.

[244]J. M. Drexler, K. Shinoda, A. L. Ortiz, D. Li, A. L. Vasiliev, A. D. Gledhill, S. Sampath, and N. P. Padture, "Air-plasma-sprayed thermal barrier coatings that are resistant to high-temperature attack by glassy deposits," *Acta Materialia,* vol. 58, pp. 6835-6844, 2010.

[245] C. J. Horwell, G. W. Stannett, D. Andronico, A. Bertagnini, I. Fenoglio, B. Fubini, J. S. L. Blond, and B. J. Williamson, "A physico-chemical assessment of the health hazard of Mt . Vesuvius volcanic ash," *Journal of Volcanology and Geothermal Research,* vol. 191, pp. 222-232, 2010.

[246] T. J. Casadevall, "The 1989-1990 eruption of Redoubt Volcano , Alaska : impacts on aircraft operations," *Journal of Volcanology and Geothermal Research,* vol. 62, pp. 301-316, 1994.

[247] S. R. Gislason, T. Hassenkam, S. Nedel, N. Bovet, E. S. Eiriksdottir, H. A. Alfredsson, C. P. Hem, Z. I. Balogh, K. Dideriksen, N. Oskarsson, B. Sigfusson, G. Larsen, and S. L. S. Stipp, "Characterization of

Eyjafjallajökull volcanic ash particles and a protocol for rapid risk assessment," *Proceedings of the National Academy of Sciences of the United States of America,* vol. 108, pp. 7307-7312, 2011.

[248] B. Langmann, A. Folch, M. Hensch, and V. Matthias, "Volcanic ash over Europe during the eruption of Eyjafjallajökull on Iceland, April-May 2010," *Atmospheric Environment,* vol. 48, pp. 1-8, 2012.

[249] P. Mechnich, W. Braue, and U. Schulz, "High-Temperature Corrosion of EB-PVD Yttria Partially Stabilized Zirconia Thermal Barrier Coatings with an Artificial Volcanic Ash Overlay," *Journal of the American Ceramic Society,* vol. 94, pp. 925-931, 2011.

[250] F. Sigmundsson, S. Hreinsdóttir, A. Hooper, T. Árnadóttir, R. Pedersen, M. J. Roberts, N. Óskarsson, A. Auriac, J. Decriem, P. Einarsson, H. Geirsson, M. Hensch, B. G. Ófeigsson, E. Sturkell, H. Sveinbjörnsson, and K. L. Feigl, "Intrusion triggering of the 2010 Eyjafjallajökull explosive eruption," *Nature,* vol. 468, pp. 426-432, 2010.

[251] K. H. Casleton, R. W. Breault, and G. A. Richards, "System issues and tradeoffs associated with syngas production and combustion," *Combustion Science and Technology,* vol. 180, pp. 1013-1052, 2008.

[252] D. R. Spearing and J. Y. Huang, "Zircon Synthesis via Sintering of Milled SiO_2 and ZrO_2," *Journal of the American Ceramic Society,* vol. 81, pp. 1964-1966, 1998.

[253] S. Kramer, J. Yang, and C. G. Levi, "Infiltration-Inhibiting Reaction of Gadolinium Zirconate Thermal Barrier Coatings with CMAS Melts," *Journal of the American Ceramic Society,* vol. 91, pp. 576-583, 2008.

[254] R. Vassen, F. Traeger, and D. Stover, "New Thermal Barrier Coatings Based on Pyrochlore/ YSZ Double-Layer Systems," *International Journal of Applied Ceramic Technology,* vol. 1, 351-361 2004.

[255] R. Vaßen, S. Giesen, and D. Stöver, "Lifetime of Plasma-Sprayed Thermal Barrier Coatings: Comparison of Numerical and Experimental Results," *Journal of Thermal Spray Technology,* vol. 18, pp. 835-845, 2009.

[256] K. W. Schlichting, N. P. Padture, E. H. Jordan, and M. Gell, "Failure Modes in Plasma-Sprayed Thermal Barrier Coatings," *Materials Science and Engineering,* vol. A342, pp. 120-130, 2003.

[257] J. P. Van der Walt and A. Nurickt, "Erosion of Dust-Filtered Helicopter Turbine Engines Part I : Basic Theoretical Considerations," *Journal of Aircraft,* vol. 32, pp. 106-111, 1995.

[258] M. Shinozaki and T. W. Clyne, "A methodology, based on sintering-induced stiffening, for prediction of the spallation lifetime of plasma-sprayed coatings," *Acta Materialia,* vol. 61, pp. 579-588, 2013.

[259] G. R. Dickinson, C. Petorak, K. Bowman, and R. W. Trice, "Stress Relaxation of Compression Loaded Plasma-Sprayed 7 Wt% Y_2O_3–

ZrO_2 Stand-Alone Coatings," *Journal of the American Ceramic Society,* vol. 88, pp. 2202-2208, 2005.

[260] M. Shinozaki and T. W. Clyne, "The effect of vermiculite on the degradation and spallation of plasma sprayed thermal barrier coatings," *Surface and Coatings Technology,* vol. 216, pp. 172-177, 2013.

[261] M. Shinozaki, K. A. Roberts, B. van de Goor, and T. W. Clyne, "Deposition of Ingested Volcanic Ash on Surfaces in the Turbine of a Small Jet Engine," *Advanced Engineering Materials,* vol. Submitted, 2013.

[262] P. F. Batcho, J. C. Moller, C. Padova, and M. G. Dunn, "Interpretation of gas turbine response due to dust ingestion," *Journal of Engineering for Gas Turbines and Power,* vol. 109, pp. 344-352, 1987.

[263] W. Ranz and W. Marshall, "Evaporation from drops," *Chemical Engineering Progress,* vol. 83, pp. 141-146, 1952.

[264] F. Incropera, *Fundamentals of Heat and Mass Transfer*: John Wiley, 2007.

[265] S. Shipley and A. M. Sarna-Wojcicki, "Distribution, thickness, and mass of Late Pleistocene and Holocene tephra from major volcanoes in the northwestern United States: a preliminary assessment of hazards from volcanic ejecta to Nuclear reactors in the Pacific Northwest," *U.S. Geological Survey Miscellaneous Field Studies Map MF-1435,* 1983.

[266] R. Büttner, B. Zimanowski, J. Blumm, and L. Hagemann, "Thermal conductivity of a volcanic rock material (olivine-melilitite) in the temperature range between 288 and 1470 K," *Journal of Volcanology and Geothermal Research,* vol. 80, pp. 293-302, 1998.